Influence of pulsatility and inlet velocity profiles on tracheal airflow characteristics

by

Bipin Tiwari

A thesis submitted to the Graduate Faculty of
Auburn University
in partial fulfillment of the
requirements for the Degree of
Master of Science

Auburn, Alabama
August 6, 2022

Keywords: Patient-Specific Simulations, Computational Fluid Dynamics, Computed Tomography, Inlet velocity profiles, Pulsatility

Approved by

Vrishank Raghav, Chair, Assistant Professor of Aerospace Engineering
Brian Thurow, W. Allen and Martha Reed Professor of Aerospace Engineering
David Scarborough, Assistant Professor of Aerospace Engineering

Abstract

Patient-specific simulation is a powerful and emerging tool for studying human airway physiological and pathological characteristics. Decision-based systems for clinicians based on the patient airflow characteristics play a critical role in tailored medical treatment, from drug delivery to surgical planning. Computational methods are commonly employed and easily executable to investigate and understand the biofluid mechanics of the airflow in simplified or patient-specific tracheal geometries. One of the key considerations in setting up computations is choosing the correct inlet boundary conditions (BCs). The most common BCs employed in previous studies are a) flat, b) parabolic, c) Womersley, and e) real velocity profiles. In many situations, an idealized velocity profile must be selected if the patient-specific velocity information is unavailable. In addition, the flow patterns change with different breathing frequencies, which might be due to underlying lung disease or physical activity. In order to examine the influence of choosing different inlet conditions and breathing frequencies, the current study executes the simulations of the inhalation-phase airflow in ten patient-specific healthy tracheas for normal and rapid breathing conditions with various inlet velocity profiles mentioned above. Qualitative results for various inlet conditions are presented using velocity and vorticity contours in the trachea's axial and sagittal planes. In contrast, quantitative flow metrics are studied by evaluating net pressure drop, Time-Averaged Wall Shear Stress (TAWSS), and Oscillatory Shear Index (OSI). These results indicate that flat profiles are the least representative of the realistic situations under both breathing conditions. Further, the Parabolic and Womersley profiles led to similar flow patterns and values of TAWSS and OSI for normal breathing conditions. However, in rapid breathing conditions, Womersley profiles better represent the real velocity profiles than parabolic profiles.

Acknowledgments

I would like to thank my advisor Dr. Vrishank Raghav for his guidance, support, and direction to the completion of this research. Under his guidance, I am also grateful for shaping my personal and academic growth in the Applied Fluids Research Group (AFRG). I would also like to thank Dr. Prabakaran Rajamanickam, a post-doc of the AFRG lab, for his help and guidance to complete the research. Finally, I would like to thank my committee member: Dr. Brian Thurow and Dr. David Scarborough, who are willing to be on my committee.

Apart from this, I would like to thank members of the AFRG group member for their support, help, and knowledge during my time as a graduate student in Auburn University. I specially would like to thank Lokesh Silwal, Abbishek Gururaj, William McAtee, John Nix, and Holger Mettelsiefen for their help in providing constructive feedback during the writing of the thesis.

Lastly, I would like to thank my parents Balram Tiwari and Ambika Kumari Panta for their unconditional support and love. I also like to thank my brother Binayak Tiwari and my girlfriend Prashamsa Pandey for all their support and encouragement for my education throughout the graduate school.

Table of Contents

List of Figures

List of Tables

Chapter 1

Introduction

The knowledge of airflow characteristics in human airways is crucial in understanding the physiological and pathological aspects of breathing. This information extracted from the flow characteristic provides valuable information for clinical practice in the evaluation and development of inhalation treatment. Understanding the respiratory flow helps the clinician in the medical treatment of obstructive lung diseases such as Chronic Obstructive Pulmonary Disease (COPD), asthma, and bronchitis. The leading causes of such respiratory diseases are tobacco smoking, passive smoke exposure, workplace exposure to smoke, and pollution [24]. Among obstructive lung diseases, COPD is the third leading cause of death worldwide, causing 3.23 million deaths in 2019 reported by WHO [1] and is associated with long-term disability. A subset of the patients with COPD has also been identified with Expiratory Central Airway Collapse (ECAC), defined by greater than 50 % collapse of the large airways during expiration [39, 15, 43, 76]. This phenomenon causes an additional airflow obstruction in addition to resistance from lower airways, leading to worsened quality of life [10]. Imaging technology like computed tomography (CT) scans and pulmonary function tests (PFTS) based on spirometry measured quantity (e.g., the forced vital capacity and the forced expiratory volume in one second) are different approaches for the diagnosis, treatment, and prognosis of obstructive lung disease in clinical routine [22, 66]. However, regional features of airflow characterized by evaluating pressure drop, flow velocity, and Wall Shear Stress (WSS) in the complex geometry of the airway will help in better assessment and treatment. Thus, studying the airflow biofluid mechanics will shed a new perspective to improve our understanding of the disease progression and its possible causes. This study aims to establish a computational methodology to comprehensively investigate the biofluid mechanics of different inlet velocity profiles in the healthy patient-specific trachea, which will be a prelude to understanding the disease progression.

Computational fluid dynamics (CFD) simulation is a powerful tool for studying flow dynamics and their characteristics through complex airways. CFD is capable of providing helpful information based on the clinically meaningful metrics to improve the understanding of the disease progression, leading to a better assessment of the patient's condition [89, 53, 64, 13, 46, 78]. Advancement in computational efficiency and noninvasive technology has led researchers to explore the respiratory fluid dynamics in a patient-specific manner [30, 77, 17, 26] in contrast to earlier CFD investigations with engineering simplifications such as idealized geometry [81, 34]. A crucial aspect of the CFD simulations is the choice of boundary conditions (BCs) [85] to simulate the breathing of airflow to investigate the flow dynamics. Patients-specific flow simulations have been studied extensively, and the idealized velocity profiles are used most commonly for the simulations as it is challenging to obtain the real velocity profiles that are patient-specific in nature [2, 84, 72]. Flat and parabolic are two popular choices of idealized inlet boundary conditions used to study the respiratory and cardiovascular fluid dynamics [72, 87]. A flat and parabolic profile is a steady state solution in which the patient-specific flow rates are maintained. However, a Womersley elementary profile accounts for the unsteady nature of fluid flow due to oscillating pressure gradients as opposed to a parabolic profile [80, 14]. When breathing frequency changes, the fluid behavior changes as well, which directly affects Womersley profile shape [48, 83]. There are no previous studies on the choice of frequency-driven idealized inlet velocity profiles and their influence on the flow characteristics of the airflow in the patient-specific trachea. This study explores the choice of idealized inlet velocity profile on computational assessment to provide the closest surrogate model to the real velocity profile for studying the airflow characteristics based on the breathing frequency.

Thus this study aims to explore the effects of different idealized inlet velocity profiles on the CFD-derived quantities, essentially on pressure drop, Time-Averaged Wall Shear Stress

(TAWSS), and Oscillatory Shear Index (OSI) resulting from the patient-specific tracheae simulations. Additionally, this study also qualitatively evaluates the flow characteristics such as velocity and vorticity contours along the axial and sagittal planes of the trachea. This simulations are conducted for ten patient-specific tracheae to discern the differences in aiflow characteristics due to the variations in airway geometry as well as the inlet velocity conditions at the inlet. The idealized BCs used in the current study are a) parabolic, b) Womersley, c) flat, and d) real profile, where the real profile is taken from the study conducted for a range of breathing conditions by previous study [37]. Therefore, we test for two breathing breathing conditions that is normal (12-16 breaths per min) and rapid (60-65 breaths per min) breathing rates combined with the aforementioned inlet velocity profile conditions. Thus, the objective of the present study is to simulate the inhalation phase through the patient-specific trachea: a) to qualitatively evaluate the velocity and vorticity contours in axial and sagital planes for idealized and real velocity profiles for one patient case to study the influence of inlet velocity profiles b) to compute flow metrics such as net pressure drop coefficient, Time-Averaged Wall Shear Stress (TAWSS) and Oscillatory Shear Index (OSI) quantitatively for idealized profiles and compare it to the real velocity profile for all ten patient cases.

1.1 Specific Aims

To study the effect of frequency-driven inlet velocity profiles on the airflow characteristics in ten patient-specific trachea for normal and rapid breathing conditions

1. Effect of inlet velocity profiles: To assess the influence of idealized profiles (parabolic, Womersley, and flat) and compare it to the real profile for one patient-specific trachea

2. Effect of breathing frequencies: To assess and identify the closest idealized profile solution that can be used as surrogate model to the real profile to study the airflow characteristics

Chapter 2

Background

This chapter covers human airway anatomy, the physiology of breathing, the biological relevance of Wall Shear Stress, fundamentals of Computational Fluid Dynamics (CFD) and Turbulence modelling details.

2.1 Anatomy of human airway

The anatomy of the human respiratory system is divided into the upper airway, including the nasal cavity, the oral cavity, the pharynx, the larynx (voice box), and the lower airway, which consists of the trachea plus the bronchial tree as shown in the figure 2.1. The lower airways branching starts from the trachea and ends in alveoli, where the air exchange process occurs, creating a tree-like structure called the tracheobronchial tree. This tracheobronchial tree structure consists of 23 generations starting from the trachea, where each generation branches into two airways. Each generation of human airways has a 2^n number of airways where n is the particular generation [81]. The trachea is the largest airway structure that passes air into and out of the lungs. It also moistens, warms, and prevents foreign particles from reaching the respiratory surface. It extends from the end of the larynx to the point of the first bifurcation known as carina. The trachea bifurcates into the left and right main bronchi at the carina. The right main bronchus lies in a more vertical orientation than the trachea, whereas the left main bronchus lies in a more horizontal orientation. Therefore, the right main bronchus is more susceptible to foreign body obstruction. Lobar bronchi transport air towards the pulmonary lobes where right main bronchi branches into three main bronchi: superior, middle, and inferior. The left main bronchi is divided into superior and inferior bronchi. Then comes the segmental bronchi, which aerate the bronchopulmonary segments.

Each segmental bronchi provides approximately fifteen intrasegmental bronchi, which give off many bronchioles that terminate into the pulmonary lobules and alveoli. The alveoli are the airsac where the gas change of oxygen and carbon dioxide occurs.

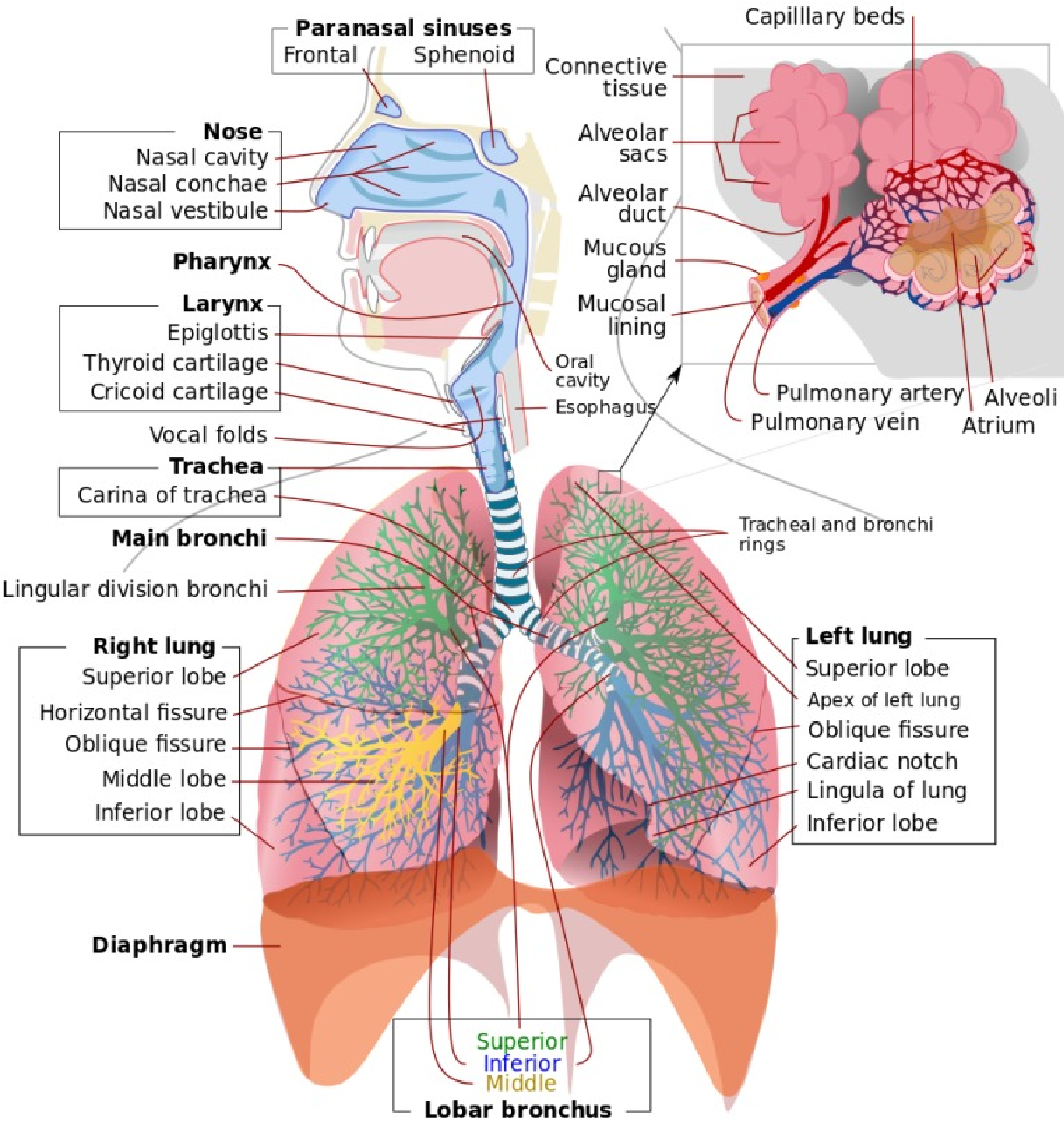

Figure 2.1: The respiratory system of the human body. Adapted from [6]

The trachea is also known as the conduction zone as its primary function is to transport the oxygenated air from the upper respiratory tract to the alveoli for gas exchange process. The length of the trachea, on average, is 11.8 cm with 18 to 22 cartilaginous C-shaped rings, which maintains the rigidity of the structure [28, 29]. The tracheal length in males is reported as 10.5 ± 0.9 cm and 9.8 ± 0.8 cm in females, which shows that tracheal length is shorter in females than in males [38]. There are approximately two cartilage rings per cm of the trachea, and each tracheal ring is an average of 4 cm in height with 3 mm tracheal wall thickness. The average diameter of the trachea is 2.3 cm in the coronal plane and 1.8 cm in the sagittal plane in men, with corresponding values in women with 2.0 cm and 1.4 cm. The shape of the trachea is often ovoid and is affected due to the presence and absence of the disease condition. This shape is circular in children and turns into an ovoid shape in adults. The trachea also stretches during normal inspiration or cough, causing expansion and contraction, which changes its luminal diameter.

2.2 Physiology of breathing

The inhalation and exhalation of air from the lungs is known as breathing. The inhalation process involves bringing in oxygen from the atmosphere to the lungs, and the exhalation process consists in removing carbon dioxide from the lungs [31]. Air naturally moves in from high pressure to lower pressure. As the thoracic cavity volume increases due to contraction or flattening of the diaphragm, the pressure in the alveoli decreases due to which inspiration occurs. Expiration is a passive process because of the elastic recoil of lungs that causes inspiratory muscle to relax and decrease the volume of the thoracic cavity which increases the pressure in the in the cavity thus removing air from the lungs. The average healthy adult person inhales and exhales about 11,000 liters of air every day. Unfortunately, this air contains dust, viruses, soots, fungi, and mold, which are harmful particles and can stick to the surface of the airway and alveoli. The defense mechanism of our respiratory system helps to remove such harmful particles. The thin mucus layer lining in the lungs helps capture such harmful particles and prevents it from reaching the lungs. In addition, lungs walls are lined by respiratory mucosa consisting of cilia, a thin hair-like structure to propel and remove mucus as a cough. They are also removed by alveolar macrophages, the white blood cell (WBC) that scavenges the particles and engulfs them [56].

Lung volumes refer to the air volume in the lungs at a given time of the respiratory cycle. Similarly, lung capacities are derived from the lung volumes at a given time of the respiratory cycle. Lung volumes will be altered based on factors like depth of respiration, ethnicity, gender, age, body composition, and certain respiratory diseases. It is the summation of two or more lung volumes. Four standard lung volumes and four standard lung capacities are clearly represented in the Figure 2.2 measured with an diagnostic device known as Spirometer are mentioned below [33]:

1. Tidal Volume (TV): Amount of air that can be inhaled or exhaled during a period of one respiratory cycle. It measures around 500 ml in healthy adult.

2. Inspiratory Reserve Volume (IRV): The amount of air that a person can forcefully breathe in after inhalation of normal tidal volume.

3. Expiratory Reserve Volume (ERV): The amount of air that a person can breathe out forcefully breathe out after exhalation of normal tidal volume breathing.

4. Residual Volume (RV): The volume of air remaining in the lungs after maximum exhalation.

5. Inspiratory Capacity (IC): It is the maximum air inhaled after the resting state.

6. Total Lung Capacity (TLC): It is maximum amount of air that the lung can accommodate after maximum inhalation.

7. Vital Capacity (VC): It is the maximum amount of air that a person can inhale after a maximum exhalation.

8. Functional Residual Capacity (FRC): The volume of air remaining in the lungs after a normal, passive exhalation.

Lung volumes and capacities are part of the pulmonary function test to determine the lung working condition, which will help in the detection and identifying the pathophysiological change [52]. The most commonly used units for diagnosing and treatment of obstructive lung conditions are Forced Vital Capacity (FVC) and Forced Expiratory Volume in one second (FEV_1). A low value of FEV_1/FVC indicates obstructive lung condition.

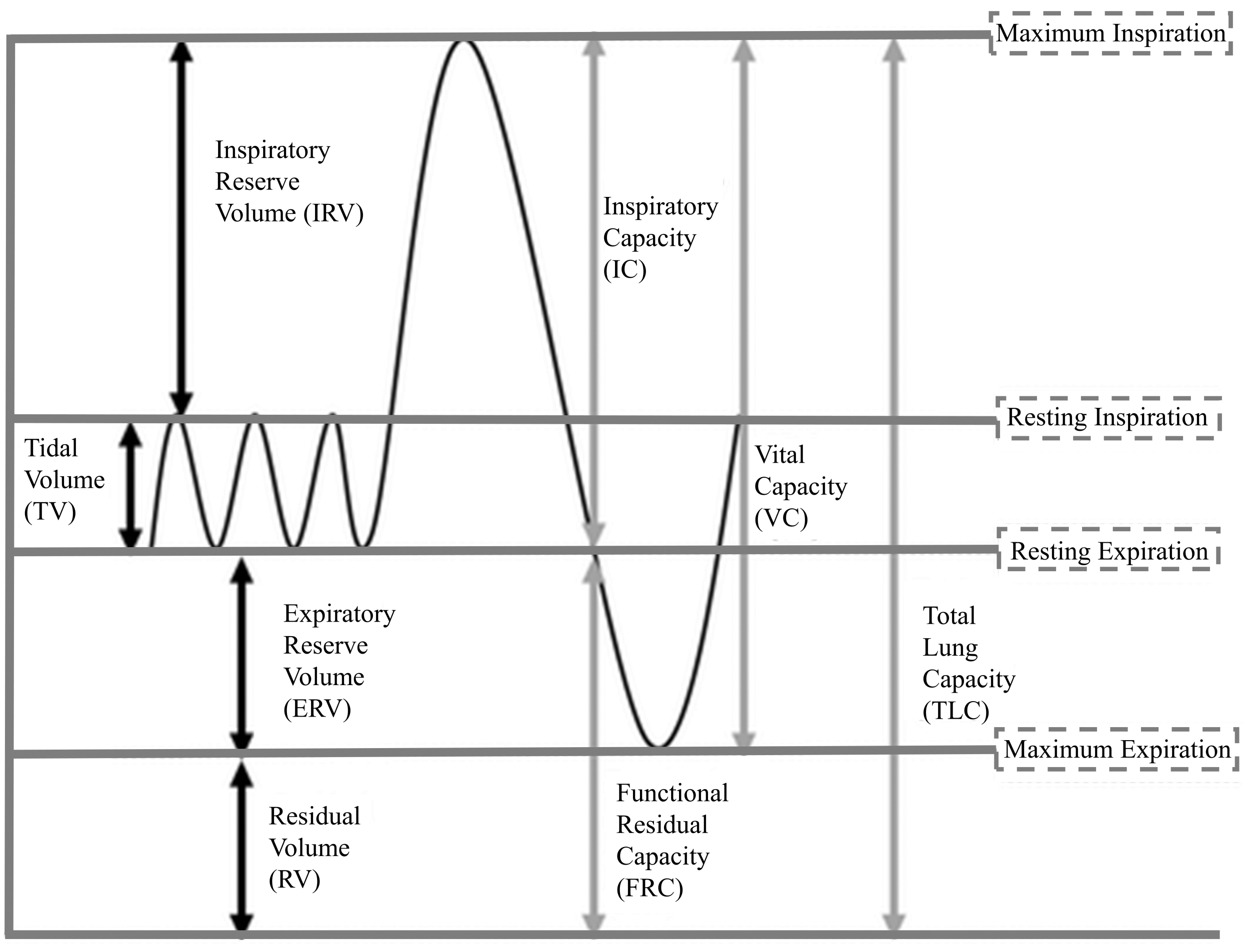

Figure 2.2: Lung volumes and capacities. Adapted from [50]

The respiratory rate determines the number of breaths that a person takes per minute, and it is one of the four primary vital signs [4] to assess the person's general physical health.

The two different respiratory rates considered in this study are normal and rapid breathing, explained in the subsection below.

2.2.1 Normal breathing

Normal breathing is a slow and regular process where inspiratory volume and chest movement are maintained. It is measured when a person is at rest, with no strenuous activity prior to the measurement. The most common factors that affect the respiratory rate are emotional state, physical fitness, body temperature, and health status. Normal breathing helps maintain a balanced level of oxygen and carbon dioxide within the body [23]. According to Table 2.1, the normal breathing rate for adults is 12-20 bpm and between 25-60 bpm for newborn babies below six months.

Table 2.1: Breathing rate with respect to different age groups [45, 86, 7]

Age	Breathing Rate (bpm)
Birth-6 weeks	30-60 bpm
6 months	25-40 bpm
3 years	20-30 bpm
6 years	18-25 bpm
10 years	15-20 bpm
Adults	12-20 bpm
Adults $\geq$ 65 years	12-28 bpm
Adults $\geq$ 80 years	10-30 bpm

2.2.2 Rapid breathing

Rapid breathing is when a person's breathing rate is higher than normal and is more than 20 breaths per minute in adults. Tachypnea, a term used to define rapid breathing, may indicate a pathological state. However, it does not necessarily have a pathological cause, as exercise can also trigger this condition. The most common rapid breathing causes are pneumonia, carbon dioxide poisoning, asthma, and COPD. Aspiration of foreign bodies, allergic reactions, and anxiety states can also cause rapid breathing. Tachypnea is rapid and shallow breathing that should not be confused with hyperventilation, which is rapid and deep breathing. As opposed to a normal breathing rate, rapid breathing occurs due to the build-up of carbon dioxide in the blood. The increased carbon dioxide makes the blood more acidic than usual, alerting the brain to the danger. In response to this, the brain signals the respiratory drive to increase the rate of breathing to balance out the imbalance between oxygen and carbon dioxide [45, 60].

2.3 The biological relevance of Wall Shear Stress (WSS)

When air flows through the airway vessel, it exerts a force on its wall. This force exerted on the vessel wall can be divided into two components. The perpendicular component of the force vector contributes to air pressure leading to the deformation of the wall. In contrast, the tangential component of the force vector leads to shearing deformation of the wall, which can be sensed by the endothelium and is known as wall shear stress. Wall shear stress is sensed by various stress-responsive cell components and is related to remodeling of the blood vessel, and airway vessel [27, 71, 75]. Airway remodelling is the structural changes in the airway due to repeated injury or repair process which is characterized by changes of tissue, cellular and molecular composition affecting airway smooth muscle, epithelium, blood vessels, and extracellular matrix [3]. Mechanical stresses are responsible for the proliferation of structural cells of the airway and its elongation. The abnormal loading of mechanical stresses thus results in altered cellular activation, leading to fibrosis (thickening or scarring of tissue as a result of repair), which results in remodeling of the airways [3]. The endothelium lining of the vessel wall repeatedly subjected to different flow behaviour like disturbed flow, re-circulation and flow separation due to vessel remodelling causes the disease progression [18]. Therefore, understanding the flow behaviour with near wall flow characteristic like WSS distribution on the vessel wall will improve our understanding of the disease progression and help the clinician approach the patient with better treatment.

2.4 Computational Fluid Dynamics (CFD)

CFD is a well-known methodology for mathematically modeling physical fluid flow problems and numerically solving them using computational power. The fluid flow phenomenon is based on the fundamental conservation laws of mass, momentum, and energy that govern fluid motion. This governing equation in partial differential form is converted into the algebraic equation system and solved using various numerical schemes such as finite-difference methods [42]. However, modeling in the CFD is challenging due to complex flow physics associated with the fluid flow as randomness, three-dimensionality, recirculation, and eddies. There are three types of CFD methods used to model turbulent flows: direct numerical simulations, large-eddy simulations, and Reynolds-Averaged Navier-Stokes equations. Several factors like computational cost, ease of use, range of applicability, and accuracy is considered depending on the specific flow problem. The CFD user plays a role in deciding a suitable model to computationally solve the flow problem and their need. Due to complex geometry with a low Reynolds number, this study is interested in accurately predicting the flow characteristics undergoing turbulent transition.

The most widely adopted CFD method for engineering application is Reynolds Averaged Navier-Stokes (RANS), which is a time-averaged equations of motion for fluid flow. Flow quantities are divided into the mean plus fluctuating part in a turbulent flow, and Osborne Reynolds first proposed this, which is well known as Reynolds Decomposition. For general three-dimensional flows, the four equations of pressure and the three velocity components are need to be solved along with the six Reynolds stresses resulting from the Reynolds averaging. The continuity and RANS equations can resolve the pressure and velocity components. However, an expression for the Reynolds stress is required to obtain a closed-form solution. Therefore a turbulence model or directly modeled Reynolds stress transport equation is used to get a closed-form solution to the RANS equations. The algebraic and transport equation to turbulence models brings closure to the RANS equations.

Algebraic turbulence models are the simplest turbulence models for determining the eddy viscosity. Transport equation models solve the quantities of the turbulent kinetic energy and dissipation rate of the energy-containing eddies. Many types of turbulence models are used to solve engineering flows, and each model has its advantages and limitations. All the different kinds of conventional turbulence models are presented in the text of Wilcox [82]. The particular interest of this study is the type of RANS turbulence models applied to predict the transitional and separated internal flows with low Reynolds numbers.

2.4.1 Transition modeling

Transitional flows are the intermediate state of fluid flow between laminar and turbulent, where both viscous forces and Reynolds stresses are equally important. The transition occurs through different mechanisms and is typically due to the flow instability (Tollmien-Schlichting waves) in the aerodynamics flows, and another mechanism is separation induced flows where the laminar boundary layer separates due to adverse pressure gradient. Therefore, there is an inherent problem in using the RANS model for predicting transitional flows. Since a conventional RANS model eliminates the effect of linear disturbance of the growth, linear and non-linear effects are relevant in the case of transitional flow. The Menter et al. [55] has developed a new transitional flow model called γRe_θ Shear Stress Transport (SST) model to estimate the flow accurately. This model is also known as the transitional SST model and is used to predict the laminar and laminar to turbulent and turbulent states of the flow. The difference between the γRe_θ SST model with $k - \omega$ SST model is that there are two other transport equations: one for, γ, the intermittency which produces the transition locally, and another for transition onset criteria in terms of the momentum thickness Reynolds number.

Each patient-specific trachea has unique geometrical features with curvature, turtuosity, and variation of cross-sectional area along the length of the trachea. Also, the Reynolds number of airflow in ten patient cases falls in the range of 2230 ± 364, which is in the transitional flow regime. Therefore, accounting the patient-specific geometry and Reynolds number regime, the transitional model justifies capturing the flow characteristics to better understand the tracheal flow.

Chapter 3

Methodology

3.1 Patient cohort

COPDGene® [67] is a study that enrolled 10,000 participants who were current and former smokers between ages 45 and 80 years across 21 clinical centers throughout the United States. The FEV_1/FVC ratio obtained from a lung function test is used to assess obstructive lung disease where a patient with a value less than 0.7 is diagnosed with COPD [10]. The present study only includes the non-smokers from the large cohort study without COPD and considered as healthy or normal patients. Therefore, ten normal patient samples were included for this study where the sample's mean age is 63.3 ± 7.3 ($mean \pm SD$) with eight females and two males. The respective BMI, weight, and height of the patient cases are reported in the Table 3.1.

Table 3.1: Patient demographics(n=10)

Parameters	Mean±SD
Age ($years$)	63.3 ± 7.3
Gender (Female/Male)	8/2
BMI (kg/m^2)	28.1 ± 5.5
Weight (kg)	78.5 ± 17.9
Height (cm)	166.9 ± 10.6
FEV_1/FVC	0.8 ± 0.1

All data are reported as mean ± standard deviation unless specified.
FEV_1 = Forced Expiratory Volume. FVC = Forced Vital Capacity.

3.2 Pre-processing of patient-specific models

The inspiratory CT scans of the ten healthy normal patients were obtained from the COPDGene® study. The CT scan was taken during full inspiration when the lung volume is completely filled with air. These medical images obtained from CT scans are used to reconstruct the patient's anatomy. Over the past decade, the technology for reconstructing patient-specific anatomy has advanced steadily. Many commercial and open-source software are used to facilitate airway vessels' manual segmentation from a stack of medical images. After the stack of images has been interpolated, a surface or volumetric model is reconstructed for the simulation. 3D Slicer (http://www.slicer.org/) is an image processing package used to convert the image segmentation to a solid model. This medical imaging data obtained from the COPDGene® study was imported to a 3D slicer to reconstruct volume from NiFTI files (raw image data saved as a 3D image). Segmentation was done by applying a volumetric filter and desired threshold value to the region of interest. The Laplacian smoothing algorithm was then applied in the segmented volume with the factor manually selected to balance between surface smoothness and maintaining the anatomical details. This final volume was then exported as a Standard Tessellation Language (STL) file, which describes the surface of a 3D model with raw and unstructured triangles [8]. Since a CT scan with a low resolution produced few triangles, Vascular Modelling Toolkit (VMTK, www.vmtk.org) software was used to increase the number of triangles so that the geometry could be accurately modeled. Increasing the number of triangles to represent the surface of the 3D model will also avoid the potential mesh problem that might be due to the low number of triangles.

The extracted trachea inlet had a non-circular cross section, which makes it difficult to impose the boundary condition. The inlet of the trachea was therefore extruded by 2 mm to convert from a non-circular to a circular cross-section in SolidWorks® (SolidWorks Corp., Waltham, MA USA). The cross-sectional area of the inlet was kept constant to maintain the volume flow rate of air during breathing. The workflow from volumetric reconstruction in a 3D slicer to SolidWorks® is shown in Figure 3.1. Therefore, the final 3D geometry created was exported to the ICEM CFD (ANSYS Inc., Pennsylvania, USA) for mesh generation, described in the following section.

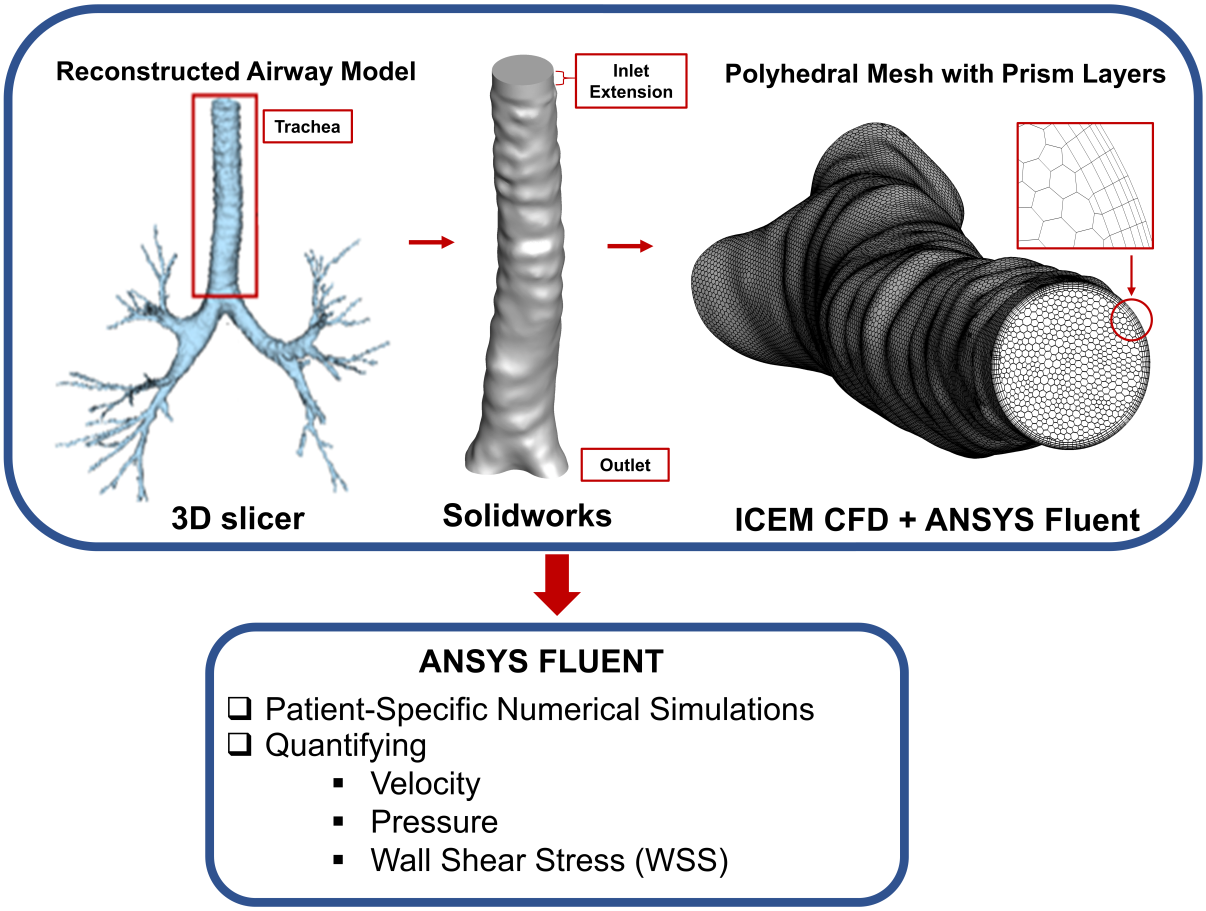

Figure 3.1: Workflow from CT scan to trachea model, mesh generation leading to the ANSYS Fluent® simulations

3.3 CFD mesh generation

During the computational modeling, mesh generation plays an important role, as simulation results depend on mesh quality. In order for the simulated results to be accurate and reliable, the mesh quality must be good. A fine mesh will result in a more accurate solution with increased computational power and time. In contrast, the coarse mesh will result in a less precise solution with decreased computational power and time. Thus, it is essential to maintain accuracy at a acceptable computational cost by using optimized mesh quality. A time-step independent study is also conducted to ensure that results do not vary with time-step size as the breathing process is unsteady. The mesh independence study and the time-step independence study were conducted to obtain the simulation's optimal mesh size and time-step size.The result obtained from mesh-independence study and time-independence study is presented in the result section of this thesis.

The trachea model was imported to ICEM CFD, where an unstructured tetrahedral mesh was generated as it was deemed appropriate due to the complex shape of the geometry. The mesh generation was conducted with the Octree mesh method for the fine-resolution surface mesh, followed by the Delaunay method to generate a smooth volumetric mesh. The prism layer of 6 concentric rows with a smooth cell transition ratio ($\sim$1.11) was also employed for the boundary wall. The mesh generation process generated a mixture of prism layers and tetrahedral elements accompanied by a few pyramids for a smooth transition towards the trachea wall to resolve the high velocity gradient. This mesh generated was further processed in the FLUENT® to generate a polyhedral mesh to increase the stability and decrease the computational time for the simulation. The workflow from CT scan to trachea model finalized for simulation is shown in the Figure 3.1.

3.4 Breathing conditions

In this study the simulations are conducted for the inhalation phase of the breathing cycle to study the influence of different inlet boundary conditions. The exhalation phase was excluded from the study for two reasons a) CT scan was obtained at full inspiration, and b) during exhalation, the movement of the air is out of the lungs which changes the boundary condition at the inlet of the trachea. The airflow simulation is conducted for two breathing conditions [37], the first one corresponds to a normal breathing condition with a typical breathing frequency, $f = 0.28Hz$ (17 breaths per min), and a peak flow rate $Q_{max} = 364$ ml/s whereas the second one corresponds to rapid breathing conditions with $f = 1.08Hz$ (65 breaths per min) and $Q_{max} = 360$ ml/s. The above-mentioned numeric values are taken from the experimental study conducted to simulate the two breathing conditions in a benchtop setup [37]. The flow rates as a function of time for both breathing conditions are approximated with a sinusoidal waveform as shown in the Figure 3.2. Thus, the flow rate Q can be expressed as

$$Q = Q_{max} \sin(\omega t) \tag{3.1}$$

where $\omega = 2\pi f$ is the angular frequency and t is the time. For normal breathing conditions ω= 1.74 rad/s and for rapid breathing conditions ω= 6.9 rad/s.

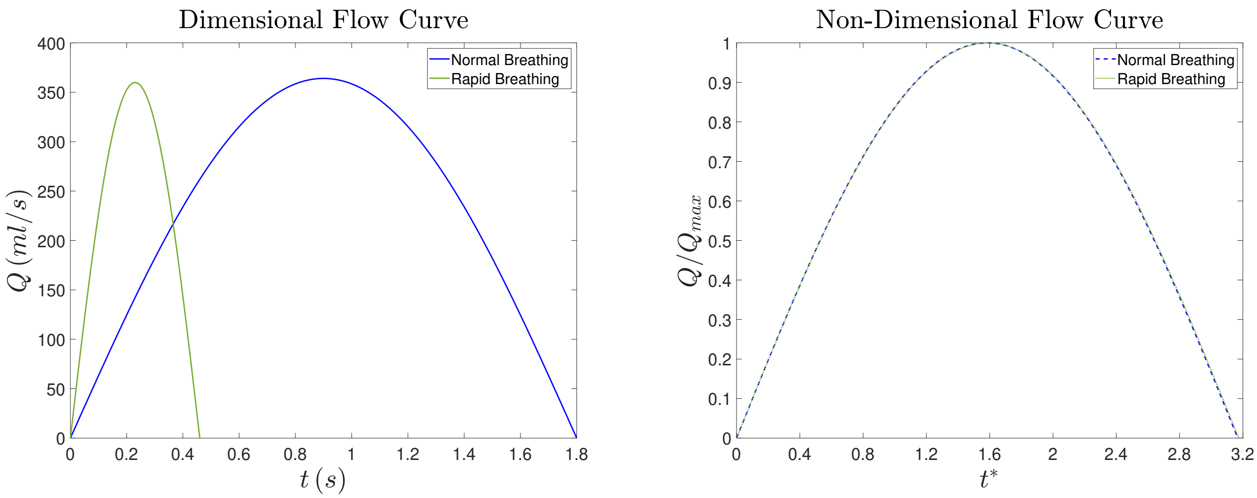

Figure 3.2: Flow rate corresponding to inspiration cycle for normal and rapid breathing conditions

3.5 Non-dimensional variables and parameters

As the breathing condition considered for the simulations is defined in the previous section, this section explains the non-dimensionalization of various physical variables which will help in interpretation of the results. The non-dimensionalization of the fluid mechanics problem starts with the selection of characteristic velocity [88] (The characteristic length scale is D and characteristic time scale is omega). For the internal flows, the characteristic velocity is the average velocity measured at the inlet cross sectional area. The non-dimensional variables and parameters are defined in the following paragraphs.

Average velocity is defined as the flow rate at the inlet cross-section divided by its cross-sectional area. The trachea geometry is patient-specific with the inlet diameter D changing from case to case, leading to different cross-sectional areas and correspondingly different average velocities at the inlet. The average velocity is given by

$$\bar{u} = \frac{4Q_{max}}{\pi D^2}. \tag{3.2}$$

The diameter and average velocities for the five cases are shown in Table 3.2 and Table 3.3 for normal and rapid breathing condition respectively.

The Reynolds number is the ratio of the inertial to viscous forces and here it is defined based on the diameter, average velocity and kinematic viscosity of air. Thus the Reynolds number is given by

$$Re = \frac{\bar{u}D}{\nu} \tag{3.3}$$

where ν is the kinematic viscosity of the air that is 1.524E-5 m^2/s at room temperature 25 $^{\circ}C$. Based on the calculated Reynolds number, flow through the pipe is classified as laminar for $Re < 2000$, where the viscous forces are dominant, turbulent for $Re > 4000$ where inertial forces are dominant, and transitional if $2000 < Re < 4000$, where both inertial and viscous forces has similar contribution [54]. Laminar flow is characterized by smooth motion with little or no mixing, where molecular diffusion is dominated with low molecular convection. In contrast, turbulent flow is identified by disturbances and chaotic motion characterized by eddies, recirculation of the fluid causing high lateral mixing. The intermediate region where the flow can either be in a laminar or turbulent state intermittently (both in space and time) is known as the transitional region, where both inertial forces as well as viscous forces contributions are equal. Transitional flows have a higher tendency to be laminar if the Reynolds number is close to 2000 and turbulent if they are close to 4000. Table 3.2 and Table 3.3 below give the Reynolds number for ten patient cases for normal and rapid breathing conditions, respectively.

Table 3.2: Reynolds number for normal breathing conditions for ten patient cases

Cases	Diameter(D) (mm)	Average Velocity ($\bar{u}$) (m/s)	Reynolds Number
Case 1	13.52	3.65	3241
Case 2	16.49	1.70	1840
Case 3	13.50	2.55	2255
Case 4	13.72	2.46	2215
Case 5	13.53	2.53	2244
Case 6	14.30	2.26	2122
Case 7	13.96	2.38	2179
Case 8	15.63	1.90	1945
Case 9	13.51	2.55	2257
Case 10	15.23	2.00	1999
Average	14.34	2.40	2230
Standard Deviation	1.02	0.51	364

Table 3.3: Reynolds number for rapid breathing conditions for ten patient cases

Cases	Diameter(D) (mm)	Average Velocity ($\bar{u}$) m/s	Reynolds Number
Case 1	13.52	3.61	3201
Case 2	16.49	1.68	1818
Case 3	13.50	2.52	2233
Case 4	13.72	2.43	2188
Case 5	13.53	2.50	2219
Case 6	14.30	2.24	2102
Case 7	13.96	2.35	2153
Case 8	15.63	1.88	1929
Case 9	13.51	2.52	2234
Case 10	15.23	1.98	1979
Average	14.34	2.42	2206
Standard Deviation	1.02	0.17	359

The Womersley number is the ratio between transient or oscillatory inertial forces to viscous forces and it is defined by

$$Wo = \sqrt{\frac{t_{viscous}}{t_{oscillation}}} = \frac{D}{2}\sqrt{\frac{\omega}{\nu}}. \tag{3.4}$$

It describes the pulsatility of the flow, where a higher Womersley number represents higher pulsation. It can also be represented as the square root of the ratio of viscous time scale ($t_{viscous} = \frac{D^2}{4\nu}$) to the oscillatory time scale ($t_{oscillation} = \frac{1}{\omega}$) as shown in Equation 3.4. Womersley number for ten patient-specific cases for normal and rapid breathing conditions are shown in the Table 3.4.

Table 3.4: Womersley number for normal and rapid breathing conditions

Cases	Diameter (D) mm	Wo (Normal Breathing) $\omega = 1.74\ rad/s$	Wo (Rapid Breathing) $\omega = 6.9\ rad/s$
Case 1	13.52	2.28	4.55
Case 2	16.49	2.79	5.55
Case 3	13.50	2.28	4.54
Case 4	13.72	2.32	4.62
Case 5	13.53	2.29	4.55
Case 6	14.30	2.42	4.81
Case 7	13.96	2.36	4.70
Case 8	15.63	2.64	5.26
Case 9	13.51	2.28	4.55
Case 10	15.23	2.57	5.12
Average	14.34	2.42	4.82
Standard Deviation	1.02	0.17	0.34

Lengths (r, z), velocities (v, v_z), time (t), and pressure (P) are non-dimensionalized as shown

$$r^* = \frac{2r}{D},\ z^* = \frac{2z}{D},\ v^* = \frac{v}{\bar{u}},\ v_z^* = \frac{v_z}{\bar{u}},\ t^* = \frac{t}{t_{oscillation}},\ \text{and}\ P^* = \frac{PD}{2\mu\bar{u}} \tag{3.5}$$

where all the lengths are divided by radius of the inlet, $D/2$, velocities by average velocity, $\bar{u}$, time by oscillatory time scale, $t_{oscillation}$, and pressure is nondimensionalized by $\frac{2\mu\bar{u}}{D}$ (viscous shear stress). This will help in reduction of the variables, data analysis and better interpretation of the results.

3.6 Mathematical model

3.6.1 Governing equations

Airflow characteristics for the inspiration cycle are calculated by solving the Navier-Stokes equation, where air is assumed as an incompressible (constant density), Newtonian (constant viscosity) fluid with kinematic viscosity of 1.52E-05 m^2/s at 25 $°C$. The continuity and Navier-Stokes equations that is used to solve for the velocity field are shown in Equation 3.6 and Equation 3.7.

$$\nabla \cdot \mathbf{u} = 0 \tag{3.6}$$

$$\frac{\partial \mathbf{u}}{\partial t} + (\mathbf{u} \cdot \nabla)\mathbf{u} = -\frac{1}{\rho}\nabla p + \nu \nabla^2 \mathbf{u} \tag{3.7}$$

3.6.2 Numerical methods

As the governing equations are non-linear partial differential equation, the analytic solutions are difficult to obtain. A numerical technique is necessary to approximate the solution of these equations. ANSYS Fluent® (ANSYS 19.5,ANSYS Inc., Pennsylvania, USA) is used as the numerical solver in this study which is based on the finite volume method (using integral form of partial differential equations). The computational domain is discretized into the finite control volume and then the governing equation is integrated on each of the control volume to construct the number of the algebraic equations for velocity and pressure. This discrete equations are linearized to solve the continuity and momentum equation to get the updated values of dependent variable for each iteration to obtain the velocity and pressure.

3.6.3 Solver setting

The transient flow simulation was conducted using transition Shear Stress Transport (SST) k-omega viscous model for the simulations as the Reynolds number ranges from 1818 to 3241. Although the Reynolds number is below 2000 in some cases, flow instabilities are prevalent due to the complexity of the geometry which justifies the use of transition model [49]. Second order discretization schemes were used for pressure and momentum with second order implicit schemes for transient flow. Furthermore, polyhedral mesh was applied to increase the stability and decrease the computational time since this decreases the cell count than the tetrahedral mesh generated from ICEM CFD [74, 73]. To increase the accuracy of the gradient calculation in the polyhedral mesh, warped-face gradient correction was enabled. A residual of 1E-03 was used as the convergence criteria with the time-step size of 1E-02 s.

A time-varying velocity profile was implemented as the inlet boundary condition, and a time-varying pressure was prescribed as the outlet boundary condition for the simulations using a user-defined function (UDF). This boundary condition was prescribed with the intermittency, which is the fraction of time when the flow is turbulent, of 0.05 and turbulence intensity of 1 % [69]. The turbulence viscosity ratio, defined as the ratio of turbulent viscosity to molecular viscosity, was set to 10 for inlet and outlet conditions that define the onset of transition. This value was prescribed with the assumption of the low turbulence at the trachea's inlet and outlet, which provides the medium level of turbulence [2]. The simulation was performed in 3D space with a no-slip boundary condition for the geometry wall. For each case, four simulations were run with the three idealized velocity profiles, and a real velocity profile explained in the inlet boundary condition section. The flow rate was kept constant for normal and rapid breathing conditions across all the patient cases.

3.7 Boundary conditions

3.7.1 Inlet

As the airway structure are complex, selecting the appropriate boundary conditions are an important factor in the study of the flow through human airways. This study compares the influences of the idealistic velocity profile with the real velocity profile simulations. The time-varying idealistic velocity profiles assumed for this study are flat, parabolic and Womersley [80] profile which is formulated by using the peak flow rate for the two breathing conditions and the radius of the inlet. The snapshot representation of the four inlet velocity profile is shown in the Figure 3.5. Overall details of the idealistic and real velocity profiles are explained in the following sections, and the velocity profile at the center line is represented in the Figure 3.4. The velocity contour plot at the inlet for normal and rapid breathing conditions for all the velocity profiles is presented in the Figure A.3 and Figure A.4 in the appendix section.

Flat profile

Uniform flow across the cross-section where all the points have equal velocity will produce a flat (plug) profile. This velocity profile distribution is more prevalent at high Reynolds number that is in a turbulent flow [42]. The flat profile is given by

$$v^* = \sin(t^*). \tag{3.8}$$

Parabolic profile

The fully developed inlet velocity profile which is based on the Poiseuille flow gives the parabolic shape. Poiseuille flow is basically a pressure driven flow in long cylindrical pipe of constant cross-section for a laminar flow of an incompressible Newtonian fluid. As the fully developed parabolic profile has been considered in the literature [68] to study the flow characteristics in the trachea, this profile is selected as one of the idealistic profiles in this study. Parabolic velocity profile is given by

$$v^* = 2\big[1 - (r^*)^2\big] \sin(t^*). \tag{3.9}$$

Womersley profile

A flow which has periodic variations is known as pulsatile flow or Womersley flow. For the $Wo \leq 1$, there is no significant difference between Womersley and parabolic profile since pulsatile flow frequency will be low and viscous effects dominates which gives enough time for parabolic profile to develop. On the other hand, for the $Wo > 1$ the frequency of pulsation will be large causing velocity profile to be more flat or plug-like [83]. Womersley profile is given by

$$v^* = -i \left[\frac{1 - J_0\left(Wo\, r^*\, i^{3/2}\right) / J_0\left(Wo\, i^{3/2}\right)}{1 - 2J_1\left(Wo\, i^{3/2}\right) / Wo\, i^{3/2} J_0\left(Wo\, i^{3/2}\right)} \right] \mathrm{e}^{it^*} \tag{3.10}$$

Where J_0, J_1 are Bessel functions of the first kind of order 0 and 1, i is the imaginary unit, and t is the time.

Real velocity profile

Real velocity profile is taken from an experiment done in a double bifurcation model of the airway structure which is relevant to the respiratory human airways with Magnetic Resonance Velocimetry (MRV) [37] where water was used as a working fluid. This experiment was conducted in the benchtop setup with the range of breathing conditions. Among these ranges of breathing conditions, normal and rapid breathing conditions was selected for this study. The velocity data obtained from the experimental study was extracted using the in-house MATLAB® (MathWorks, Natick, MA, USA) code at the inlet of the trachea. The extracted velocity data at the inlet was implemented in the computational mesh of the CFD simulations using the UDF as shown in Figure 3.3. The data extracted from the inlet of the trachea was interpolated spatial and temporally to implement in the inlet of the computational mesh and to conduct time resolved simulations. Details of the code that is used to extract and implement the velocity profile is given in the Appendix B.

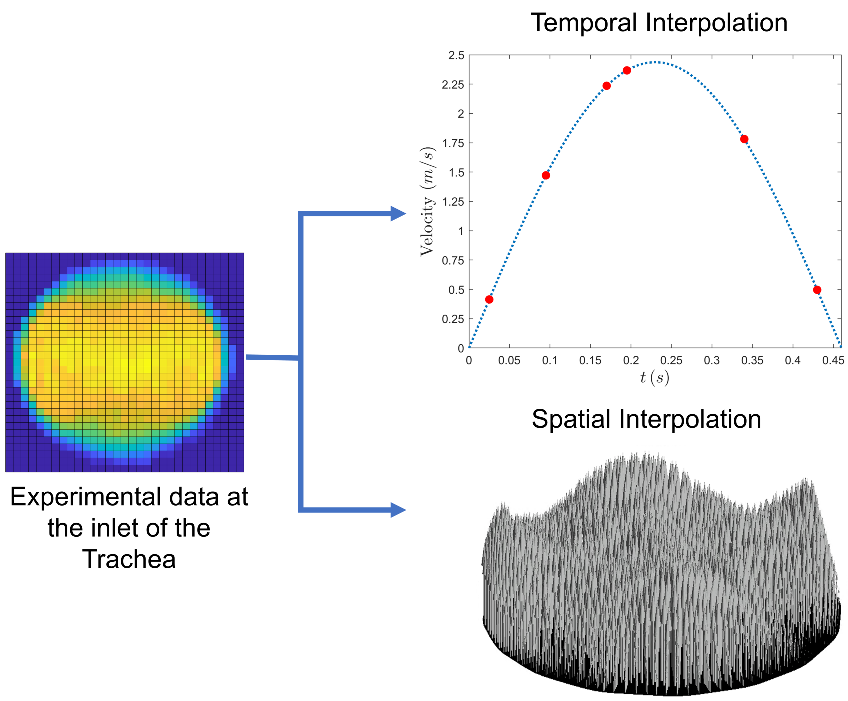

Figure 3.3: Implementation of real velocity profile from the MATLAB® data of the experimental study to the CFD inlet

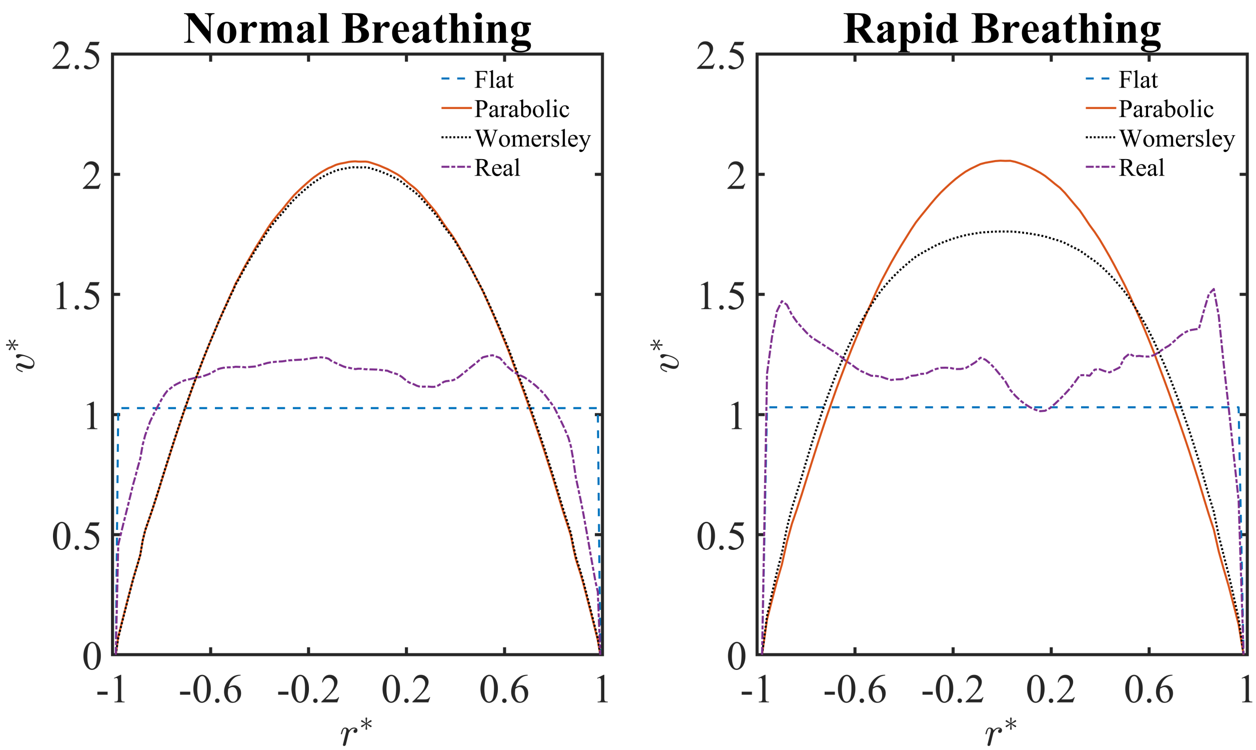

Figure 3.4: Inlet velocity profile drawn at the center of the inlet for the flat, parabolic, Womersley, and real profile of one patient case

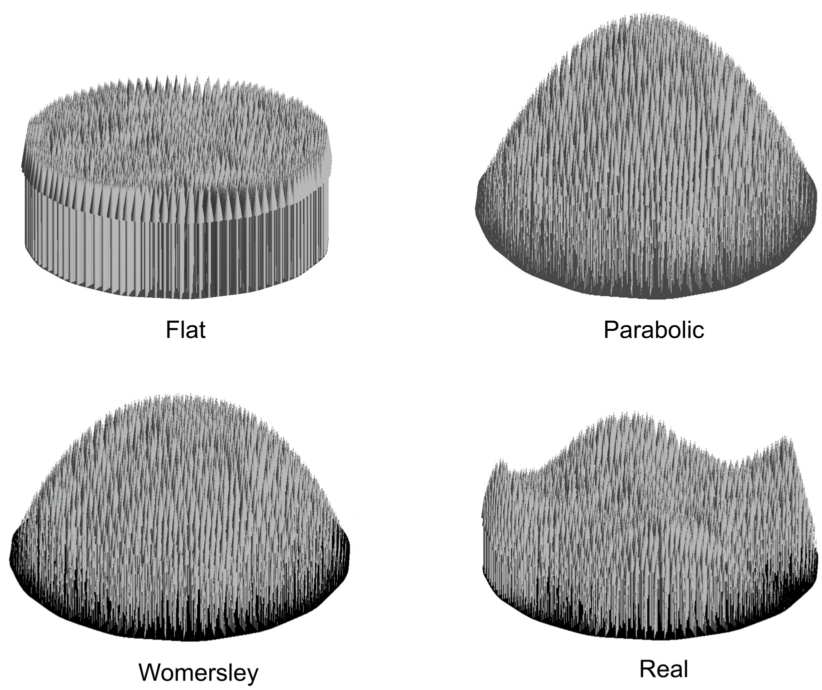

Figure 3.5: Snapshot of the four inlet velocity profiles at the peak inspiratory flow for rapid breathing condition

3.7.2 Outlet

Although previous studies have used a zero-pressure condition at the outlets of the trachea, it has influence on the flow characteristics [63, 62]. A time-varying pressure outlet boundary condition was calculated for the outlet of the trachea coupling with the lower airways pressure drop due to compliance and resistance which will produce physiologically realistic flow patterns [79, 5]. In this current study we model the breathing of the human airways by the pressure difference between the intrapleural pressure (which is the pressure in the pleural cavity) and the atmospheric pressure [58] at the mouth. The pressure drop in the lower airways is calculated using the resistance and compliance value of the healthy adult from the literature [12, 70] as shown in Equation 3.11. The lower airways resistance and compliance values taken for this study are reported in the Table 3.5. The pressure at the outlet of the trachea is given by

$$P_t(t) = R_g Q(t) + \frac{V(t)}{C_g} + P_i(t). \tag{3.11}$$

where $Q(t)$ is the flow rate, $V(t) = \int Q(t)dt$ is the time-dependent breathing volume, P_t is the pressure at the trachea, P_i is the intrapleural pressure at the pleural cavity which drives the breathing flow, and finally R_g, C_g are the resistance and compliance of the lower airways, respectively. The time-varying pressure implemented at the outlet of the trachea is shown in Figure 3.6.

Table 3.5: Resistance and compliance value of a healthy adult for lower airways

	Values	Units
Resistance (R_g)	1.5E-03	$cmH_2O - s - ml^{-1}$
Compliance (C_g)	1.81E02	$ml - cmH_2O^{-1}$

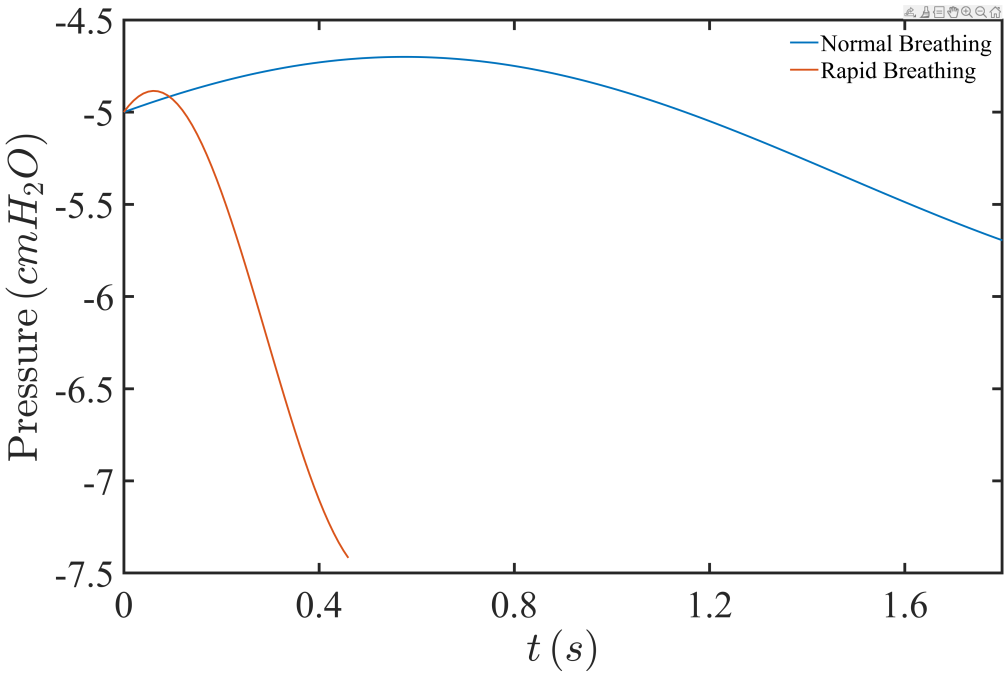

Figure 3.6: Time-varying pressure computed at the outlet of the trachea for normal and rapid breathing conditions

3.8 Data analysis

3.8.1 Wall Shear Stress (WSS)

Fluid flowing in a cylinder does not have a uniform velocity across all the points in the cross-section perpendicular to the length of the tube; velocity is highest at the center of the tube and decreases as it reaches the wall. The non-uniform distribution of velocity is due to the frictional forces that arise from the interaction of fluid itself and fluid with the wall, which causes the diffusion of momentum from the wall to the center. The transfer of momentum between the fluid molecules will cause a velocity gradient to exist in the pipe, due to which tangential stress arises, causing resistance in the movement of one layer of fluid over the adjacent layer. The property of the fluid which offers this resistance is known as viscosity. Lower viscosity causes a lower velocity gradient, which causes lower shear stress and vice versa.

WSS is defined as the tangentially acting force per unit surface area by the flowing fluid on the walls of the tube in the opposite direction. WSS is directly proportional to the velocity gradient, which shows how fast the velocity in one layer of the fluid moves with respect to the velocity at the adjacent layer of the fluid in the direction perpendicular to the flow. Wall shear stress (τ_w) for each case at the wall is calculated by

$$\tau_{\mathrm{w}} = \mu \left.\frac{\partial u}{\partial r}\right|_{y=0} \tag{3.12}$$

measured close to the vessel wall, where μ is the viscosity of the fluid, u is the velocity, and r is the distance perpendicular to and away from the wall.

3.8.2 Time-Averaged Wall Shear Stress (TAWSS)

In a pulsatile flow the WSS varies in time, so TAWSS filters out the temporal variation of the WSS to account for the total effect. Therefore, the TAWSS is defined as a measure of the total wall shear stress exerted on the wall which is averaged over a breathing cycle. The TAWSS is calculated by

$$\mathrm{TAWSS} = \frac{1}{T}\int_0^T |\tau_{\mathrm{w}}| dt \tag{3.13}$$

It is a WSS-based descriptor that is used to study the effects of airflow in the airway vessel. Wall shear stress corresponds to the compressing or stretching mechanical forces experienced by the wall, which directly influences the endothelial cell function [3]. The change in velocity gradient near the wall will influence the particle deposition that is important in aerosol drug delivery. A high WSS indicates increased velocity gradient near the wall region where aerosol particles are expected to collide and deposit in the wall. A lower WSS indicates a smaller velocity gradient where aerosol particles are more likely to be suspended in the air and later can be repelled or attracted to the wall [61].

3.8.3 Oscillatory Shear Index (OSI)

It is a non-dimensional metric which describes the cyclic departure of the WSS vector over a breathing cycle and characterizes if it aligns with TAWSS vector. The OSI is calculated by

$$\text{OSI} = \frac{1}{2}\left(1 - \frac{\left|\int_0^T \tau_{\text{w}}\, dt\right|}{\int_0^T |\tau_{\text{w}}| dt}\right) \tag{3.14}$$

The OSI value varies from 0 to 0.5, where 0 represents the unidirectional flow with no cyclic variation of the WSS vector, and 0.5 signifies complete oscillatory flow with disturbed flow behavior. The flow behavior near the wall can be simple or disturbed based on the normal or diseased condition that changes the instantaneous WSS vector alignment with the TAWSS. Orientation and morphological changes of the endothelial cells are dependent on the magnitude and the direction of the shear stress. The time-averaged WSS vector affects the tendency of the endothelial cells to align in the flow direction in simple flows, which causes the favorable remodeling of the vessel wall [16]. On the other hand, an oscillating shear stress pattern due to disturbed flow or higher pulsatility can cause increased cyclic stress and elongation compared to simple flows, which might relate to cyclic fatigue in traditional materials such as steel and aluminum [35, 59]. Previous studies has used OSI in the arterial blood flow study [41, 32] and this index is introduced here since it influences the deposition of aerosol particles and the remodeling of the vessel wall [61].

3.8.4 Pressure drop

The pressure gradient from the mouth to the alveoli drives the airflow through the lungs. The airflow going through the airway depends on the pressure drop, which differs for normal and diseased conditions. A higher pressure drop indicates higher energy consumed to drive the flow through the airway vessel, indicating an obstructive disease. Thus, the pressure drop is necessary for evaluating either an airway vessel or the entire lung system. The pressure drop coefficient (C_p) is evaluated for all the cases to study the influence of boundary conditions at the inlet and is defined as

$$C_p = \frac{\Delta p}{\frac{1}{2}\rho v^2} = \frac{P_i - P_o}{\frac{1}{2}\rho v^2} \tag{3.15}$$

where P_i is the average inlet pressure, P_o is the average outlet pressure, v is the average velocity at the inlet, and ρ is the density of the fluid.

3.8.5 Statistical analysis

All the statistical analyses were performed with the software R, release 4.0.3 (www.r-project.org). Data are presented as mean $\pm$ standard deviation, and normality was assessed with the Shapiro-Wilk test. Independent samples two-tailed t-test were used to compare means of normally distributed variables and the Mann-Whitney U test is used for non-normally distributed data. A p-value less than 0.05 is considered as statistically significant for all test.

Chapter 4

Results

4.1 Mesh and time-step independence studies

In order to ensure final computed results are not dependent on the number of elements used for the CFD study, a mesh-independent study is conducted. The number of mesh elements was varied from coarse to fine (0.4M to 5.75M) with an element size of around 1% of the inlet diameter. One of the 10 patient-specific cases was taken for the study with output parameters as average velocity at the mid-plane of the trachea and TAWSS to test for the mesh convergence. The graphical results in the Figure 4.1 and quantitative data in Table 4.1 shows the convergence of results as the number of mesh elements increases. The average velocity and TAWSS calculated are within a tolerance of around <6%. So, considering a balance between the computational cost and accuracy of the solution mesh size of 1.27M was selected for the numerical study.

Table 4.1: Average Velocity at the mid-plane of trachea and TAWSS as a function of number of elements

Number of Elements	Average Velocity (m/s)	TAWSS (Pa)
0.40M	1.12	0.0183
0.75M	1.11	0.0181
1.27M	1.14	0.0163
2.35M	1.21	0.0164
5.75M	1.16	0.0165

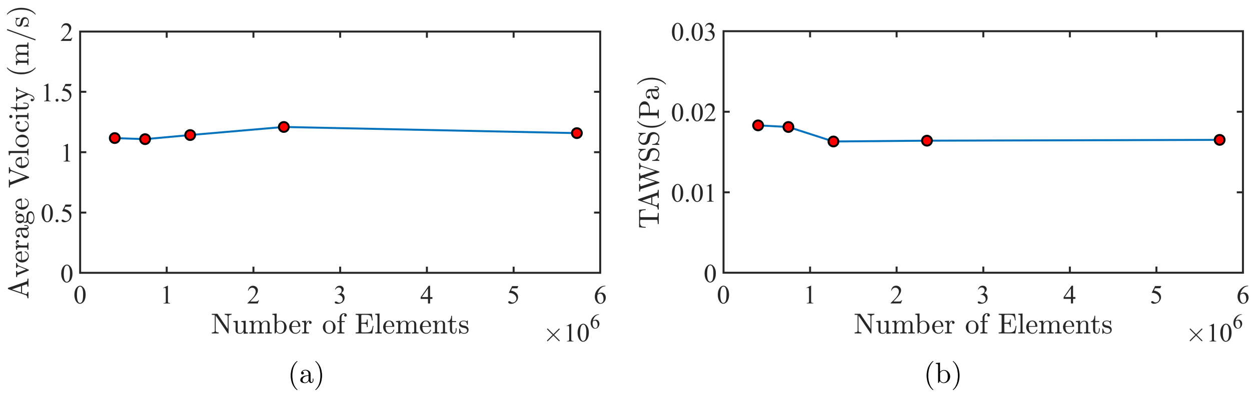

Figure 4.1: Mesh independent study quantifying a) Average velocity at the midplane of the trachea vs number of elements b) TAWSS vs the number of elements

The flow properties in an unsteady flow changes with time, so a time-step independent study is necessary to get the temporal accuracy and capture the dynamics of the flow system. Therefore, time-step independent study was conducted by varying time step size with 0.1 s, 0.01 s, 0.001 s, and 0.0001 s. TAWSS was evaluated with increasing time-step size to test for its independence. The mesh size used for the entire time-step independence study is 1.27M. Graphical representation in Figure 4.2 and quantitative result in the table 4.2 shows the convergence of the time-step size was within <5% error. Therefore, accounting for computational time and accuracy, a time-step size of 0.01 s was selected for the further study. Figure 3.1 shows the trachea model finalized after the mesh convergence study, which is exported to ANSYS Fluent® for simulations and post-processed to quantify velocity, pressure, and WSS.

Table 4.2: TAWSS evaluated with the increasing time-step size

Time-step size (s)	TAWSS (Pa)
0.0001	0.017
0.001	0.0171
0.01	0.0163
0.1	0.0147

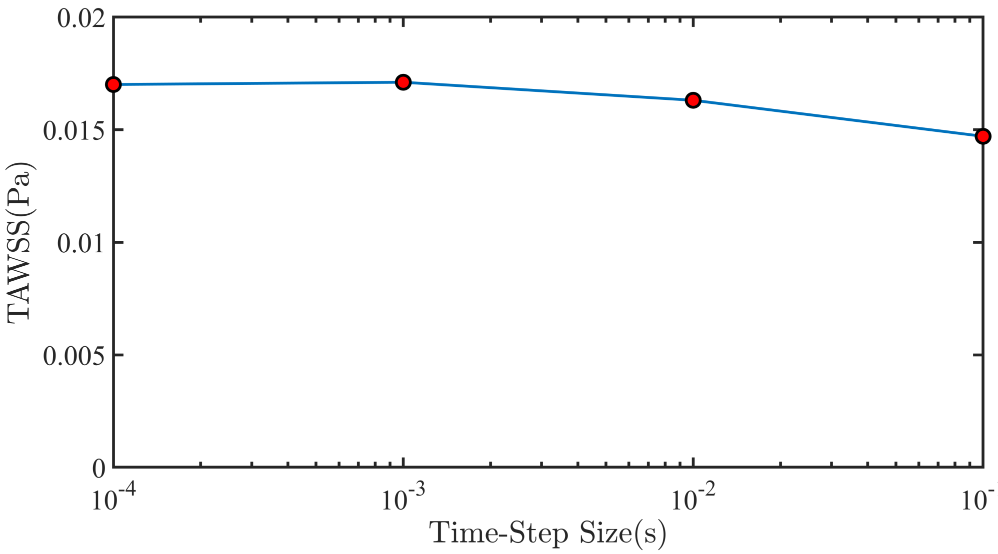

Figure 4.2: Time independence study quantifying TAWSS vs. time-step size in semilog plot

4.2 Patient-specific geometry

The extracted model of ten patient-specific geometry is shown in Figure 4.3 which provides a visualization of distinctive features of each geometry. The details of healthy patient characteristics was discussed in detail in the methods section. The normal case provides a similar reference to a number of healthy case geometry found in the literature [44, 17, 51, 47]. Realistic geometry was chosen for the study due to its complex flow features instead of the idealistic geometry. The Figure 4.4 shows the details of the case 3 patient-specific trachea, where the centerline seen in a) and f) part of the figure is extracted along the length of the trachea using VMTK software. The centerlines are the weighted shorted paths traced out between two points and are considered the descriptors of the vessel's shape. To further investigate the effect of the case 3 patient-specific geometry, 11 cross-sections were extracted along the centerline, including inlet and outlet plane, which were perpendicular to the centerline and equally spaced with 0.1 L spacing. The cross-sectional area plotted for all the length of the showed decrease in area till third cross-section and then increases from 3-6 cross-section and finally decreases until the 10^{th} cross-section that is plotted along the length of the trachea.

Figure 4.4 shows CSA, the curvature of the geometry, and average velocity along the length of the trachea evaluated at 11 cross-sections. The curvature of the geometry is evaluated using VMTK software along the centerline of the trachea which is reciprocal of the radius of curvature. As the CSA increases, velocity decreases and vice versa because mass is always conserved when fluid is in motion, which implies the product of area and velocity is constant, assuming that density doesn't alter. The curvature changes also fluctuate along the length of the trachea, which affects the secondary flow structure generation and spatial velocity peak distribution in the trachea.

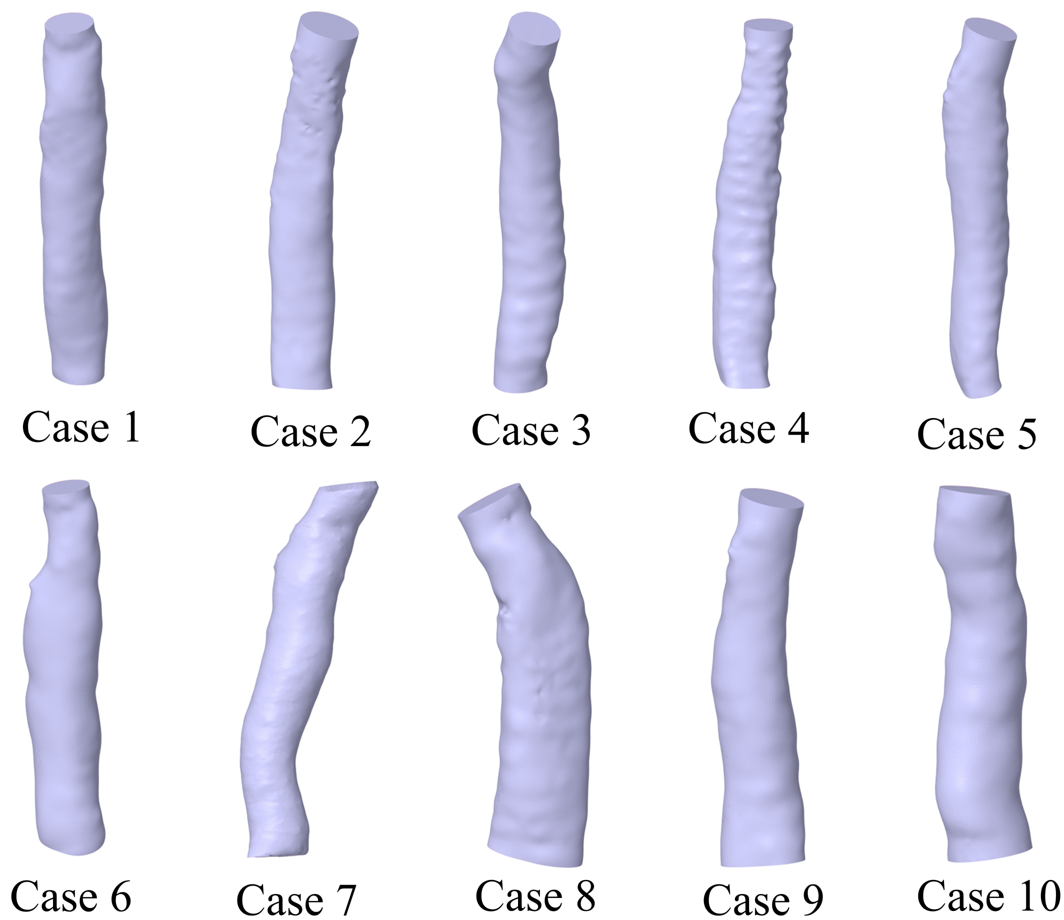

Figure 4.3: Patient-specific geometry shown in the sagittal view for all the ten patient cases analyzed in the study

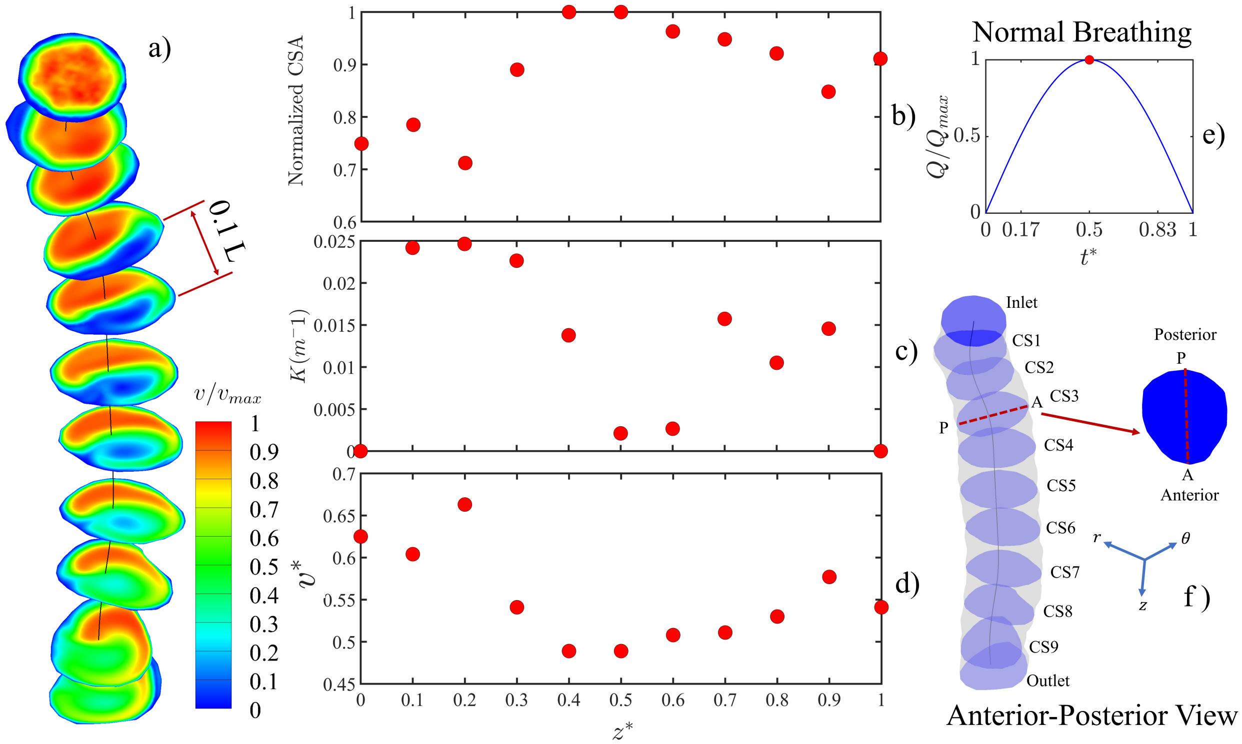

Figure 4.4: Patient Specific geometry of case 3 a) Velocity contour from inlet to outlet for 11 cross-sections with spacing of 0.1 L where L is the length of the centerline b) The cross-sectional area (CSA) normalized by maximum CSA along the centerline of the geometry c) The local Curvature of the trachea centerline d) Normalized average velocity at different cross-section of the trachea e) Peak flow curve with red dot showing the time point of the data f) Cross-section view along the length of the trachea showing Anterior-Posterior view

4.3 Effect of inlet velocity profiles on velocity and vorticity contours

The first aim of the study was to assess the influence of the inlet velocity profiles on the flow characteristics of the patient-specific healthy trachea. In this section, one patient data (Case 3) was investigated to study the influence of inlet velocity profiles on the velocity and vorticity contours. Both velocity and vorticity contours were explored in the sagittal plane, while only velocity was considered in the axial plane. This is because the sagittal plane provides more insight into the flow characteristics along the length of the trachea.

4.3.1 Axial plane

In order to study the effect of the inlet velocity profile in detail, velocity contour at five different slices perpendicular to the centerline were extracted at various locations along the length of the trachea represented as inlet, CS1, CS2, CS3, and outlet. The velocity contour was compared between the Parabolic, Womersley, flat, and Real velocity profiles for normal and rapid breathing cases. To study the unsteady effects for both normal and rapid breathing cases, velocity contours comparison was studied for three different time points $t^* = (0.17, 0.5, 0.83)$, where 0.5 corresponds to the peak flow rate and time point 0.17 and 0.83 correspond to half of the peak flow rate during acceleration and deceleration phase of inhalation. It should be noted that v/v_{max} is normalized by v_{max}, which is the maximum velocity in the flow domain for each inlet velocity profile case.

Normal breathing

Figure 4.5 shows the velocity contour plot at five different cross-sections along the length of the trachea as described in section 4.3 for normal breathing at the peak flow rate. As shown in the inlet cross-section, the Parabolic and Womersley profile has peak velocity at the central region of the cross-section. In contrast, the flat profile shows uniform velocity distribution, and the real profile from the experiment shows the non-uniform distribution. Looking at the CS1 cross-section, the flow patterns remain the same as the inlet cross-section but are deflected towards the geometry's posterior section. This deflection of the flow towards the posterior region is due to the curvature of the geometry. Further downstream, by comparing the cross-sections (CS2, CS3, and outlet) it is noted that all cases of inlet velocity profile shows no significant difference is observed in the velocity patterns. However, there are subtle differences can be observed between different cross-sections along the length of the trachea. Overall observation for CS2, CS3, and outlet cross-sections indicates that the flow patterns in parabolic, and Womersley profiles appear to be in better agreement with the real velocity profile close to the wall in comparison to the flat velocity profile. This observation is crucial as the velocity gradient near the wall determines the wall shear stress. In the distal part of the trachea input velocity effect diminishes and the flow is more dependent on the curvature in addition to the shape of the cross-section of the trachea [9].

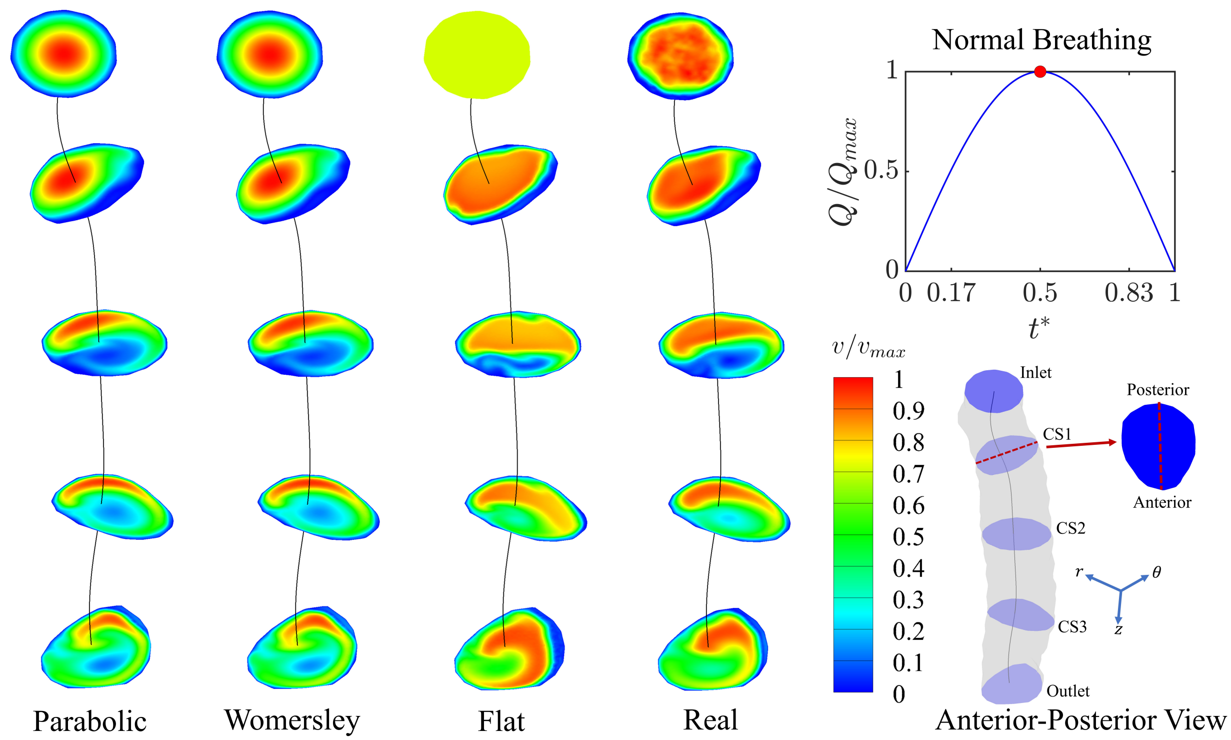

Figure 4.5: Velocity contour at time point $t^* = 0.5$ corresponding to peak flow rate at five different cross sections for normal breathing

The velocity contours for the two time points $t^* = 0.17$ and $t^* = 0.83$ are in better agreement with each other as shown for the acceleration and deceleration phase surrounding the peak inspiratory flow as shown in Figure 4.6 and Figure 4.7. The blue region away from the wall corresponds to slow moving fluid induced by the recirculation region which is referred to as the secondary flow. Observation of this secondary flow for the cross-section CS1-outlet differs from the time points $t^* = 0.17$ and $t^* = 0.83$ when compared to peak inspiratory time point ($t^* = 0.5$) since the flowrate is double at this time point. Overall comparison of the fast moving region and secondary flow for real velocity profile is close to parabolic and Womersley profile than flat profile for all the three time points.

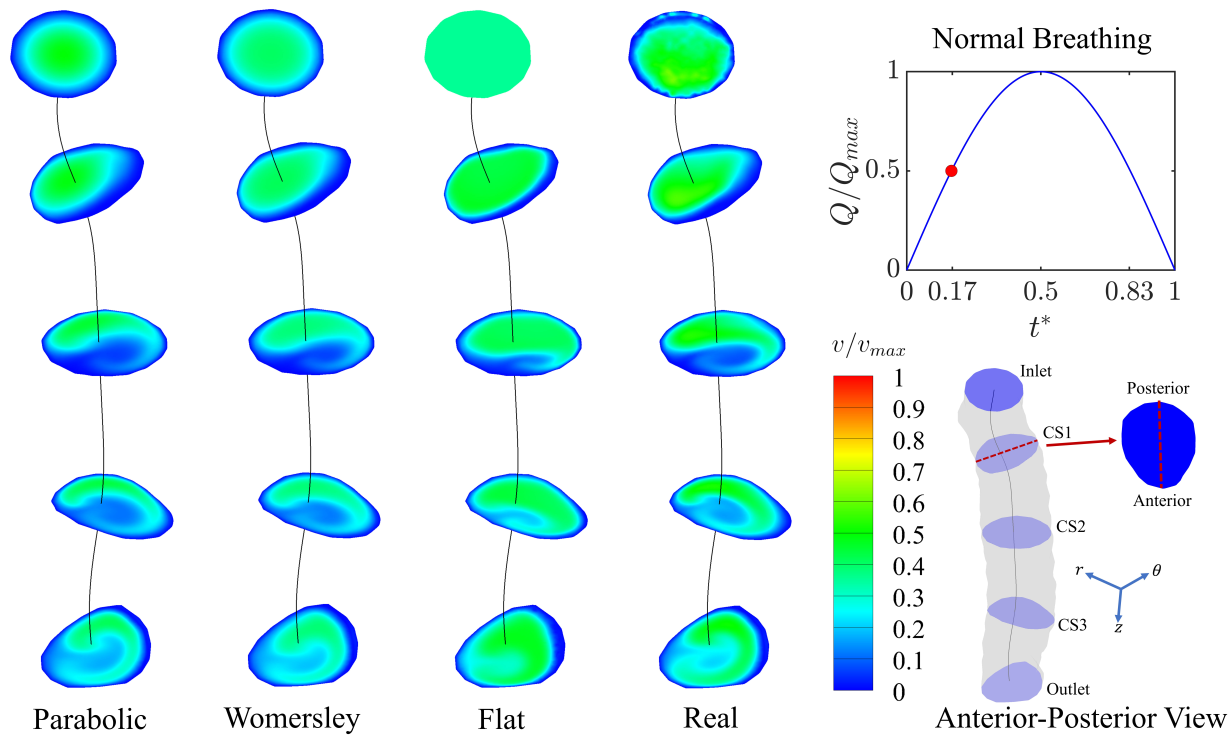

Figure 4.6: Velocity contour at time point $t^* = 0.17$ corresponding to half of peak flow rate at five different cross sections for normal breathing

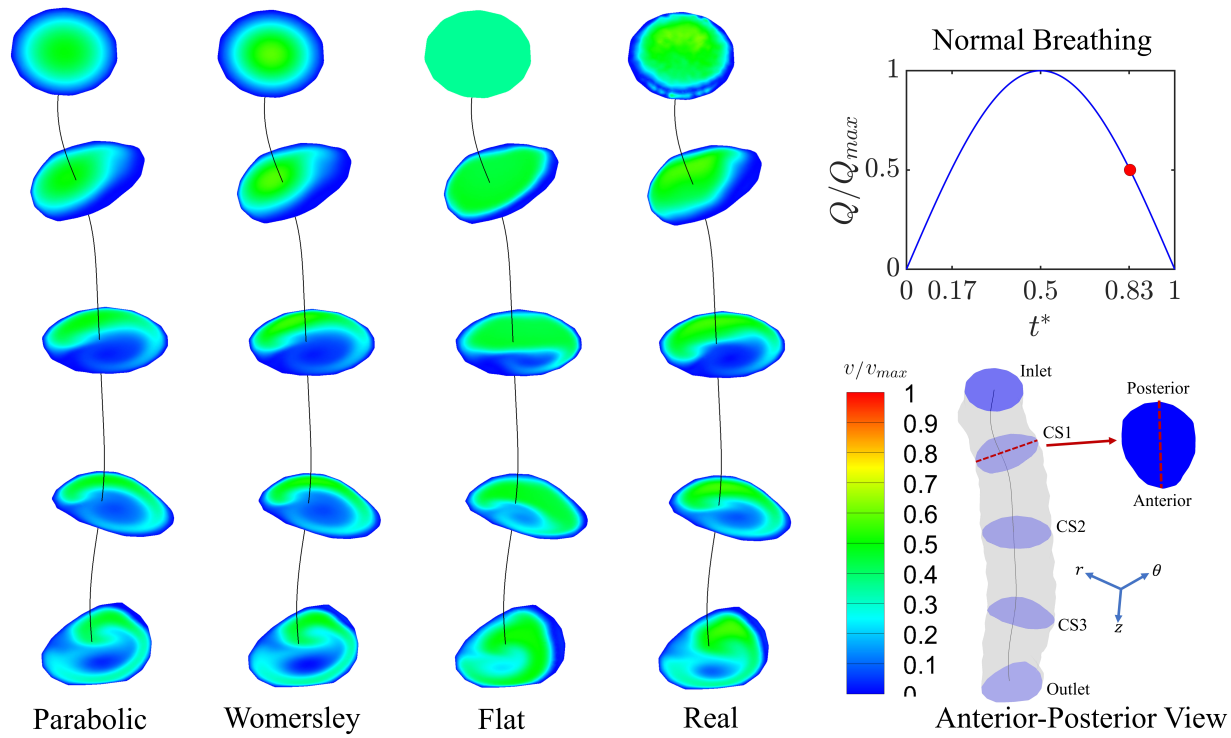

Figure 4.7: Velocity contour at time point $t^* = 0.83$ corresponding to half of peak flow rate at five different cross sections for normal breathing

Rapid breathing

Figure 4.8 shows the velocity contour plot at five different cross-sections along the length of the trachea as described in section 4.3 for rapid breathing at a peak flow rate. As shown in the inlet cross-section, the parabolic and Womersley profile has peak velocity in the central region of the cross-section while the flat profile shows uniform distribution of velocity, and the real profile from the experiment shows the non-uniform distribution of velocity. The key difference between normal and rapid breathing appears in Womersley profile with which it is more flatter than the parabolic case whereas the real profile has peak velocity at four corners of the inlet. This is due to the higher Womersley number, which in turn means higher pulsatility effects than normal breathing condition. Observation of CS1 cross-section shows that the flow patterns remain closely the same as the inlet cross-section but are deflected towards the posterior section of the geometry. As pointed out in normal breathing case, this deflection of the flow towards the posterior region is due to the effect of the change in curvature of the geometry. Further downstream, at the cross-sections (CS2, CS3, and outlet), comparing all cases of inlet velocity profile shows that real velocity is in good agreement with parabolic and Womersley profile than with flat velocity profile. Further observation of CS2, CS3 and outlet cross-sections, implied that the recirculation zone in parabolic and Womersley profile resembles close to real velocity profile in comparison to flat velocity profile. The major difference between the peak inspiratory time-point between the normal and rapid case is that the parabolic and Womersley profile velocity profile at the inlet are different from each other due to the higher Womersley number for the rapid case. In the distal part of the trachea same observation as normal breathing is observed that is input velocity effect diminishes and the flow is more dependent on the curvature in addition to the shape of the cross-section of the trachea [9].

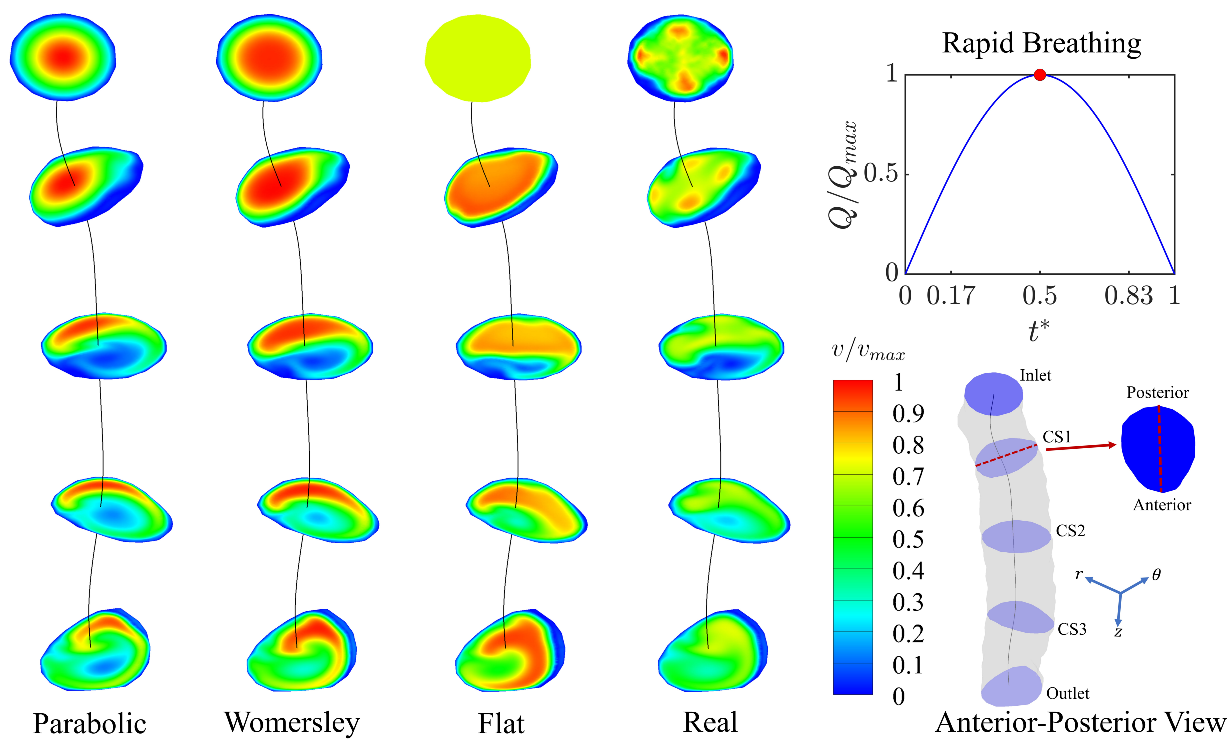

Figure 4.8: Velocity contour at time point $t^* = 0.5$ corresponding to peak flow rate at five different cross section in different cross sections for rapid breathing

The velocity contours show that there are differences observed between the two-time points corresponding to the acceleration and deceleration phase surrounding the peak inspiratory time-point as shown in Figure 4.9 and Figure 4.10. In the inlet cross-section, it can be observed that there is an asymmetry in the inlet velocity profile for the Womersley profile case due to rapid variations in time which was not observed in normal breathing condition. Velocity contour at cross-section CS1 for all cases is more uniformly distributed as in the initial inlet condition except the wall effect evident from slow moving fluid near the wall because time-point at $t^* = 0.17$ corresponds to $t^* = 0.17$ in dimensional which is very less. The time-point corresponding to $t^* = 0.83$ during the deceleration phase shows the secondary flow for CS2-outlet cross-sections are closer to the parabolic and Womersley case when compared to the flat profile.

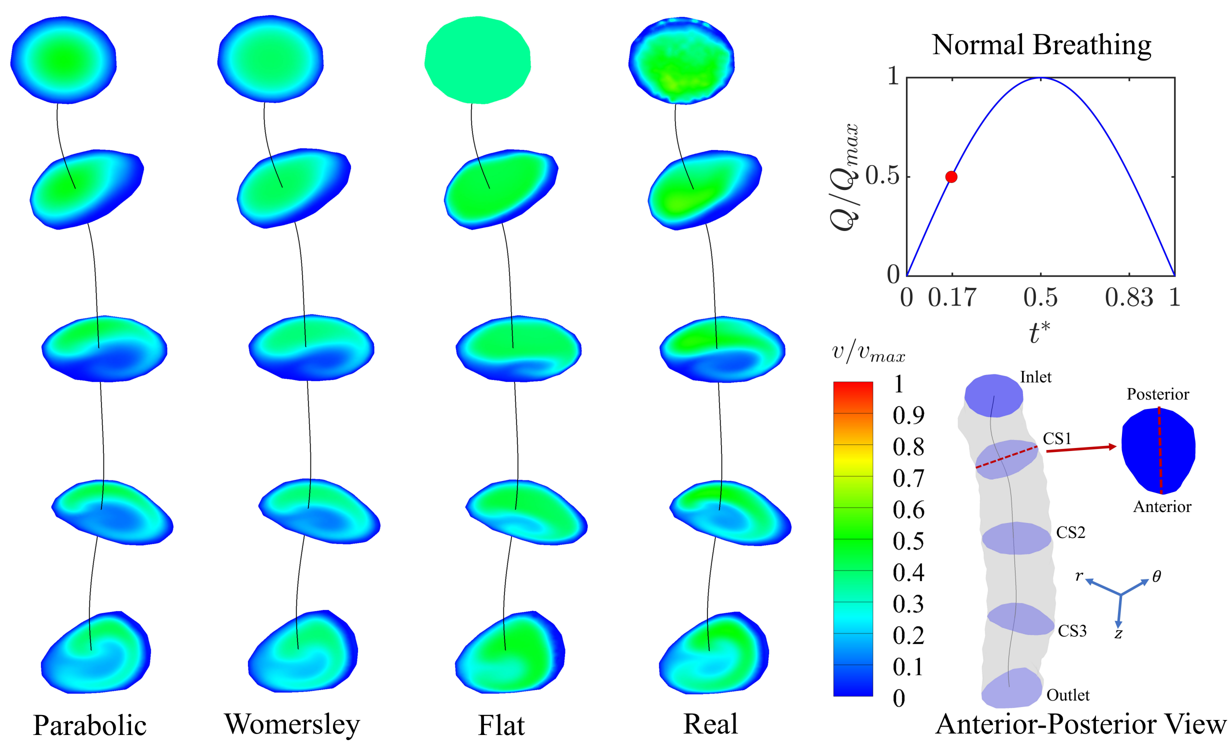

Figure 4.9: Velocity contour at time point $t^* = 0.17$ corresponding to half of peak flow rate at five different cross sections for rapid breathing

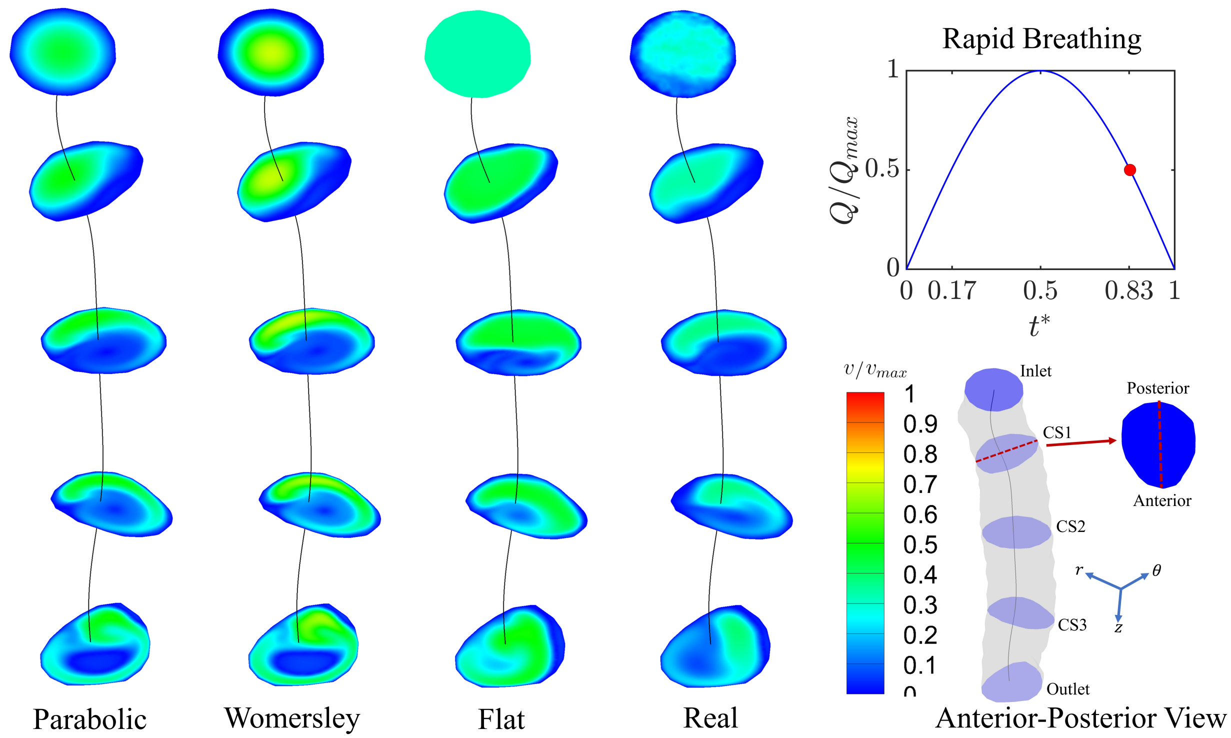

Figure 4.10: Velocity contour at time point $t^* = 0.83$ corresponding to half of peak flow rate at five different cross sections for rapid breathing

4.3.2 Sagittal plane

This result section discusses the effect of different inlet velocity profiles on tracheal velocity and vorticity contours in the sagittal plane for one patient-specific geometry (case 3). The vorticity magnitude is normalized by the inlet diameter and maximum domain velocity for each inlet velocity profile, while the normalization of velocity is described in the methods section. The sagittal plane provides a better look at how velocity and vorticity contours change along the length of the trachea compared with the axial plane that shows cross-sectional data. The peak flow was chosen to see the differences in the flow features in the sagittal plane between the flat, parabolic, Womersley, and real inlet velocity profiles for normal and rapid breathing cases.

Normal breathing

Figure 4.11 and Figure 4.12 show the contours of velocity and vorticity magnitude in the sagittal plane for four different inlet velocity profiles for normal breathing. From the sagittal plane cross-section observed in the Figure 4.11, it can be seen that patient-specific geometry narrows and then increases with the change in curvature along the length of the trachea, leading to a large separation region. Based on the observation of the low velocity separation region indicated by the blue color in the Figure 4.11 shows that the real velocity profile closely resembles with parabolic and Womersley profile compare to flat profile for normal case.

Vorticity is the curl of the velocity due to the velocity gradient and is defined as twice of angular velocity. Vorticity is typically higher near the wall, which can be observed in the Figure 4.12 and diffuse into the flow because of the viscosity. The high vorticity closer to the wall influences the wall shear stress of the trachea which is the quantity of interest from clinical perspective and application. The change of the patient-specific vessel cross-section and curvature along the length causes the large vorticity region, which is elongated and confined along the edge of the separated region as seen in Figure 4.12. It is evident from the Figure 4.12 that parabolic and Womersley profile vorticity region near the wall is identical and resembles more close to the real profile. But the flat profile has distinctively different vorticity at the wall when compared to other velocity profile.

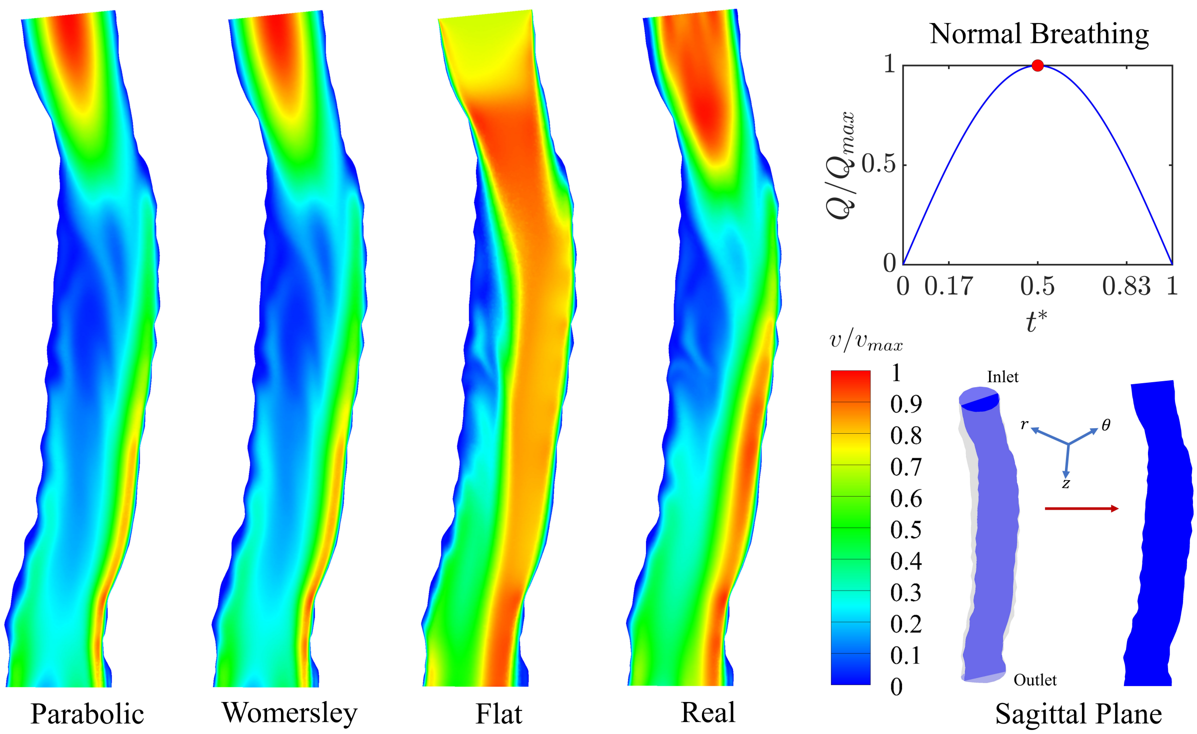

Figure 4.11: Velocity contours plotted for a sagittal plane for normal breathing condition

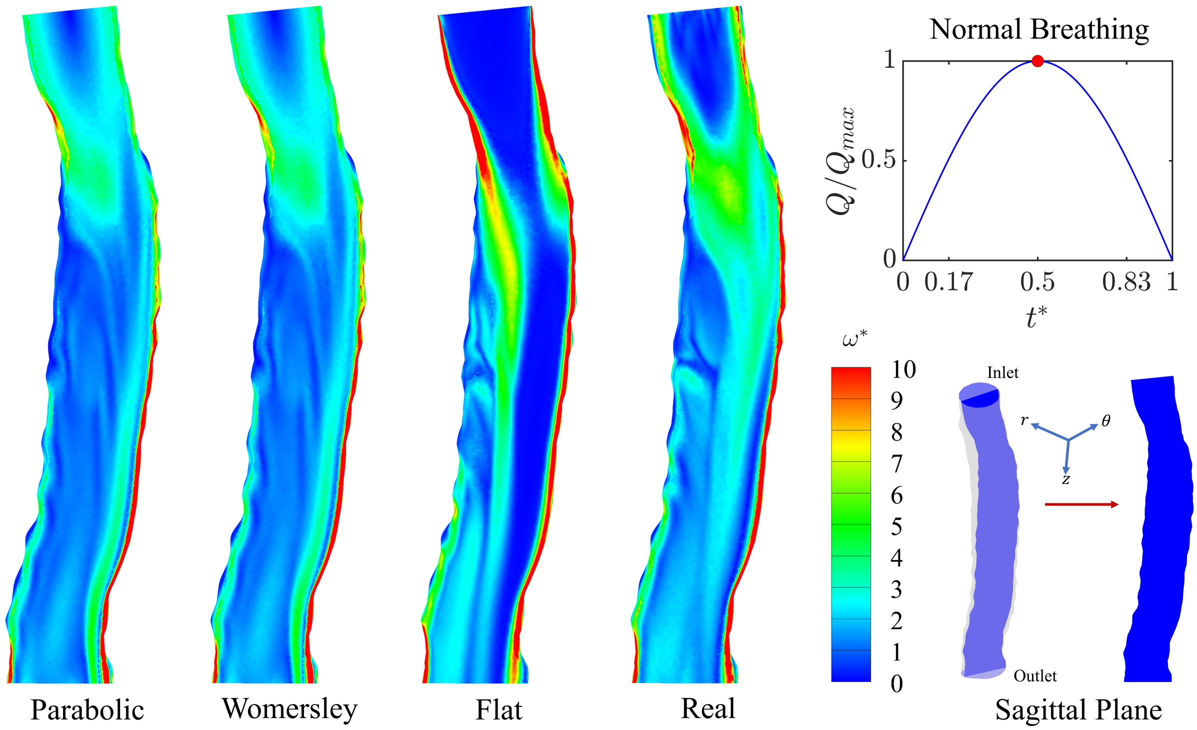

Figure 4.12: Contours of vorticity magnitude plotted in a sagittal plane normalized by the inlet of the trachea diameter and maximum velocity in the domain for each inlet velocity profile for normal breathing condition

Rapid breathing

Figure 4.13 and Figure 4.14 show the contours of velocity and vorticity magnitude in the sagittal plane for four different inlet velocity profiles for rapid breathing. The separated region is identified by a low-velocity region, indicated by a blue color in the Figure 4.13, similar to the normal breathing condition in Figure 4.11. However, in rapid breathing conditions, the separation region for the real profile is closer to the Womersley profile than the parabolic profile. Similarly, when the separated region for the flat profile is compared to the other veolcity profile, it is observed to be significantly different.

As the same patient-specific case is analyzed for rapid breathing conditions similar to normal breathing, the flow passes through the reduction in cross-section with curvature change which causes the separation of flow and high vorticity region. In contrast to normal breathing conditions, the parabolic and Womersley profile shows a slightly different vorticity region for the rapid breathing condition that can be observed in the Figure 4.14. Womersley profile vorticity region at the wall resembles close to real profile more than parabolic profile for rapid breathing condition. Further comparison of the other three idealistic velocity profiles shows that the flat profile has significantly different vorticity contours.

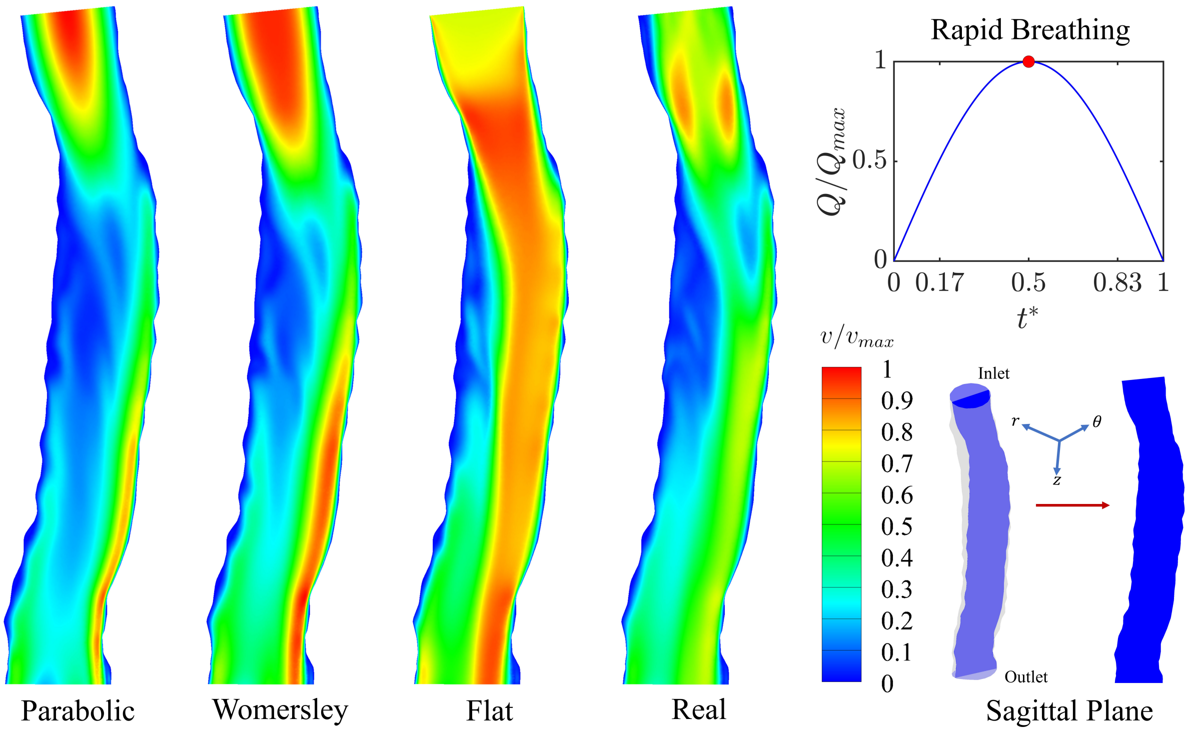

Figure 4.13: Velcoity contours plotted for a sagittal plane for rapid breathing condition

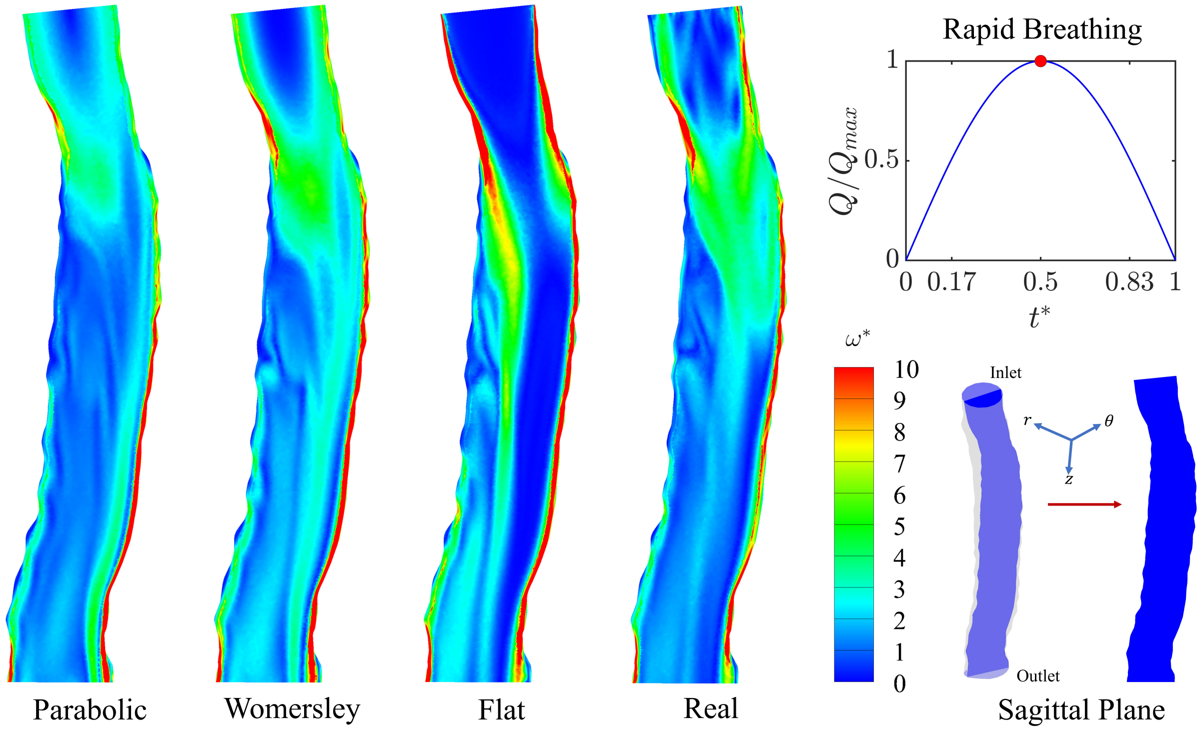

Figure 4.14: Contours of vorticity magnitude plotted in a sagittal plane normalized by the inlet of the trachea diameter and maximum velocity in the domain for each inlet velocity profile for rapid breathing condition

4.4 Effect of breathing frequencies

The second aim of this study was to identify the closest surrogate model for the patient-specific simulation for normal and rapid breathing conditions. In this section, all the ten patient cases were explored based on the TAWSS, OSI, and pressure drop behavior to study these clinically relevant metrics. These metrics were evaluated and plotted in the bar graph to compare the idealized profile results with real profiles for normal and rapid breathing conditions.

4.4.1 Time-Averaged Wall Shear Stress (TAWSS)

The flow through the trachea showed that airflow did not move at the same velocity in the whole cross-section of the geometry. The airflow in the trachea is faster in the central region and slower at the trachea wall. This observed phenomenon is due to the fluid friction that is the viscosity between the fluid itself and the fluid with the wall. The tangential force created due to the fluid friction is known as wall shear stress. This wall shear stress was spatially as well as temporally averaged over the inhalation phase. In order to compare patient case samples between different inlet velocity profiles, the TAWSS was normalized by inlet velocity and diameter for each inlet profile. The normalized TAWSS is defined as

$$\text{Normalized TAWSS}\,(\tau^*) = \frac{\text{TAWSS}}{\mu \frac{u_i}{D_i}} \tag{4.1}$$

where u_i is the average inlet velocity and D_i is the inlet diameter.

Figure 4.15 and Figure 4.16 shows the comparison of the TAWSS for ten patient-specific cases between each inlet velocity profile. It is observed from Figure 4.15 and Figure 4.16 that the flat profile predicts higher TAWSS when compared to other inlet velocity profiles for all the patient-specific cases for both normal and rapid breathing conditions. Also, the parabolic and Womersley profile has very close prediction of TAWSS with real velocity profile for all patient cases, which is evident in the Figure 4.15 and Figure 4.16. Table 4.3 and Table 4.4 shows the tabulated percentage difference , E_{TAWSS}, between idealized inlet velocity profile with real profile condition, which is calculated by using

$$E_{\text{TAWSS}} = \left(\frac{|\tau^*_{\text{ideal}} - \tau^*_{\text{real}}|}{\tau^*_{\text{real}}} \right) \times 100\% \tag{4.2}$$

where τ^*_{real} is normalized TAWSS for real velocity profile and τ^*_{ideal} is normalized TAWSS for idealized velocity profile (Parabolic, Womersley and Flat). The idealized inlet velocity profile affects the calculation of TAWSS for normal breathing, on average, 8.65 ± 8.83%, 8.48 ± 6.51% and 43.67 ± 15.84% for the parabolic, Womersley, and flat profiles, respectively. Similarly, the TAWSS calculation is affected for rapid breathing conditions, on average, 8.71 ± 7.40%, 5.33 ± 7.79%, and 30.06 ± 20.99% for the parabolic, Womersley, and flat profiles, respectively. A further observation of the average of the data shows that the absolute difference of E_{TAWSS} between real vs. parabolic and real vs. Womersley for normal breathing is 0.17 %, which is less than the 3.38 % difference for rapid breathing.

Figure 4.17 shows the box and whisker plot comparing three different idealized velocity profiles with real profiles for normal and rapid breathing conditions for all the ten cases of patient-specific geometry. No significant difference was observed between the real velocity profile and the other three velocity profiles ($p > 0.05$). However, the mean difference between the flat velocity profile with respect to parabolic, Womersley, and real velocity profile was greatest. A similar observation was found in both the normal and rapid breathing cases. It indicates that a flat profile provides a significant difference in the result while the parabolic and Womersley profile is closer to the real velocity condition.

Table 4.3: TAWSS percentage difference evaluated for idealized inlet velocity profile compared with real velocity profile in normal breathing condition

	E_{TAWSS} (%)		
Cases	Real vs. Parabolic	Real vs. Womersley	Real vs. Flat
Case 1	3.87	6.75	65.59
Case 2	0.85	3.21	23.52
Case 3	5.66	5.52	32.41
Case 4	17.42	15.57	66.90
Case 5	5.15	5.18	24.85
Case 6	6.39	5.74	52.33
Case 7	31.63	24.78	50.84
Case 8	7.11	9.45	28.00
Case 9	0.70	1.65	56.57
Case 10	7.75	6.95	35.64
Average	8.65	8.48	43.67
Standard Deviation	8.83	6.51	15.84

Table 4.4: TAWSS percentage difference evaluated for idealized inlet velocity profile compared with real velocity profile in rapid breathing condition.

	E_{TAWSS} (%)		
Cases	Real vs Parabolic	Real vs Womersley	Real vs Flat
Case 1	24.98	28.16	88.31
Case 2	9.22	1.08	26.10
Case 3	5.54	0.92	11.09
Case 4	20.16	6.72	39.16
Case 5	1.37	1.09	17.69
Case 6	4.46	2.36	21.32
Case 7	3.29	3.27	15.21
Case 8	4.38	1.81	20.12
Case 9	4.22	3.54	32.54
Case 10	9.57	4.29	29.09
Average	8.71	5.33	30.06
Standard Deviation	7.40	7.79	20.99

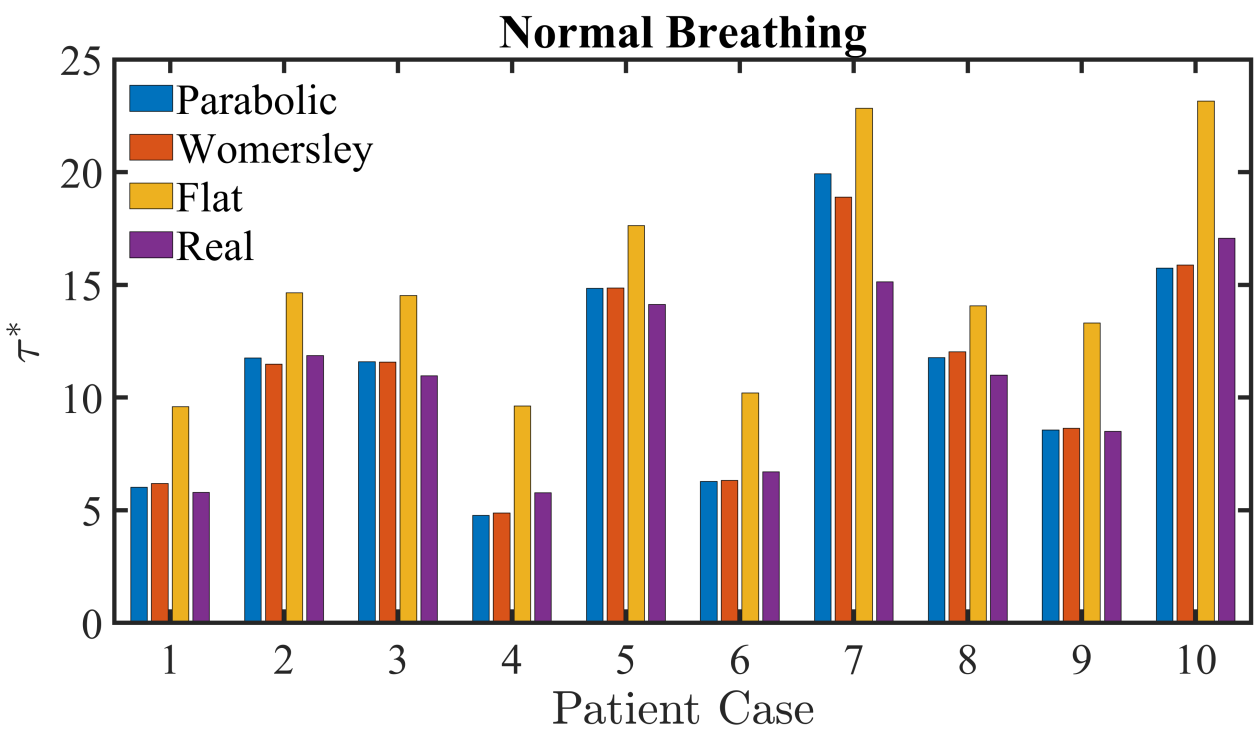

Figure 4.15: Bar graph of ten patient case simulations showing the comparison for TAWSS resulting from the Parabolic, Womersley, Flat and Real velocity profiles for normal breathing condition

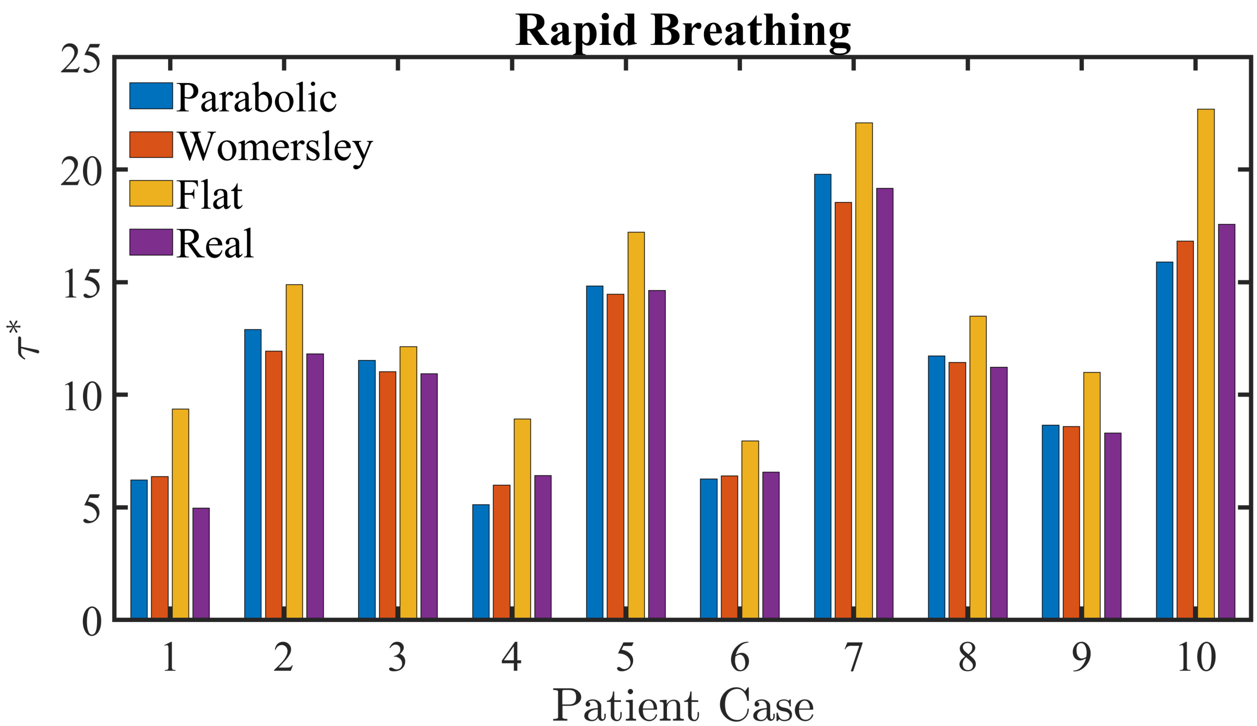

Figure 4.16: Bar graph of ten patient case simulations showing the comparison for TAWSS resulting from the Parabolic, Womersley, Flat and Real velocity profiles for rapid breathing condition

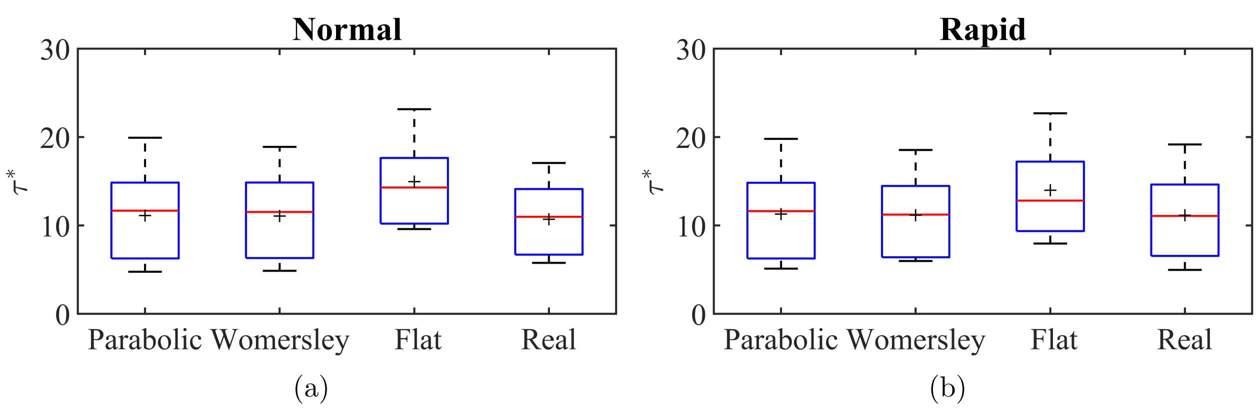

Figure 4.17: Box and whisker plots for TAWSS resulting from the Parabolic, Womersley, Flat and Real velocity profiles. + in each of the box and whisker plots of the TAWSS represents the mean value of the data

4.4.2 Oscillatory Shear Index (OSI)

Evaluation of OSI implies that instantaneous WSS vectors fluctuate significantly with the time-averaged TAWSS direction at the calculated point during the whole cycle of the inhalation phase. Therefore, OSI is introduced to account for the oscillatory flow disturbances that influence the flow field. A high value of OSI indicates the high flow complexity where the flow has higher oscillatory flow disturbances. Figure 4.18 and Figure 4.19 shows the comparison of the OSI for ten patient-specific cases between each inlet velocity profile. It is observed from Figure 4.18 and Figure 4.19 that the flat profile predicts lower OSI when compared to other inlet velocity profiles for all the patient-specific cases for both normal and rapid breathing conditions. Also, the parabolic and Womersley profile has a very close prediction of OSI with real velocity profile for all the patient cases, which is evident in the Figure 4.15 and Figure 4.16. Table 4.5 and Table 4.6 shows the percentage difference, E_{OSI}, of OSI between idealized inlet velocity condition compared to real profile condition, which is calculated by using

$$E_{\mathrm{OSI}} = \left(\frac{|\mathrm{OSI}_{\mathrm{ideal}} - \mathrm{OSI}_{\mathrm{real}}|}{\mathrm{OSI}_{\mathrm{real}}} \right) \times 100\% \tag{4.3}$$

where $\mathrm{OSI}_{\mathrm{real}}$ is Oscillatory shear index evaluated for real velocity profile and $\mathrm{OSI}_{\mathrm{ideal}}$ are oscillatory shear index evaluated for idealized velocity profile (Parabolic, Womersley, and Flat). The idealized inlet velocity profile affects OSI calculations for normal breathing, on average, 23.61 ± 18.03 %, 28.50 ± 25.25 %, and $42.87 \pm 21.50\%$ for the parabolic, Womersley, and flat profiles, respectively. Similarly, the OSI calculation is affected by rapid breathing, on average, $25.43\pm$ 13.71%, 18.40 ± 19.38 %, and $44.85 \pm 16.70\%$ for the parabolic, Womersley, and flat profiles, respectively. A further observation of the data shows that the absolute difference of the average OSI percentage difference between real vs. parabolic and real vs. Womersley for normal breathing is 4.89 %, which is less than the 7.03 % difference for rapid breathing.

Statistical analysis for OSI resulting from the four inlet velocity profiles were computed for all the ten cases of the patient-specific geometry and summarized in the Figure 4.20 as a box and whisker plots. No significant difference was observed between the real velocity profile and the other three velocity profiles ($p > 0.05$). However, the mean difference between the flat velocity profile with respect to parabolic, Womersley, and real velocity profile was greatest. A similar observation was found in both the normal and rapid breathing cases. It indicates that a flat profile provides a significant difference in the result while the parabolic and Womersley profile is closer to the real velocity condition.

Table 4.5: Percentage difference evaluated for OSI for idealized inlet velocity profile compared with real velocity profile for normal breathing condition

	E_{OSI} (%)		
Cases	Real vs Parabolic	Real vs Womersley	Real vs Flat
Case 1	16.48	24.08	29.90
Case 2	1.06	5.97	26.81
Case 3	37.86	45.39	10.51
Case 4	12.50	7.49	33.11
Case 5	70.77	83.30	77.16
Case 6	23.12	62.12	52.15
Case 7	21.61	18.62	32.75
Case 8	20.86	21.17	83.12
Case 9	18.03	4.59	35.76
Case 10	13.77	12.22	47.46
Average	23.61	28.50	42.87
Standard Deviation	18.03	25.25	21.50

Table 4.6: Percentage difference evaluated for OSI for idealized inlet velocity profile compared with real velocity profile for rapid breathing condition

	E_{OSI} (%)		
Cases	Real vs Parabolic	Real vs Womersley	Real vs Flat
Case 1	34.11	17.92	53.11
Case 2	36.63	2.13	56.47
Case 3	22.91	14.09	34.60
Case 4	27.18	5.45	42.29
Case 5	41.93	68.08	31.93
Case 6	44.33	3.15	61.89
Case 7	7.44	13.63	61.12
Case 8	13.17	30.13	37.11
Case 9	1.62	29.11	7.60
Case 10	25.01	0.24	62.33
Average	25.43	18.40	44.85
Standard Deviation	13.71	19.38	16.70

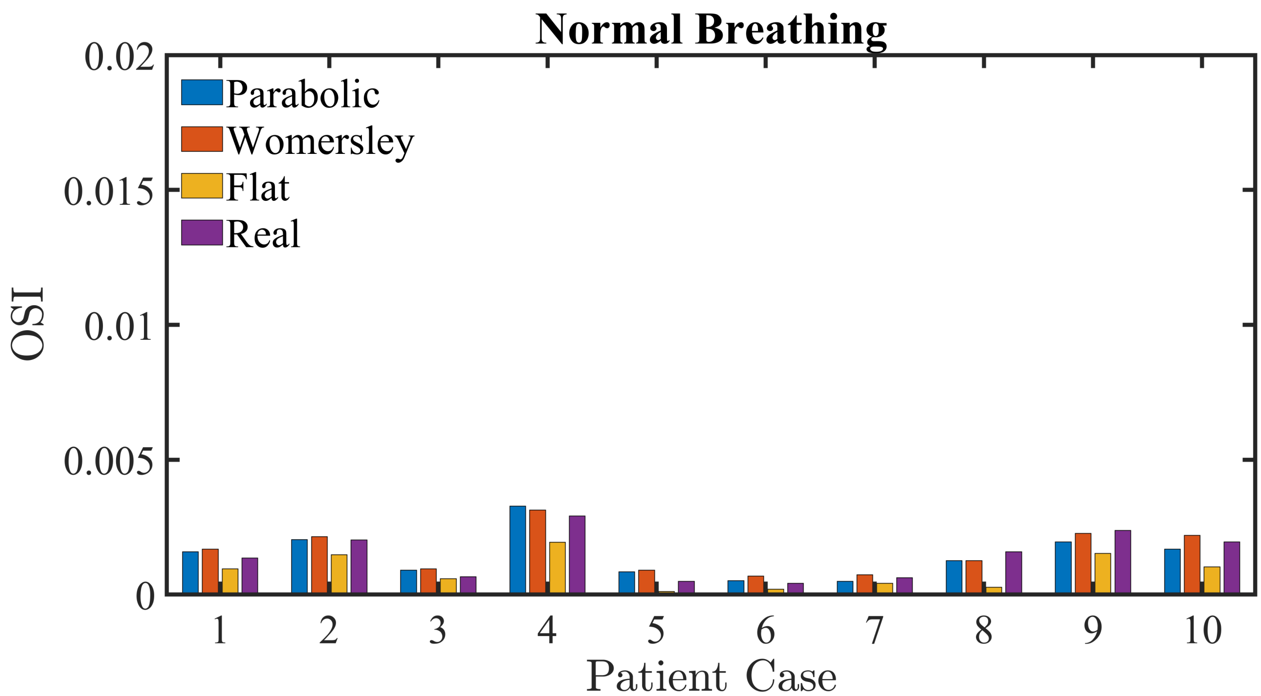

Figure 4.18: Bar graph of ten patient case simulations showing the comparison for OSI resulting from the Parabolic, Womersley, Flat, and Real velocity profiles for normal breathing condition

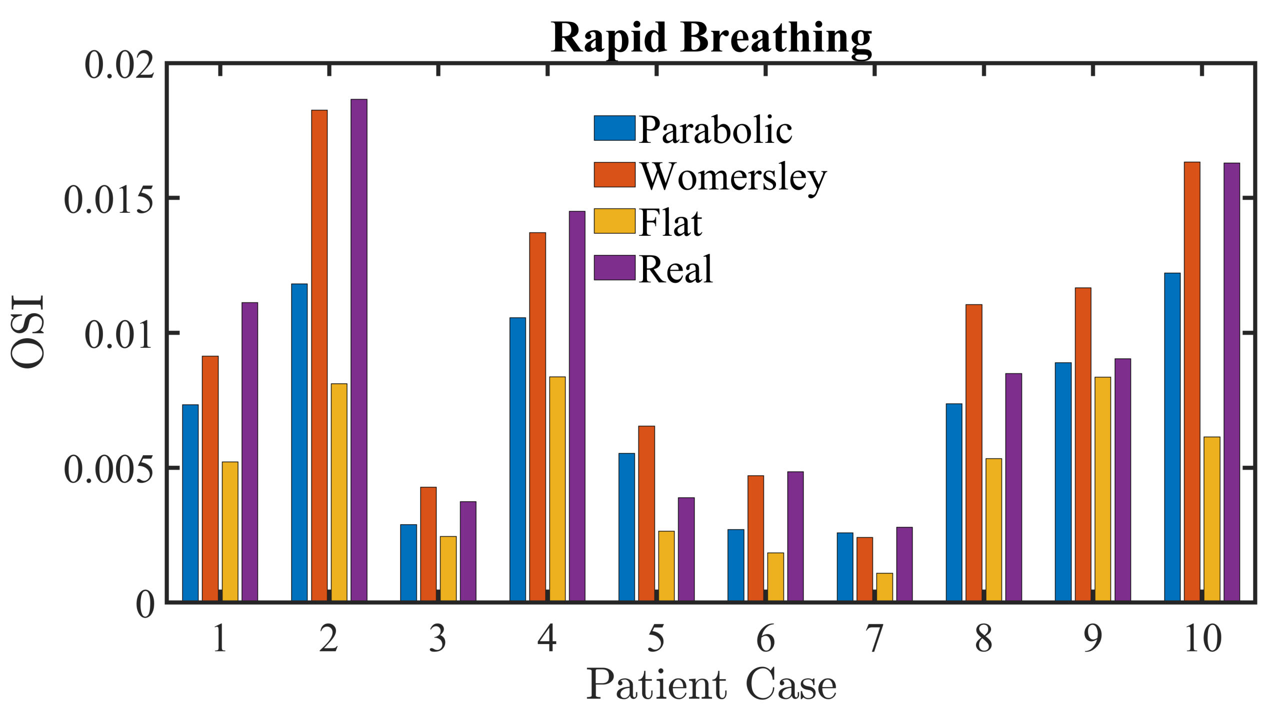

Figure 4.19: Bar graph of ten patient case simulations showing the comparison for OSI resulting from the Parabolic, Womersley, Flat and Real velocity profiles for rapid breathing condition

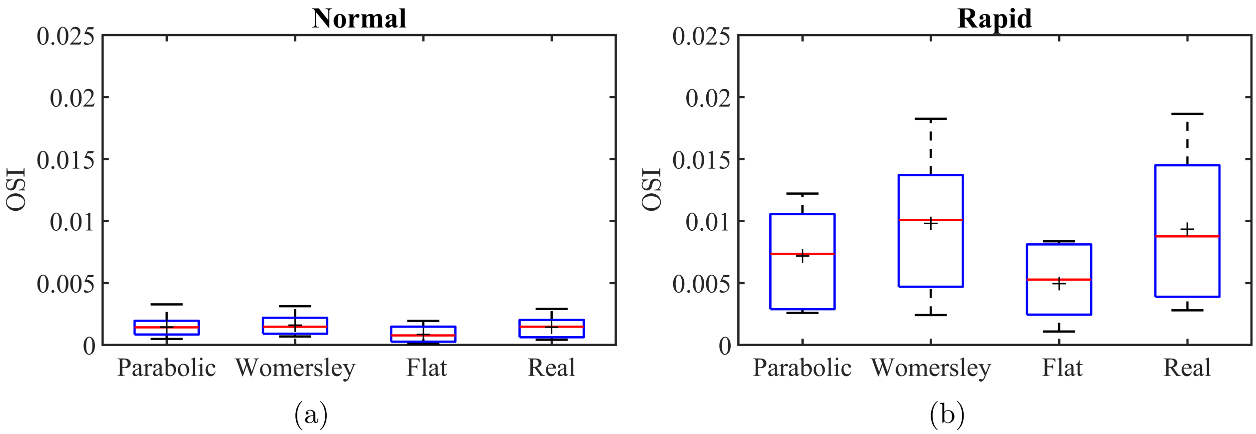

Figure 4.20: Box and whisker plots for oscillatory shear index resulting from the Parabolic, Womersley, Flat, and Real velocity profiles. + in each of the box and whisker plots of the OSI represents the mean value of the data

4.4.3 Pressure drop behaviour

It is essential to understand the pressure drop behaviour as it is the driving force of the breathing process. The ratio of pressure drop to the flow rate will give the resistance of the flow. The higher resistance means the obstructive breathing and is the indication of disease condition. Therefore, it is important to understand the behaviour of the pressure drop due to the imposed boundary condition. Figure 4.21 and Figure 4.22 shows the bar graph of pressure drop coefficient for all cases between the different inlet velocity profiles for normal and rapid breathing conditions. It can be observed that pressure drop coefficient between the real, Womersley and parabolic profile are almost similar for all the patient-specific cases for both normal and rapid breathing condition. However, the C_P due to flat profile is greater and in most of the cases it is more than 100% of that observed in other inlet velocity profiles. Therefore the use of flat profile will lead to significant deviation of the results from real profile.

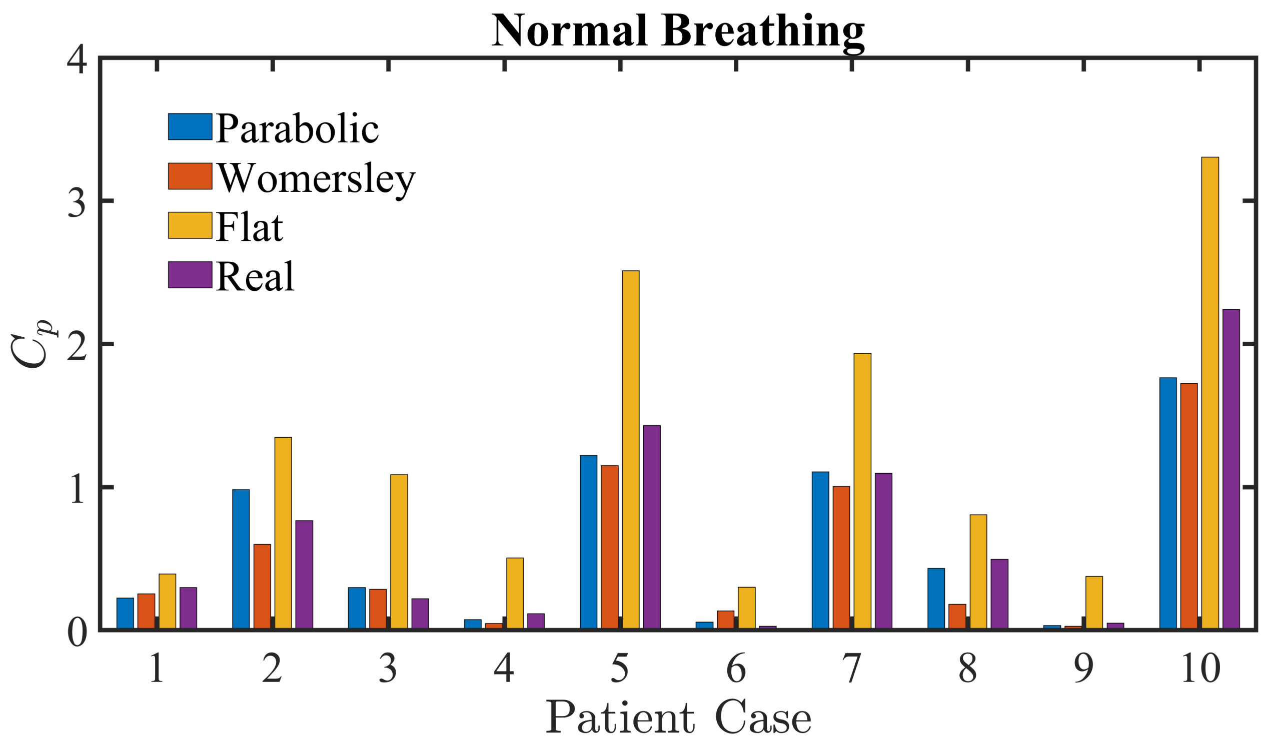

Figure 4.21: Bar graph of pressure drop coefficient for normal breathing for all ten patient cases

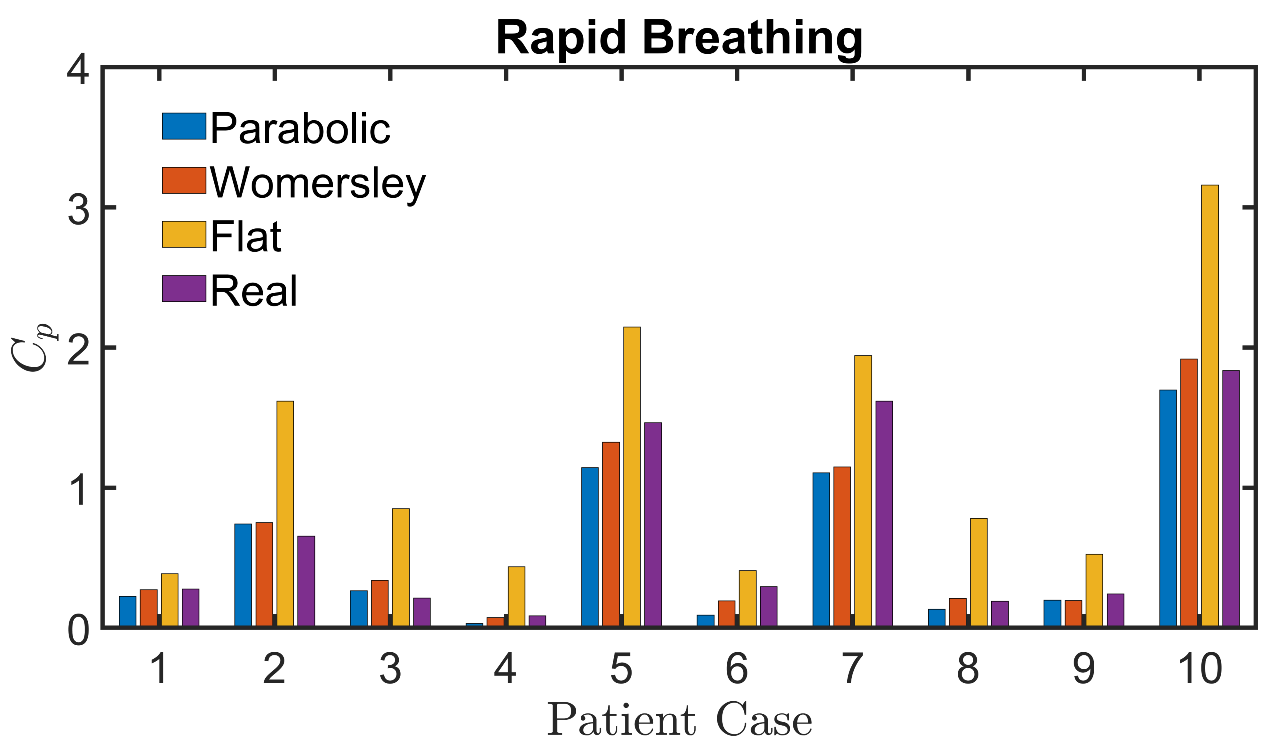

Figure 4.22: Bar graph of pressure drop coefficient for rapid breathing for all ten patient cases

4.5 Straight pipe simulation

The evaluation of percentage change for TAWSS (E_{TAWSS}) for all patient cases showed that E_{TAWSS} varies from patient to patient. The patient-specific geometrical factors could be responsible for the variations between the patient cases. The geometric variability of the trachea is evident from variations in curvature and cross-sectional area along its length which can be visually observed from the Figure 4.3. If observed closely, the patient cases are an addition of complexity to the straight pipe with these geometrical factors like curvature and cross-sectional variation along the length. Therefore, straight pipe simulation results can be used as a reference to compare patient-to-patient case variation since each patient case is unique in its geometric nature. Also, the idealized (flat, parabolic, and Womersley) profiles used in this study are derived as the solution to the straight pipe, and the simulation results are free from the effect of this geometric complexity. The simulation results are further discussed in the next paragraph and compared with patient-specific cases.

The straight pipe geometry was constructed in SolidWorks® with a diameter of 14.36 mm and a length of 100.08 mm for the simulation, which falls in the range of tracheal geometry [38]. This simulation was carried out ANSYS FLUENT® under the same conditions described in the methods section for patient-specific cases, with Reynolds number 2122 and Womersley number 2.42 for normal and 4.81 for rapid conditions. The TAWSS was evaluated and compared between the inlet velocity profile for both normal and rapid conditions, which is plotted as the bar graph in the Figure 4.23. The comparison of the straight pipe result with all patient cases for normal and rapid breathing is shown in the appendix section with Figure A.1 and Figure A.2. The Equation 4.3 was evaluated to compare the TAWSS percentage difference between real velocity profile and the idealized profiles. This comparison showed that the idealized inlet velocity profile affects the calculation of TAWSS for normal breathing by 20.53%, 18.60%, and 93.60% for parabolic, Womersley, and flat profiles, respectively. Similarly, the TAWSS calculation for rapid breathing conditions was affected by 23.76%, 8%, and 61.37% for the parabolic, Womersley, and flat profiles. In rapid breathing, the simulation result shows that Womersley profile better approximates the real profile with only 8% E_{TAWSS} difference. In contrast, in normal breathing, both the parabolic and Womersley profiles are good approximations of the real profile with 20.53% and 18.60% E_{TAWSS} difference. The patient cases shows small to large deviation of E_{TAWSS} when compared with straight pipe which is shown in Figure A.1 and Figure A.2 in appendix section. The reason of this deviation is due to the patient-specific variability of the geometry. Therefore, an idealized geometry with each geometrical factor can be constructed and studied to understand the affect of patient-specific nature in the results.

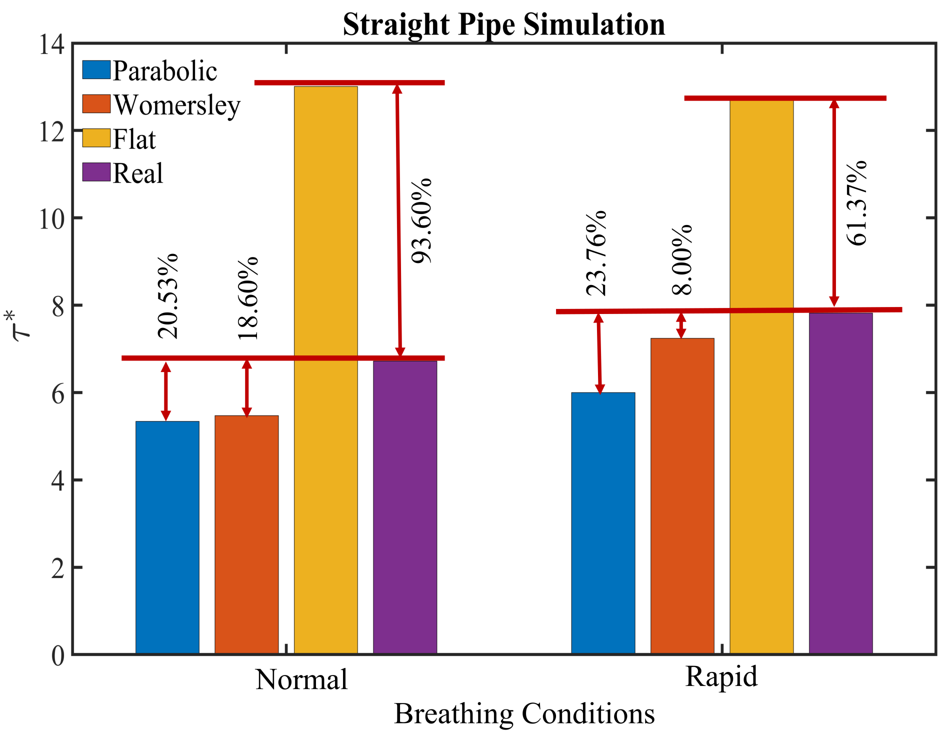

Figure 4.23: Bar graph of straight pipe simulation showing the comparison for TAWSS resulting from the Parabolic, Womersley, Flat, and Real velocity profiles for normal and rapid breathing condition

Chapter 5

Discussion

CFD has been used to study the flow dynamics of airflow through the airway structure using clinically relevant metrics. However, simplified assumptions are used in the absence of suitable boundary conditions, such as the flat, parabolic, and Womersley profile at the tracheal inlet for patient-specific simulations. The use of an idealized inlet velocity profile as a surrogate model is either due to the lack of patient-specific flow data or computational limitations. This study analyzed the qualitative airflow characteristics, such as velocity and vorticity contours in the axial and sagittal planes for one patient case to understand the influence of inlet velocity profiles. Also, the quantitative analysis of pressure drop, TAWSS, and OSI were conducted for ten patient cases to identify the closest surrogate model for normal and rapid breathing conditions. The two main findings of this study are a) idealized velocity profiles do affect the airflow characteristics compared to real velocity profiles with flat profiles exhibiting the most profound differences, and b) the quantitative analysis shows that both the Womersley profile and the parabolic profile provided the closest solutions for normal breathing, while the Womersley profile provided the closest solutions for rapid breathing. The following paragraph discusses these findings in more detail.

The first objective of this study is to assess the effect of real and idealized profiles on the flow characteristic of the patient-specific trachea. Qualitative observation of the velocity and vorticity contours in axial and sagittal planes showed the differences between the real and idealized profiles for normal and rapid breathing conditions. The axial plane shows the discrepancies in shape and sizes of spatial velocity peaks distribution in the cross-sections of the trachea between the inlet profiles. In contrast, the sagittal plane provides flow characteristics along the trachea length, clearly showing the discrepancy in the separation region between the inlet profiles. The flat profile shows distinct differences compared to parabolic, Womersley, and real profiles in axial and sagittal directions. There are no spatial velocity peaks on the flat profile, as seen in the inlet cross-section of Figure 4.5, which contributes to its distinct differences from other idealized profiles. On the other hand, the fact that a similar spatial velocity peak is present in real as well as parabolic and Womersley profiles, as seen in the inlet cross-sections of Figure 4.5 and Figure 4.8, is the reason for the similarity of flow characteristics. Flow patterns for the Womersley and parabolic profiles are similar because both have an inlet velocity profile similar to the parabolic shape. However, differences in velocity contours were observed in the rapid breathing condition between the parabolic and Womersley profiles in axial and sagittal planes. Also, during the rapid breathing condition, the flow contour was asymmetric for all three-time points evaluated but symmetric under the normal breathing condition. The reason is due to the higher Womersley number in rapid breathing.

The second objective of this study is to compare the inlet velocity profiles for normal ($f = 0.28Hz$) and rapid ($f = 1.06Hz$) breathing in ten patient cases quantitatively. The quantitative evaluation of the relative percentage difference between real and idealized profiles, for E_{TAWSS} and E_{OSI}, shows that the flat profile gives the largest relative percentage difference compared to the parabolic and Womersley profile when averaged for all ten cases for normal and rapid breathing. There is no velocity gradient for the flat profile, but the parabolic and Womersley profiles have a certain velocity gradient that is directly proportional to the WSS. This difference in velocity gradient explains the discrepancy between flat profiles compared to parabolic and Womersley profiles. Furthermore, average E_{TAWSS} and E_{OSI} for ten patient cases are similar for parabolic and Womersley in normal breathing, which can be referred to from the Table 4.3 and Table 4.5. In contrast, for rapid breathing, the average E_{TAWSS} and E_{OSI} for Womersley is less in comparison to parabolic and flat, which can also be referred to from the Table 4.4 and Table 4.6. These observations are due to the fact that a Womersley profile is flatter for the rapid breathing case than the normal breathing case. The Womersley number for rapid breathing for all the patient-specific cases on an average is 4.82 ± 0.34 (mean ± SD), and for normal breathing, it is 2.42 ± 0.17 (mean ± SD) with a difference of 2.4. A high Womersley number indicates that the flow is dominated by unsteady forces and the flow is more pulsating, resulting in a flat velocity profile. Conversely, when the Womersley number is low, flow is less pulsating and dominated by the viscous forces, resulting in the parabolic shape velocity profile [40].

Moreover, comparison of the co-efficient of pressure drop (C_p) between the inlet profiles also showed that the pressure drop for the flat profile was significantly greater than the parabolic, Womersley, and real profiles. The flatter profile has higher velocity gradient at the wall. With an increased velocity gradient, the wall shear stress increases, causing an increase in the pressure drop required to drive the flow. This observation is also true for turbulent flows as the velocity profile is flatter due to its highly unsteady nature compared to laminar flow, where the velocity profile is a parabolic shape since the viscous forces are more dominant [19, 25].

Even if the TAWSS and OSI values are derived from the idealized profiles that are the closest substitutes for the real profiles, such as the parabolic and Womersley profiles obtained in this study, deviation from the real profile results is always evident as evidenced by prior research work [80, 14]. In other words, an idealized velocity profile can never be a perfect representation of a real profile, and there will always be some variation. Additionally, this study uses the sinusoidal breathing flow rate to construct an idealized profile, instead of the patient-specific breathing flow, which is another contributing factor to error in calculation of TAWSS and OSI from actual values. The other error sources come from smoothing of the geometry for meshing to removing of the artifacts (noise and staircases) in the CT scan image. The smoothing of the geometry requires a continual examination of the shape and curvature of the patient-specific geometry. Because of the unique nature of each patient case, smoothing a large number of cases is a challenging process. Although the error is undesirable for clinical application, it can be minimized by using the patient's breathing waveform with careful segmentation and smoothing the geometry. This type of study where processing medical imaging and integrating with CFD analysis for the derivation of flow field metrics will help in understand the regional airflow dynamics through the trachea.

It should be noted that this study conducted airflow simulations for only two breathing frequencies in a small cohort of patients. For a more generalizable result, the study should be expanded to include a larger cohort, as well as higher breathing frequency ranges. Furthermore, this study has not investigated the influence of age factors in the current study since the airway structure and breathing frequency changes with age [65]. Also, the Womersley profile is the solution of the fully developed straight pipe flows that include the pulsatility effects. However, the patient-specific model is not a straight pipe and has the variation in structural features like cross-sectional area, change in the curvature, and the twisting which will affect the pulsatility of the patient-specific trachea. Therefore, a geometrical transformation to the equivalent constant cross-section cylinder can be used to address the issue [11] which is done for straight pipe simulation results section for one diameter and length. A comparison of straight pipe results with patient cases shows that the variation of differences in inlet velocity profiles across different patients is due to patient-specific nature. This difference is also backed by other studies in the literature, which justify the geometry as a greater modulator of the flow properties [57, 14]. In the current study, the "reference standard" real velocity profile is based on the experimental study conducted with the Magnetic Resonance Velocimetry (MRV) technique referred from the previous study [37]. The idealized velocity profile is constructed based upon the same flow waveform and compared with the real profile used in the study. Even though the idealized profile is constructed based on the same flow waveform and compared, a patient-specific breathing velocity profile containing secondary flow structures at the inlet of the trachea will likely underestimate the difference between the idealized velocity profile and the real profile.

Chapter 6

Conclusion

Patient-specific simulation is one of the powerful tools which will help the clinician make the necessary decision based on the prior analysis for the treatment of the patients. Simplifying assumptions for inlet conditions must be made for the computational fluid dynamics study of airflow through the trachea if the patient-specific real velocity profile is unknown. In this study, three idealized velocity profiles most commonly used in the literature were evaluated: parabolic, Womersley, and flat, to compare with real velocity profiles for normal and rapid breathing conditions. The qualitative study was conducted to evaluate the velocity and vorticity distribution in axial as well as in the sagittal plane between parabolic, Womersley, and real profiles. In comparison to other idealized inlet velocity profiles, the flat profile showed significantly different velocity and vorticity distributions in both planes with the real profile. This study also looked into the effect of breathing frequency by quantitative evaluation of pressure drop, TAWSS, and OSI for ten patient trachea cases to compare real and idealistic velocity profiles to identify the closest surrogate model. An analysis of the statistical data showed no significant difference between real and idealistic profiles. However, the differences in E_{TAWSS} were evident in the individual patient cases from the bar graph of the inlet velocity profile comparison for both normal and rapid breathing conditions. In an evaluation using E_{TAWSS}, the parabolic and Womersley profiles closely approximate the real velocity profile under normal conditions, while under rapid breathing conditions, the Womersley profile approaches the real velocity profile more closely than the flat and parabolic profiles. On the other hand, the flat profile provides maximum deviation from the real profile. The study and comparison of straight pipe simulation results conducted to understand the patient-to-patient case variation showed that the deviation of patient case tracheal geometry from straight pipe significantly influences TAWSS. Therefore, the geometrical factor must be considered while selecting the surrogate model close to the real profile. However, we generally recommend using the Womersley profile in rapid breathing conditions and the parabolic or Womersley profile in normal breathing conditions. Furthermore, if a tentative assessment of the flow field is needed, we recommend the parabolic profile as it is easier to reproduce than the Womersley profile due to mathematical complexity [36].

Chapter 7

Future work

1. During the exhalation phase, the inlet and outlet boundary condition changes their location with respect to the inhalation phase. Only the inhalation phase is included in the present simulation, but a complete simulation of the breathing cycle would be more appropriate to better understand the true dynamics of the airflow. A continuation of the work would be to analyze the boundary condition influence during a complete cycle of breathing.

2. As a continuation of this computational study, the next step would be to implement the curvature of the upper airway from the mouth to the end of the vocal cord from where the trachea starts. This portion forms the circular arc due to the curvature, which will induce the secondary flow that superimposes in the primary flow. The curvature is the reason for the lateral instability, which results in a secondary cross-sectional flow field, also known as Dean flow [20, 21], and can be characterized by counter-rotating vortices. This addition of secondary flow structure in the inlet condition will change the inlet velocity profile, resulting in the change of airflow characteristics.

3. This study used the sinusoidal-based breathing profile for the inhalation phase, which is not the case in the actual breathing flow rate. A continuation of the study incorporating a realistic breathing flow rate provided by medical information will be a more realistic representation of the data.

4. During the inhalation and exhalation phase of breathing, the trachea expands, contracts, and lengthens, which causes interaction between the wall and airflow. As a

result of this complex interaction between structure and fluid, the flow simulation results are different from what they would be if the wall were assumed to be rigid. The current simulation does not consider fluid-structure interactions, and including it will provide new insights into flow physics.

References

[1] Chronic obstructive pulmonnary disease (copd). `https://www.who.int/news-room/fact-sheets/detail/chronic-obstructive-pulmonary-disease-(COPD`, 2021. World Health Organization (WHO), Accessed: February 22, 2022.

[2] Elin Aasgrav, Sverre Gullikstad Johnsen, Are Johan Simonsen, and Bernhard Müller. Cfd simulations of turbulent flow in the human upper airways. *arXiv preprint arXiv:1706.02565*, 2017.

[3] Saleh Al-Muhsen, Jill R Johnson, and Qutayba Hamid. Remodeling in asthma. *Journal of allergy and clinical immunology*, 128(3):451–462, 2011.

[4] B Alhassan and N Tela. Modeling vital signs components and it consequence in human health. *J. Phys. Sci. Innov*, 11:1–14, 2019.

[5] Mohammed Alzahrany, Arindam Banerjee, and Gary Salzman. The role of coupled resistance–compliance in upper tracheobronchial airways under high frequency oscillatory ventilation. *Medical engineering & physics*, 36(12):1593–1604, 2014.

[6] Matthew Ball, Mohammad Hossain, and Devang Padalia. Anatomy, airway. 2017.

[7] Carina Barbosa Pereira, Xinchi Yu, Michael Czaplik, Vladimir Blazek, Boudewijn Venema, and Steffen Leonhardt. Estimation of breathing rate in thermal imaging videos: a pilot study on healthy human subjects. *Journal of clinical monitoring and computing*, 31(6):1241–1254, 2017.

[8] M Bartikian, A Ferreira, A Gonçalves-Ferreira, and LL Neto. 3d printing anatomical models of head bones. *Surgical and Radiologic Anatomy*, 41(10):1205–1209, 2019.

[9] A.J. Bates, R. Cetto, D.J. Doorly, R.C. Schroter, N.S. Tolley, and A. Comerford. The effects of curvature and constriction on airflow and energy loss in pathological tracheas. *Respiratory Physiology Neurobiology*, 234:69–78, 2016.

[10] Surya P Bhatt, Nina LJ Terry, Hrudaya Nath, Jordan A Zach, Juerg Tschirren, Mark S Bolding, Douglas S Stinson, Carla G Wilson, Douglas Curran-Everett, David A Lynch, et al. Association between expiratory central airway collapse and respiratory outcomes among smokers. *Jama*, 315(5):498–505, 2016.

[11] Evangelos Boutsianis, Sumeet Gupta, Kevin Boomsma, and Dimos Poulikakos. Boundary conditions by schwarz-christoffel mapping in anatomically accurate hemodynamics. *Annals of Biomedical Engineering*, 36(12):2068–2084, 2008.

[12] William A Briscoe, Arthur B Dubois, et al. The relationship between airway resistance, airway conductance and lung volume in subjects of different age and body size. *The Journal of clinical investigation*, 37(9):1279–1285, 1958.

[13] Hadrien Calmet, Alberto M Gambaruto, Alister J Bates, Mariano Vázquez, Guillaume Houzeaux, and Denis J Doorly. Large-scale cfd simulations of the transitional and turbulent regime for the large human airways during rapid inhalation. *Computers in biology and medicine*, 69:166–180, 2016.

[14] Ian C Campbell, Jared Ries, Saurabh S Dhawan, Arshed A Quyyumi, W Robert Taylor, and John N Oshinski. Effect of inlet velocity profiles on patient-specific computational fluid dynamics simulations of the carotid bifurcation. *Journal of biomechanical engineering*, 134(5), 2012.

[15] Kelly A Carden, Philip M Boiselle, David A Waltz, and Armin Ernst. Tracheomalacia and tracheobronchomalacia in children and adults: an in-depth review. *Chest*, 127(3):984–1005, 2005.

[16] Amlan Chakraborty, Sutirtha Chakraborty, Venkatakrishna R Jala, Bodduluri Haribabu, M Keith Sharp, and R Eric Berson. Effects of biaxial oscillatory shear stress on endothelial cell proliferation and morphology. *Biotechnology and bioengineering*, 109(3):695–707, 2012.

[17] Jiwoong Choi, Merryn H Tawhai, Eric A Hoffman, and Ching-Long Lin. On intra-and intersubject variabilities of airflow in the human lungs. *Physics of Fluids*, 21(10):101901, 2009.

[18] Kristopher S Cunningham and Avrum I Gotlieb. The role of shear stress in the pathogenesis of atherosclerosis. *Laboratory investigation*, 85(1):9–23, 2005.

[19] Lars Davidson. Closure modeling. In *Advanced Approaches in Turbulence*, pages 161–241. Elsevier, 2021.

[20] Wo R Dean. Xvi. note on the motion of fluid in a curved pipe. *The London, Edinburgh, and Dublin Philosophical Magazine and Journal of Science*, 4(20):208–223, 1927.

[21] WR Dean. The streamline motion of fluid in a curved pipe. *Phil. Mag.*, 5:673–693, 1928.

[22] Kunio Doi. Current status and future potential of computer-aided diagnosis in medical imaging. *The British journal of radiology*, 78(suppl_1):s3–s19, 2005.

[23] C Gordon Douglas and JS Haldane. The regulation of normal breathing. *The Journal of physiology*, 38(5):420, 1909.

[24] Thomas Ferkol and Dean Schraufnagel. The global burden of respiratory disease. *Annals of the American Thoracic Society*, 11(3):404–406, 2014.

[25] Robert W Fox, Alan T McDonald, and John W Mitchell. *Fox and McDonald's introduction to fluid mechanics*. John Wiley & Sons, 2020.

[26] Rainhill K Freitas and Wolfgang Schröder. Numerical investigation of the three-dimensional flow in a human lung model. *Journal of Biomechanics*, 41(11):2446–2457, 2008.

[27] Frank Gijsen, Yuki Katagiri, Peter Barlis, Christos Bourantas, Carlos Collet, Umit Coskun, Joost Daemen, Jouke Dijkstra, Elazer Edelman, Paul Evans, et al. Expert recommendations on the assessment of wall shear stress in human coronary arteries: existing methodologies, technical considerations, and clinical applications. *European heart journal*, 40(41):3421–3433, 2019.

[28] HC Grillo. Surgical anatomy of the trachea and techniques of resection. *General thoracic surgery*, pages 873–883, 1999.

[29] Hermes C Grillo, Ellen F Dignan, Tsuyoshi Miura, and J Gordon Scannell. Extensive resection and reconstruction of mediastinal trachea without prosthesis or graft: an anatomical study in man. *The Journal of thoracic and cardiovascular surgery*, 48(5):741–749, 1964.

[30] Chamindu C Gunatilaka, Andreas Schuh, Nara S Higano, Jason C Woods, and Alister J Bates. The effect of airway motion and breathing phase during imaging on cfd simulations of respiratory airflow. *Computers in biology and medicine*, 127:104099, 2020.

[31] Saunders-John E Hall. Guyton and hall textbook of medical physiology e-book, livre ebook. 2010.

[32] Xiaoyi He and David N Ku. Pulsatile flow in the human left coronary artery bifurcation: average conditions. *Journal of biomechanical engineering*, 118(1):74–82, 1996.

[33] Helene Holmgren. *On the formation and physical behaviour of exhaled particles*. Chalmers Tekniska Hogskola (Sweden), 2011.

[34] Keith Horsfield, Gladys Dart, Dan E Olson, Giles F Filley, and Gordon Cumming. Models of the human bronchial tree. *Journal of applied physiology*, 31(2):207–217, 1971.

[35] Tzung K Hsiai, Sung K Cho, Henry M Honda, Susan Hama, Mohamad Navab, Linda L Demer, and Chih-Ming Ho. Endothelial cell dynamics under pulsating flows: significance of high versus low shear stress slew rates ($\tau/\ \tau$). *Annals of biomedical engineering*, 30(5):646–656, 2002.

[36] Andrea Natale Impiombato, Giorgio La Civita, Francesco Orlandi, Flavia Schwarz Franceschini Zinani, Luiz Alberto Oliveira Rocha, and Cesare Biserni. A simple transient poiseuille-based approach to mimic the womersley function and to model pulsatile blood flow. *Dynamics*, 1(1):9–17, 2021.

[37] Sahar Jalal, Tristan Van de Moortele, Andras Nemes, Omid Amili, and Filippo Coletti. Three-dimensional steady and oscillatory flow in a double bifurcation airway model. *Physical Review Fluids*, 3(10):103101, 2018.

[38] Kirollos Salah Kamel, Gabriel Lau, and Mark D Stringer. In vivo and in vitro morphometry of the human trachea. *Clinical Anatomy: The Official Journal of the American Association of Clinical Anatomists and the British Association of Clinical Anatomists*, 22(5):571–579, 2009.

[39] Chitra Kandaswamy and Vijay Balasubramanian. Review of adult tracheomalacia and its relationship with chronic obstructive pulmonary disease. *Current opinion in pulmonary medicine*, 15(2):113–119, 2009.

[40] David N Ku. Blood flow in arteries. *Annual review of fluid mechanics*, 29(1):399–434, 1997.

[41] David N Ku, Don P Giddens, Christopher K Zarins, and Seymour Glagov. Pulsatile flow and atherosclerosis in the human carotid bifurcation. positive correlation between

plaque location and low oscillating shear stress. *Arteriosclerosis: An Official Journal of the American Heart Association, Inc.*, 5(3):293–302, 1985.

[42] Pijush K Kundu and Ira M Cohen. Fluid mechanics. 2002.

[43] Karen S Lee, Maryellen RM Sun, Armin Ernst, David Feller-Kopman, Adnan Majid, and Phillip M Boiselle. Comparison of dynamic expiratory ct with bronchoscopy for diagnosing airway malacia: a pilot evaluation. *Chest*, 131(3):758–764, 2007.

[44] Ching-Long Lin, Merryn H Tawhai, Geoffrey McLennan, and Eric A Hoffman. Characteristics of the turbulent laryngeal jet and its effect on airflow in the human intra-thoracic airways. *Respiratory physiology & neurobiology*, 157(2-3):295–309, 2007.

[45] Wilburta Q Lindh, Marilyn Pooler, Carol D Tamparo, Barbara M Dahl, and Julie Morris. *Delmar's comprehensive medical assisting: administrative and clinical competencies*. Cengage Learning, 2013.

[46] Yang Liu, RMC So, and CH Zhang. Modeling the bifurcating flow in an asymmetric human lung airway. *Journal of biomechanics*, 36(7):951–959, 2003.

[47] P Worth Longest and Samir Vinchurkar. Effects of mesh style and grid convergence on particle deposition in bifurcating airway models with comparisons to experimental data. *Medical engineering & physics*, 29(3):350–366, 2007.

[48] Catherine Loudon and Antoinette Tordesillas. The use of the dimensionless womersley number to characterize the unsteady nature of internal flow. *Journal of theoretical biology*, 191(1):63–78, 1998.

[49] HY Luo and Yang Liu. Modeling the bifurcating flow in a ct-scanned human lung airway. *Journal of Biomechanics*, 41(12):2681–2688, 2008.

[50] Mohamed Faisal Lutfi. The physiological basis and clinical significance of lung volume measurements. *Multidisciplinary respiratory medicine*, 12(1):1–12, 2017.

[51] Baoshun Ma and Kenneth R Lutchen. An anatomically based hybrid computational model of the human lung and its application to low frequency oscillatory mechanics. *Annals of biomedical engineering*, 34(11):1691–1704, 2006.

[52] Carmela Maiolo, Ehab I Mohamed, and MG Carbonelli. Body composition and respiratory function. *Acta diabetologica*, 40(1):s32–s38, 2003.

[53] M Malve, S Chandra, JL Lopez-Villalobos, EA Finol, A Ginel, and M Doblare. Cfd analysis of the human airways under impedance-based boundary conditions: application to healthy, diseased and stented trachea. *Computer methods in biomechanics and biomedical engineering*, 16(2):198–216, 2013.

[54] E Shashi Menon. *Transmission pipeline calculations and simulations manual.* Gulf Professional Publishing, 2014.

[55] FR Menter, R Langtry, and S Völker. Transition modelling for general purpose cfd codes. *Flow, turbulence and combustion*, 77(1):277–303, 2006.

[56] Douglas J Minnich and Douglas J Mathisen. Anatomy of the trachea, carina, and bronchi. *Thoracic surgery clinics*, 17(4):571–585, 2007.

[57] JG Myers, JA Moore, M Ojha, KW Johnston, and CR Ethier. Factors influencing blood flow patterns in the human right coronary artery. *Annals of biomedical engineering*, 29(2):109–120, 2001.

[58] Jessica M Oakes, Steven C Roth, and Shawn C Shadden. Airflow simulations in infant, child, and adult pulmonary conducting airways. *Annals of biomedical engineering*, 46(3):498–512, 2018.

[59] Tomas B Owatverot, Sara J Oswald, Yong Chen, Jeremiah J Wille, and Frank CP Yin. Effect of combined cyclic stretch and fluid shear stress on endothelial cell morphological responses. *Journal of biomechanical engineering*, 127(3):374–382, 2005.

[60] Sharon B Park and Divya Khattar. Tachypnea. 2019.

[61] Ratchanon Piemjaiswang, Shuichi Shiratori, Tawatchai Chaiwatanarat, Pornpote Piumsomboon, and Benjapon Chalermsinsuwan. Computational fluid dynamics simulation of full breathing cycle for aerosol deposition in trachea: Effect of breathing frequency. *Journal of the Taiwan Institute of Chemical Engineers*, 97:66–79, 2019.

[62] Shouliang Qi, Zhenghua Li, Yong Yue, Han JW van Triest, and Yan Kang. Computational fluid dynamics simulation of airflow in the trachea and main bronchi for the subjects with left pulmonary artery sling. *Biomedical engineering online*, 13(1):1–15, 2014.

[63] Shouliang Qi, Baihua Zhang, Yueyang Teng, Jianhua Li, Yong Yue, Yan Kang, and Wei Qian. Transient dynamics simulation of airflow in a ct-scanned human airway tree: more or fewer terminal bronchi? *Computational and mathematical methods in medicine*, 2017, 2017.

[64] Shouliang Qi, Baihua Zhang, Yong Yue, Jing Shen, Yueyang Teng, Wei Qian, and Jianlin Wu. Airflow in tracheobronchial tree of subjects with tracheal bronchus simulated using ct image based models and cfd method. *Journal of Medical Systems*, 42(4):1–15, 2018.

[65] Maria Ragnarsdóttir and Ella Kolbrun Kristinsdóttir. Breathing movements and breathing patterns among healthy men and women 20–69 years of age. *Respiration*, 73(1):48–54, 2006.

[66] Harpreet Ranu, Michael Wilde, and Brendan Madden. Pulmonary function tests. *The Ulster medical journal*, 80(2):84, 2011.

[67] Elizabeth A. Regan, John E. Hokanson, James R. Murphy, Barry Make, David A. Lynch, Terri H. Beaty, Douglas Curran-Everett, Edwin K. Silverman, and James D. Crapo. Genetic epidemiology of copd (copdgene) study design. *COPD: Journal of Chronic Obstructive Pulmonary Disease*, 7(1):32–43, 2011.

[68] R. C. Schroter and M. F. Sudlow. Flow patterns in models of the human bronchial airways. *Respiration Physiology*, 7(3):341–355, 1969.

[69] Yidan Shang, Jingliang Dong, Lin Tian, Kiao Inthavong, and Jiyuan Tu. Detailed computational analysis of flow dynamics in an extended respiratory airway model. *Clinical biomechanics*, 61:105–111, 2019.

[70] John Turner Sharp et al. The effect of body position change on lung compliance in normal subjects and in patients with congestive heart failure. *The Journal of clinical investigation*, 38(4):659–667, 1959.

[71] Venkataramana K Sidhaye, Kelly S Schweitzer, Michael J Caterina, Larissa Shimoda, and Landon S King. Shear stress regulates aquaporin-5 and airway epithelial barrier function. *Proceedings of the National Academy of Sciences*, 105(9):3345–3350, 2008.

[72] Bela Soni and Shahrouz Aliabadi. Large-scale cfd simulations of airflow and particle deposition in lung airway. *Computers & Fluids*, 88:804–812, 2013.

[73] Marcin Sosnowski, Jaroslaw Krzywanski, Karolina Grabowska, and Renata Gnatowska. Polyhedral meshing in numerical analysis of conjugate heat transfer. In *EPJ Web of Conferences*, volume 180, page 02096. EDP Sciences, 2018.

[74] Martin Spiegel, Thomas Redel, Y Jonathan Zhang, Tobias Struffert, Joachim Hornegger, Robert G Grossman, Arnd Doerfler, and Christof Karmonik. Tetrahedral vs. polyhedral mesh size evaluation on flow velocity and wall shear stress for cerebral hemodynamic simulation. *Computer methods in biomechanics and biomedical engineering*, 14(01):9–22, 2011.

[75] Bora Sul, Anders Wallqvist, Michael J Morris, Jaques Reifman, and Vineet Rakesh. A computational study of the respiratory airflow characteristics in normal and obstructed human airways. *Computers in biology and medicine*, 52:130–143, 2014.

[76] Nicola Sverzellati, Andrea Rastelli, Alfredo Chetta, Valentina Schembri, Luca Fasano, Angela Maria Pacilli, Valerio Di Scioscio, Tommaso Bartalena, Massimo De Filippo, and Maurizio Zompatori. Airway malacia in chronic obstructive pulmonary disease: prevalence, morphology and relationship with emphysema, bronchiectasis and bronchial wall thickening. *European radiology*, 19(7):1669–1678, 2009.

[77] Shahab Taherian, Hamid Rahai, Bernardo Z Gomez, Thomas Waddington, and Jeremy R Bonifacio. Tracheal stenosis: a cfd approach for evaluation of drug delivery. In *ASME International Mechanical Engineering Congress and Exposition*, volume 57380, page V003T03A096. American Society of Mechanical Engineers, 2015.

[78] Caroline Van Ertbruggen, Charles Hirsch, and Manuel Paiva. Anatomically based three-dimensional model of airways to simulate flow and particle transport using computational fluid dynamics. *Journal of applied physiology*, 98(3):970–980, 2005.

[79] Xiao Wang, Keith Walters, Greg W Burgreen, and David S Thompson. Cyclic breathing simulations: Pressure outlet boundary conditions coupled with resistance and compliance. In *Fluids Engineering Division Summer Meeting*, volume 57229, page V002T26A007. American Society of Mechanical Engineers, 2015.

[80] Zhenglun Alan Wei, Connor Huddleston, Phillip M Trusty, Shelly Singh-Gryzbon, Mark A Fogel, Alessandro Veneziani, and Ajit P Yoganathan. Analysis of inlet velocity profiles in numerical assessment of fontan hemodynamics. *Annals of biomedical engineering*, 47(11):2258–2270, 2019.

[81] Ewald R Weibel, Andre F Cournand, and Dickinson W Richards. *Morphometry of the human lung*, volume 1. Springer, 1963.

[82] David C Wilcox. Turbulence modelling for cfd, dcw industries. *Inc., La Canada, California*, 1998.

[83] John R Womersley. Method for the calculation of velocity, rate of flow and viscous drag in arteries when the pressure gradient is known. *The Journal of physiology*, 127(3):553, 1955.

[84] XL Yang, Yang Liu, RMC So, and JM Yang. The effect of inlet velocity profile on the bifurcation copd airway flow. *Computers in biology and medicine*, 36(2):181–194, 2006.

[85] Youbing Yin, Jiwoong Choi, Eric A Hoffman, Merryn H Tawhai, and Ching-Long Lin. Simulation of pulmonary air flow with a subject-specific boundary condition. *Journal of biomechanics*, 43(11):2159–2163, 2010.

[86] George Yuan, Nicole A Drost, and R Andrew McIvor. Respiratory rate and breathing pattern. *McMaster Univ. Med. J*, 10(1):23–25, 2013.

[87] Lei Zhang, Bahman Asgharian, and Satish Anjilvel. Inertial deposition of particles in the human upper airway bifurcations. *Aerosol Science and Technology*, 26(2):97–110, 1997.

[88] Th Zisis and E Mitsoulis. Viscoplastic flow around a cylinder kept between parallel plates. *Journal of non-newtonian fluid mechanics*, 105(1):1–20, 2002.

[89] Tareq Zobaer and Alok Sutradhar. Modeling the effect of tumor compression on airflow dynamics in trachea using contact simulation and cfd analysis. *Computers in Biology and Medicine*, 135:104574, 2021.

Appendices

Appendix A

Figures

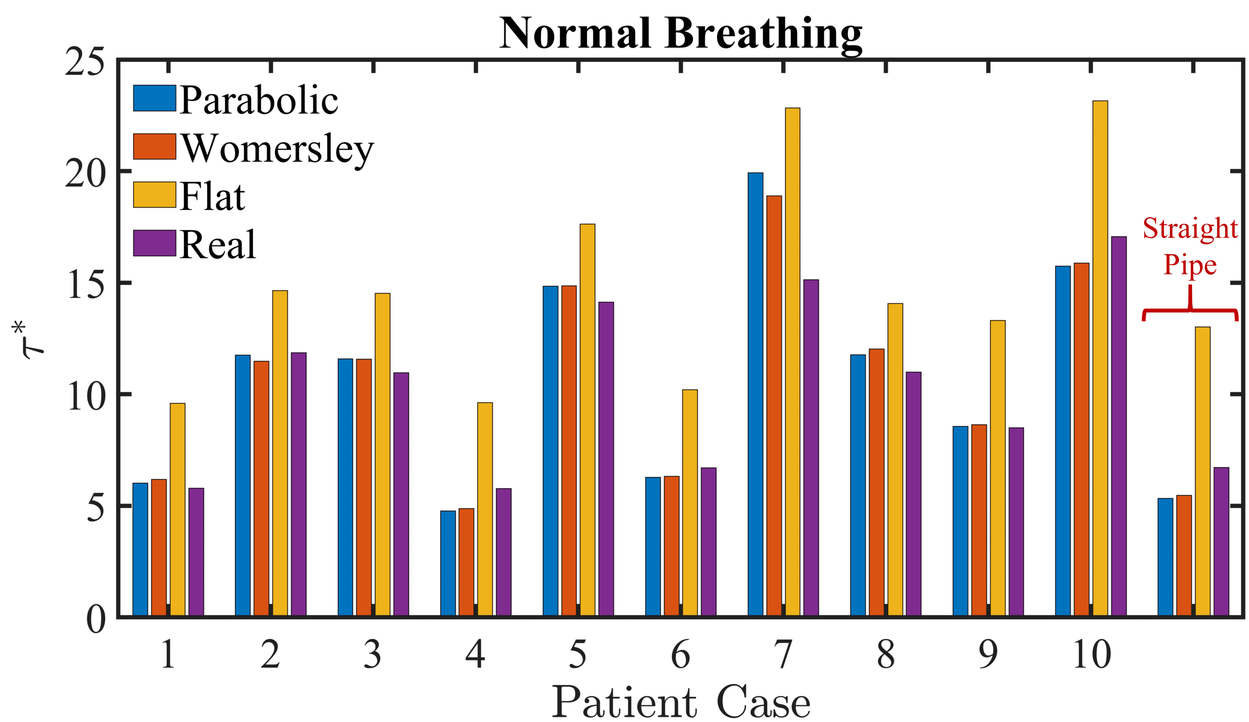

Figure A.1: Comparison of bar graph between straight pipe and patient cases simulation showing TAWSS resulting from the Parabolic, Womersley, Flat, and Real velocity profiles for normal breathing condition

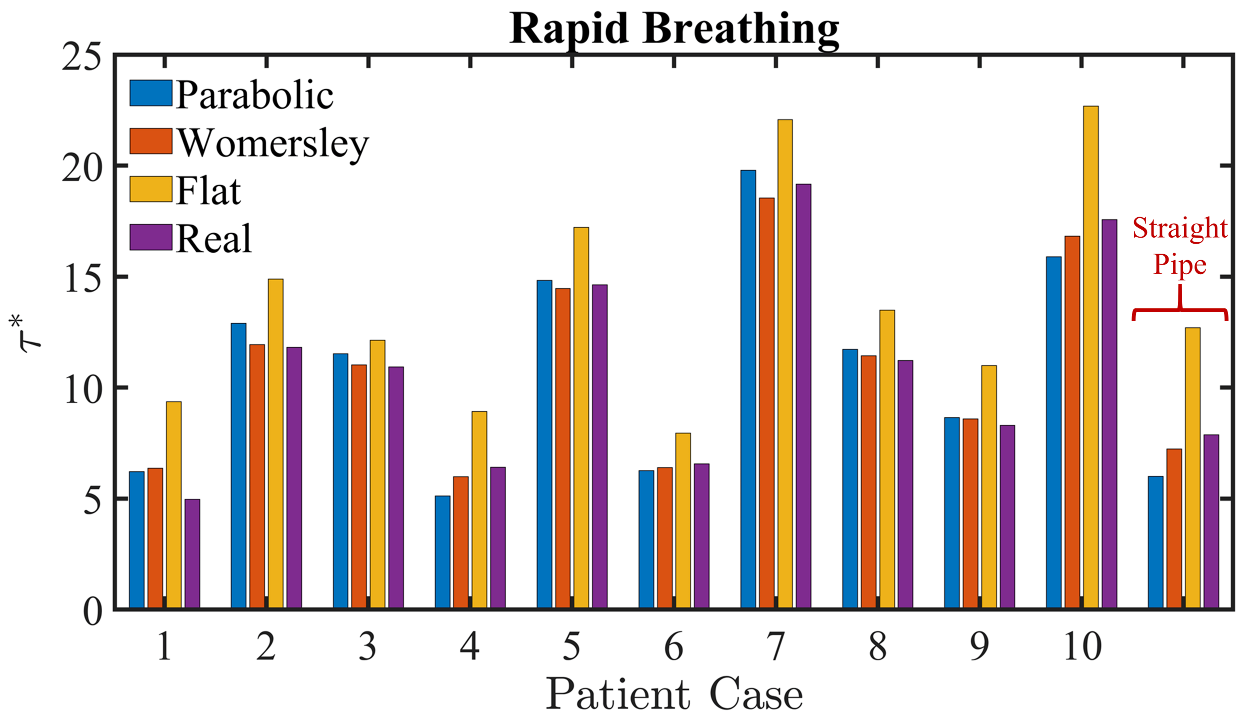

Figure A.2: Comparison of bar graph between straight pipe and patient cases simulation showing TAWSS resulting from the Parabolic, Womersley, Flat, and Real velocity profiles for rapid breathing condition

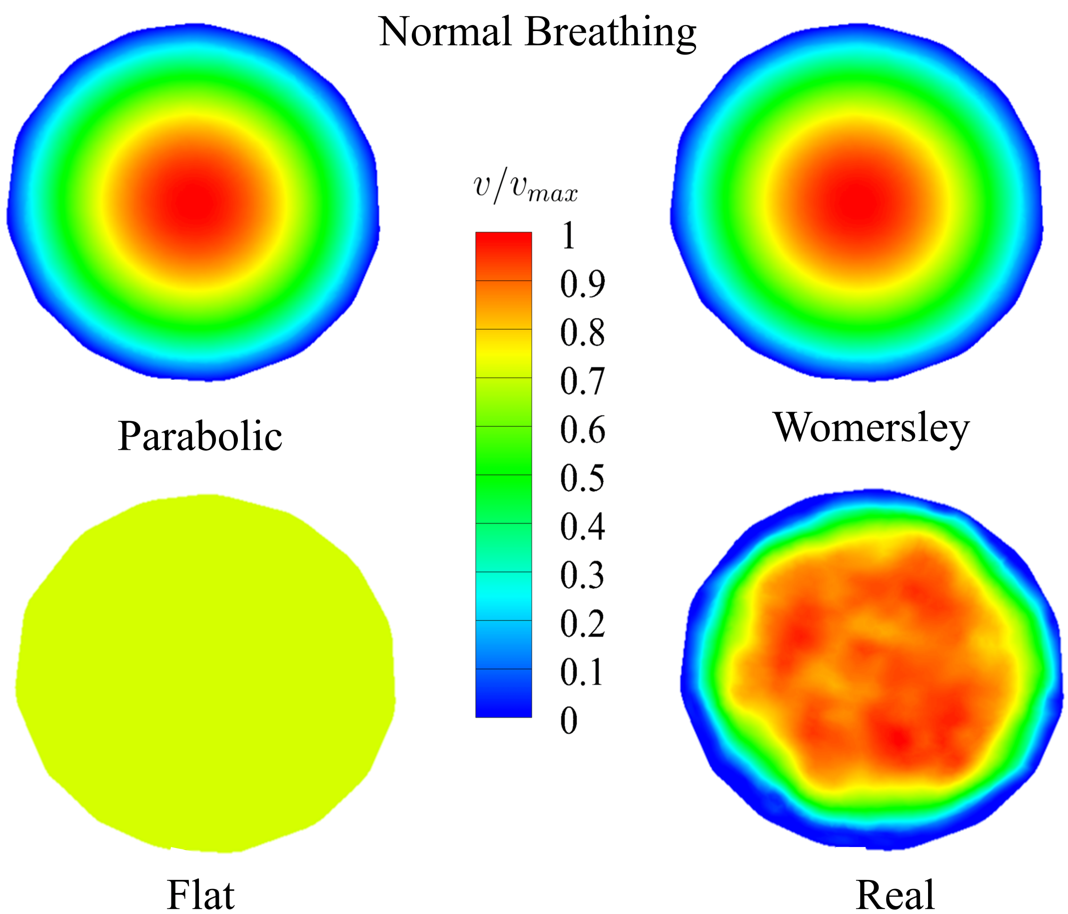

Figure A.3: Velocity contour plot at the inlet of the trachea for normal breathing condition

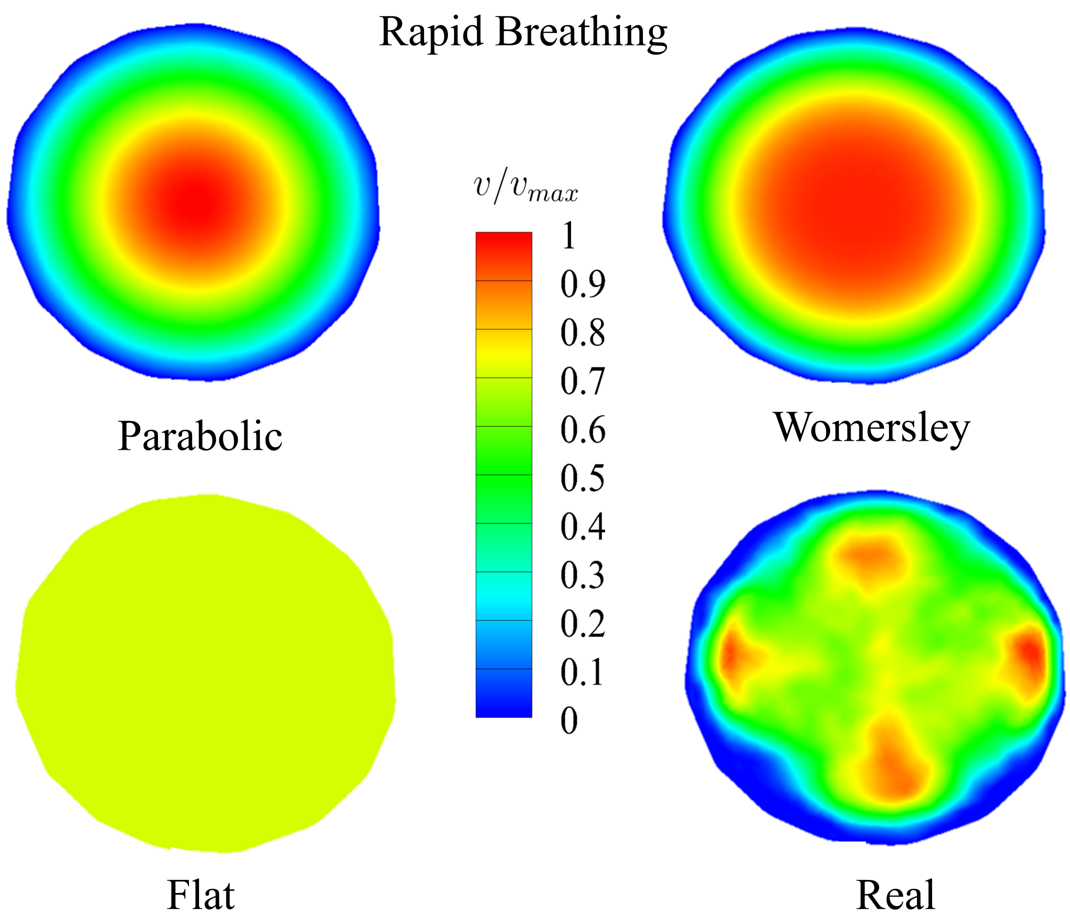

Figure A.4: Velocity contour plot at the inlet of the trachea for rapid breathing condition

Appendix B

Inlet velocity profile MATLAB® code

The MATLAB® code was use to construct the Womersley velocity profile and real velocity profile which was then implemented in ANSYS Fluent® as an inlet velocity profile using a User defined function (UDF).

B.1 Real velocity profile

```
clc
clear all
clear variables
%%Reading velocity of each phase from the data
Phases_dataname = { ...
    'Phase0.csv','Phase1.csv','Phase2.csv','Phase3.csv', 'Phase4.csv', ...
    'Phase5.csv' , 'Phase6.csv'}
message_input = 'chagne below input path for each case'
viscosityscaling = 15.083
vesselType = 'inlet'
currentFol = pwd
inDir1 = fullfile(currentFol,'Input_File_Normal')
message_output = 'chagne below output path for each case'
OutDir = fullfile(currentFol)
facecoords = strcat(currentFol,'/inlet_face_coords.dat')
count = 0
while exist(facecoords) == 0
    count = count + 1
end
```

```
facecoords = strcat(currentFol,'/inlet_face_coords.dat')
cfdVessel = readFluentCoords(facecoords)
cfdVessel.Name = vesselType
a_R = cfdVessel.Radius
v_peak = 364e-6 / cfdVessel.Area
Area_Ratio = (17.1*10^-3) / (2*a_R)
% for loop to check the mean of the datasets
for p = 1:7
% clearvars -except inDir1 Phases_dataname phases
Data_interpolated(:,:,p) = csvread(fullfile(inDir1,Phases_dataname{p}))
mean_check(p) =  mean(Data_interpolated(:,:,p),'all')
Data_final(:,:,p) = viscosityscaling * Data_interpolated(:,:,p)
mean_check_final(p) =  mean(Data_final(:,:,p),'all')
end
for phases = 1 : 7
% clearvars -except inDir1 Phases_dataname phases outDir phase1 phase2 ...
    phase3 phase4 phase5 phase6
data_phase1 = csvread(fullfile(inDir1,Phases_dataname{phases}))
data_phase1 = csvread(fullfile(inDir1,Phases_dataname{phases}))....
*viscosityscaling*Area_Ratio*1.16
table_data = readtable(fullfile(currentFol,'inlet_face_coords.dat'))
Coordinate_values = table2array(table_data)
Index_coordinates = Coordinate_values(:,1)
X_coord_values = Coordinate_values(:,2)
Y_coord_values = Coordinate_values(:,3)
Z_coord_values = Coordinate_values(:,4)
map_a = sortrows(X_coord_values)
map_b = sortrows(Y_coord_values)
map_a(:,2) = [1:length(X_coord_values)]
map_b(:,2) = [1:length(X_coord_values)]
data_length = length(X_coord_values)
for i = 1:length(X_coord_values)
    for j = 1:length(X_coord_values)
```

```
        if ( Y_coord_values(i) == map_b(j,1))
          h(i,:) = map_b(j,2)
        end
        if ( X_coord_values(i) == map_a(j,1))
          k(i,:) = map_a(j,2)
        end
    end
end
minimum_y = min(Y_coord_values)
maximum_y = max(Y_coord_values)
minimum_x = min(X_coord_values)
maximum_x = max(X_coord_values)
% % Number of coordinates is 31
x = linspace(minimum_x,maximum_x,30)
y = linspace(minimum_y,maximum_y,31)
[X,Y] = meshgrid(x,y)
% Increased the number of points to 2191 coordinate
xq = linspace(minimum_x,maximum_x,length(X_coord_values))
yq = linspace(minimum_y,maximum_y,length(X_coord_values))
[Xq,Yq] = meshgrid(xq,yq)
vq = interp2(X,Y,data_phase1,Xq,Yq,'cubic')
%velocity mapping to coordinates
for j = 1:data_length
v_cfd(j,:) = vq(h(j),k(j))
end
if phases == 1
phase0 = v_cfd
elseif phases == 2
  phase1 = v_cfd
elseif phases == 3
  phase2 = v_cfd
elseif phases == 4
    phase3 = v_cfd
```

```
    elseif phases == 5
    phase4 = v_cfd
    elseif phases == 6
    phase5 = v_cfd
    elseif phases == 7
    phase6 = v_cfd
end
end
filename_save = 'mappedforallpahses.xlsx'
filetosave = fullfile(OutDir,filename_save)
T = table(phase0,phase1,phase2,phase3,phase4,phase5,phase6)
T.Properties.VariableNames = {'Phase0','Phase1','Phase2', 'Phase3', ...
    'Phase4', 'Phase5','Phase6'}
writetable(T,filetosave,'writeVariableNames',true)
mappedforallphases = table2array(T)
%  Function to develop real velocity profile
[inlet_real_Profile] = ...
    Real_velocity_profile_2(mappedforallphases,Coordinate_values)
% write to the specific file or case that you want to save
% patient case and curved, normal or extension
filename = fullfile(OutDir,'inlet_real_Profile.csv')
csvwrite(filename,inlet_real_Profile)
```

```
function[inlet_real_Profile] = ...
    Real_velocity_profile_2(mappedforallphases,Coordinate_values)
% % Reading coordinate to make real velocity profile
Index_coordinates = Coordinate_values(:,1);
X_coord_values = Coordinate_values(:,2);
Y_coord_values = Coordinate_values(:,3);
Z_coord_values = Coordinate_values(:,4);
length_data = length(X_coord_values);
```

```
% % No need to chage anything
inlet_real_Profile = [-1;-1;-1;-1]
noofphases = 7;
inlet_real_Profile(1,2:length_data+1) = Index_coordinates;
inlet_real_Profile(2,2:length_data+1) = X_coord_values;
inlet_real_Profile(3,2:length_data+1) = Y_coord_values;
inlet_real_Profile(4,2:length_data+1) = Z_coord_values;
% % % % canges with the change in coordinate values all cases
phasedatavalues = mappedforallphases;
phasedatavalues = phasedatavalues'
% % % % average of the each time point velocity profile
for j = 1 : noofphases
Averagevel(j,:) = mean(phasedatavalues(j,1:length(phasedatavalues)));
end
Ti = 1.8;
ftime = [0, 0.1324, 0.4724, 0.8124, 1.1524, 1.4924, 1.8]
ftimeq = [linspace(0,1.8,128)]'
for i = 1 : length(phasedatavalues)
  phasedatavaluesq(1:127,i) = ...
      interp1(ftime,phasedatavalues(1:noofphases,i),ftimeq(1:127),'spline');
end
for j = 1 : 127
Averagevelq(j,:) = mean(phasedatavaluesq(j,1:length(phasedatavalues)));
end
plot(ftime,Averagevel,'o',ftimeq(1:127),Averagevelq,':.');
title('spline Interpolation for velocity with time')
inlet_real_Profile(5:131,1)= ftimeq(1:127);
inlet_real_Profile(5:131,2:length(phasedatavalues)+1) = phasedatavaluesq;
% % % % % % % % % % % % % % % % %
```

```
clc
```

```
clear all
clear variables
%%Reading velocity of each phase from the data
Phases_dataname = { 'Phase1.csv','Phase2.csv','Phase3.csv', ...
    'Phase4.csv', 'Phase5.csv'};
inDir1 = 'C:\Users\Data_paper_sahar_jalal\Interpolated_phase_water_x=75'
OutDir = ...
    'C:\Users\Data_paper_sahar_jalal\Normals_withAreaScaling_final\3_16032X'
for phases = 1:5
% % clearvars -except inDir1 Phases_dataname phases outDir phase1 ...
    phase2 phase3 phase4 phase5 phase6;
Data_interpolated(:,:,phases) = ...
    xlsread(fullfile(inDir1,Phases_dataname{phases}));
mean_check(phases) =  mean(Data_interpolated(:,:,phases),'all')
viscosityscaling = 15.083;
diameter_experiment_model = 17.1;
diameter_patient_specific_model = 16.67; %depends on patient data
diameterscaling = 17.1/16.68;
Data_final(:,:,phases) = ...
    viscosityscaling*diameterscaling*Data_interpolated(:,:,phases);
writematrix(Data_final(:,:,phases),fullfile(OutDir,Phases_dataname{phases}))
mean_check_final(phases) =  mean(Data_final(:,:,phases),'all')
end
h3 = Data_final(:,:,3
```

```
function vessel = readFluentCoords(filename)
fh = fopen(filename);
header = fgetl(fh);
areaLine = fgetl(fh);
[¬,vesselArea] = strtok(areaLine,':');
vesselArea = str2double(vesselArea(3:end));
```

```
vR = sqrt(vesselArea/pi());
line = fgetl(fh);
count = 1;
while ischar(line) && ¬strcmp(line,'\n')
[id,rest] = strtok(line);
ids(count,1) = str2double(id);
[xcoord,rest] = strtok(rest);
coords(count,1) = str2double(xcoord);
[ycoord,rest] = strtok(rest);
coords(count,2) = str2double(ycoord);
[zcoord,rest] = strtok(rest);
coords(count,3) = str2double(zcoord);
[fArea, ¬] = strtok(rest);
faceAreas(count,1) = str2double(fArea);
line = fgetl(fh);
count = count + 1;
end
fclose(fh);
xx = coords(:,1);
yy = coords(:,2);
zz = coords(:,3);
len_ids = length(ids)
ids = [ 0 : 1 : len_ids-1]'
vessel = VesselFace(xx,yy,zz,ids,faceAreas,vesselArea);
end
```

```
classdef VesselFace
properties
Name
X
Y
```

```
Z
ID
FaceAreas
Area
Radius
Origin
NumFaces
Normal
end
methods
function obj = VesselFace(x,y,z,id,fAreas,area,name)
if nargin == 3
obj.X = x;
obj.Y = y;
obj.Z = z;
obj.Origin = obj.GetOrigin(x,y,z);
obj.NumFaces = obj.GetFaceCount(x);
obj.Normal = obj.GetNormal(x,y,z);
elseif nargin == 6
obj.X = x;
obj.Y = y;
obj.Z = z;
obj.ID = id;
obj.FaceAreas = fAreas;
obj.Area = area;
obj.Radius = obj.GetRadius(area);
obj.Origin = obj.GetOrigin(x,y,z);
obj.NumFaces = obj.GetFaceCount(x);
obj.Normal = obj.GetNormal(x,y,z);
elseif nargin == 7
obj.X = x;
obj.Y = y;
obj.Z = z;
```

```
obj.ID = id;
obj.FaceAreas = fAreas;
obj.Area = area;
obj.Name = name;
obj.Radius = obj.GetRadius(area);
obj.Origin = obj.GetOrigin(x,y,z);
obj.NumFaces = obj.GetFaceCount(x);
obj.Normal = obj.GetNormal(x,y,z);
end
end
function radius = GetRadius(¬,area)
radius = sqrt(area/pi);
end
function origin = GetOrigin(¬,x,y,z)
origin = [mean(x);mean(y);mean(z)];
end
function plot(obj)
scatter3(obj.X,obj.Y,obj.Z,'b');
end
function num = GetFaceCount(¬,coords)
num = length(coords);
end
function normVec = GetNormal(obj,x,y,z)
p1 = [x(1);y(1);z(1)];
p2 = [x(round(obj.NumFaces/2));
y(round(obj.NumFaces/2));
z(round(obj.NumFaces/2))];
p3 = [x(end);y(end);z(end)];
count = 4;
while dot(p2-p1,p3-p1) == 0 && count < obj.NumFaces
p3 = [x(count);y(count);z(count)];
count = count + 1;
end
```

```
normVec = cross(p2-p1,p3-p1)/norm(cross(p2-p1,p3-p1));
end
end
end
```

B.2 Womersley velocity profile

```
clc;
clear all;
%% User Define Variables Here
caseFoldername = 'Normal_Womersley';
vesselType = 'inlet';
intnum = 128;
fileType = '.xls';
TB = 3.6 ; % Time period for normal and rapid breathing conditions
%%(normal-3.6s or rapid-0.92s)
ftime_true = 0:0.1:(TB/2);
currentFol = pwd;
facecoords = strcat(currentFol,'/inlet_face_coords.dat');
count = 0
while exist(facecoords) == 0
count = count + 1
end
facecoords = strcat(currentFol,'/inlet_face_coords.dat');
kmu = 1.52*10^-5; % dynamic viscosity/density and unit is in m^2/s
%% Read Segment Output
f = ftime_true;
ftime = f';
ftimei = linspace(ftime(1),ftime(end),intnum)';
Qmax = 364e-6;%input('maximum flow rate for wo 3 - 364e-6 and wo 6 - ...
    360e-6? \n');
```

```
%max volume flow rate whihc is also B1
vfr = Qmax * sin ((2*pi()/TB)*ftime);
nd = length(ftime_true);
%% Read Fluent Coordinates, IDs, and Initialize cfdVessel Object
cfdVessel = readFluentCoords(facecoords);
cfdVessel.Name = vesselType;
a_R = cfdVessel.Radius;  %input('Radius of the geometry? \n');
%% Womersley Specific Variables
alpha_w = a_R*sqrt(2*pi()/TB/kmu); % Womersley number %change Radius ...
    for each patient data
B1 = Qmax;
vfr_poly(:,1) = interp1(ftime,vfr,ftimei,'spline');
%% Get Womersley Profile
w_arr = getWProfile(cfdVessel,B1,kmu,intnum,ftimei,TB);
w_prof = VelocityProfile(ftimei,w_arr,'Womersley');
%% Write Womersley Profile
csvwrite(sprintf('./%s_Womersley_Profile.csv',cfdVessel.Name),[[-1 ...
    cfdVessel.ID']; [-1 cfdVessel.X']; [-1 cfdVessel.Y']; [-1 ...
    cfdVessel.Z']; w_prof.Timepoints(1:end-1), w_prof.Profile(1:end-1,:)]);
disp('Womersley Profile written.');
```

```

function w_arr = getWProfile(vessel,B1,kmu,intnum,ftimei,TB)
a_omega = 2*pi()/TB; % fundamental frequency
w_arr = zeros(intnum,vessel.NumFaces);
for t = 1:intnum
for i = 1:vessel.NumFaces
faceDist = sqrt((vessel.X(i)-vessel.Origin(1))^2 + ...
    (vessel.Y(i)-vessel.Origin(2))^2 + (vessel.Z(i)-vessel.Origin(3))^2);
% calculate distance of each face from origin
if(faceDist > vessel.Radius)
```

```
w_vel = 0;
else
ii = sqrt(-1);
nn = 1
alpha_n = vessel.Radius*(sqrt(nn*a_omega/kmu));
J0_1 = besselj(0,alpha_n*faceDist/vessel.Radius*ii^1.5);
J0_2 = besselj(0,alpha_n*ii^1.5);
J1 = besselj(1,alpha_n*ii^1.5);
w_vel = (-ii * B1/(pi()*vessel.Radius^2)) * ...
    ((1-J0_1/J0_2)/(1-2*J1/(alpha_n*ii^1.5*J0_2))) * ...
    exp(ii*nn*a_omega*ftimei(t));
end
w_arr(t,i) = real(w_vel);
end
display(t);
end
end
```